Dissertation
submitted to the
Combined Faculties for the Natural Sciences and for Mathematics
of the Ruperto-Carola University of Heidelberg, Germany
for the degree of
Doctor of Natural Sciences

presented by
Diplom-Physiker Alexander Robert Weiß
born in: Stuttgart

Oral examination: May 21, 2003

Point Spread Function Reconstruction for the Adaptive Optics System ALFA and its Application to Photometry

Referees: Prof.Dr. Reinhard Mundt
Prof.Dr. Immo Appenzeller

Zusammenfassung:

Die adaptive Optik (AO) ALFA, die vom Max-Planck-Institut für Astronomie am Calar Alto Observatorium betrieben wird, steht seit einigen Jahren für astronomische Beobachtungen zur Verfügung. Die wissenschaftliche Verwendung von mit Hilfe dieses Instruments gewonnenen Aufnahmen, wird, wie auch bei anderen AO Systemen, durch orts- und zeitabhängige Variationen der Punktverbreiterungsfunktion (PSF) erschwert. Aufgrund anisoplanatischer Effekte und/oder Überbelichtung des Leitsterns ist es i.a. nicht möglich, Informationen über die PSF aus Aufnahmen zu entnehmen. Daher ist es wünschenswert, unabhängige Schätzungen der PSF an jeder Stelle des Sichtfeldes durchführen zu können.
Diese Schätzungen können aus Messungen von ALFAs Wellenfrontsensor (WFS) gewonnen werden. Zu diesem Zweck war es notwendig, einen vorhandenen Algorithmus, der für Curvature-Sensoren entwickelt wurde, für den in ALFA verwendeten Shack-Hartmann Sensor zu adaptieren. Dieser Algorithmus wurde dann mittels Simulationen hinsichtlich Leistung und Anwendungsmöglichkeiten getestet.
Abhängig von der Helligkeit des Leitsterns und der gewählten Regelkreisfrequenz sind WFS-Signale unterschiedlich verrauscht. Um zufriedenstellende Ergebnisse mit dem PSF-Schätzalgorithmus zu erzielen, muss dieses Rauschen verlässlich bestimmt werden. Für ALFA ist diese Bestimmung nur indirekt durch Zeitreihenanalyse der WFS-Signale möglich. In diesem Rahmen wird eine neue Schätzmethode vorgeschlagen, die im Fall dunkler Leitsterne und niedriger Regelkreisfrequenzen sehr gute Ergebnisse ermöglicht.
PSF Schätzungen abseits der Korrekturachse erfordern die Kenntnis der vertikalen Turbulenzverteilung in der Atmosphäre. Daher wurden simultan zu Beobachtungen mit ALFA Messungen mit einem SCIDAR-System durchgeführt. Diese Messungen dienten zudem der Überprüfung von Werten atmosphärischer Parameter, die aus WFS-Signalen sowie Sternaufnahmen gewonnen wurden.
Der abschließende Vergleich von aus Aufnahmen entnommenen PSFs mit den entsprechen Schätzungen ergab in allen Fällen gute Übereinstimmung. Zudem ergab sich eine erhebliche Verbesserung der photometrischen Genauigkeit bei Verwendung einer lokal geschätzten PSF gegenüber der Leitstern-PSF.

Abstract:

The ALFA adaptive optics (AO) system, operated by the Max-Planck-Institut für Astronomie at the Calar Alto Observatory, has been available as a standard facility instrument for some years now. As with other AO systems, however, the scientific use of observations with this instrument is complicated by the time- and space-variant nature of the system point spread function (PSF). Generally, the PSF information cannot be taken from the images due to anisoplanacy and/or overexposure of the guide star. It is therefore highly desirable to obtain an independent estimate of the PSF at each position in the field of view.
This estimate can be derived from the wavefront sensor (WFS) signals of the ALFA system. It was necessary to adapt an existing algorithm developed for curvature sensors to the Shack-Hartmann sensor (SHS) used on ALFA. The practicability and performance of this algorithm was then tested using simulations of atmospheric turbulence.
WFS signals are affected by noise, depending on the brightness of the guide star as well as the selected loop frequency; this noise has to be reliably determined in order to obtain satisfactory results from the PSF estimation process. With ALFA, noise estimation is only possible indirectly by time-series analysis of the WFS signals. A new method is proposed that delivers superior results for faint guide stars and low loop frequencies.
PSF estimation away from the guide star requires knowledge of the vertical turbulence profile of the atmosphere. Hence, SCIDAR measurements were carried out alongside AO observations. These measurements also served to cross-check estimates of atmospheric parameters gained from WFS signals as well as images.
Finally, on- and off-axis PSFs extracted from images were compared to their estimated counterparts, with good agreement found in all cases. Additionally, it could be shown that the photometric accuracy is strongly improved by using a locally estimated PSF as compared to the guide star PSF.

To my father,
in loving memory

Contents

Chapter 1

Introduction

The last decade has seen a growing number of observatories being equipped with Adaptive Optics (AO), a technique to correct for the degradation of astronomical imaging by the earth's atmosphere. The fact that the performance of telescopes was not only restricted by shortfalls in the manufacturing of mirrors and lenses or alignment accuracy, but also, and strongly so, by the movements of the air was noted as early as 1704 in Newton's *Opticks*.

Since the invention of the telescope, there were two main desires of the astronomers using that instrument: to "go deeper", meaning to be able to see ever fainter objects in the universe, and to "resolve higher", in order to study finer and finer details of the celestial bodies. Both of these goals are subject to limitations due to atmospheric turbulence. For all of the improvements of astronomical observations, beginning with photographic plates up to the modern electronic detectors like CCDs and APDs, the maximum spatial resolution even of the latest 8 m class telescopes is not higher than that of ambitious amateur equipment with aperture diameters of some tens of centimeters. The reason for this is that the resolving power of telescopes is seeing- rather than diffraction limited, i.e. determined not by the optical properties of the instrument but by that of the atmosphere. Sensitivity is also affected and the consequences are dramatic: while the time to reach a given signal-to-noise ratio (SNR) on a specific object would fall with the 4th power of the aperture diameter in the diffraction limited case, it only falls with the 2nd power under seeing conditions. So, the step from 3m to 10m class telescopes could reduce the necessary integration times by a factor of 100, while under real conditions the performance gain is more about a factor of 10.

There are two ways to overcome the restrictions of observing through the atmosphere: either by avoiding it altogether by putting instruments in space or correcting for its degrading effects while observing from the ground.

The success of the Hubble Space Telescope (HST) has shown the promises of observing from space. Not only did it reach the imaging quality allowed by its optics, but it also benefited from the absence of other complications of ground-based astronomy: notably the missing of sky background noise as well as atmospheric emission and absorption lines in spectroscopy. The downside of HST's tremendous achievements, however, lies in its price; development and launch alone summed up to about 3 billion US dollars, and its share on NASA's budget for maintenance missions and the necessary infrastructure is also substantial. For this reason, space telescopes offer only a partial, if very important, solution to the problems imposed by imaging through the atmosphere.

This leaves the option to improve ground-based observations by techniques that correct for atmospheric distortions. *Speckle imaging* solves the resolution problem but wreaks havoc on sensitivity; the very short exposure times (several milliseconds in the visual) dictated by this method increase both

measurement and photon noise, thus limiting its applicability to objects brighter than 11th magnitude. Additionally, diffraction limited images are only delivered through post-processing, rendering speckle imaging unsuitable for spectroscopy.
The method of choice is therefore AO, that actively and in real-time compensates for wavefront distortions imposed by the atmosphere. Its basic principle is the measurement of phase aberrations on a reference source which are subsequently compensated by a deformable mirror, with the goal to keep those aberrations as small as possible. Today, AO can be regarded as a mature technology and consequently is part of the instrument pool of every recent observatory.

A short history of adaptive optics

The concept of adaptive optics was first described in the 1950s by Babcock (1953); his account already contained all the elements of a modern AO system, i.e. wavefront sensor, phase corrector and a control system. Due to the technical limitations, mainly in sensor and computer technology, the system was not sufficiently successful. Hence, the following decades concentrated on image movement (tip-tilt) correction only, which is much easier to achieve. Beginning in the middle of the 1970s, however, interest in the field grew again, albeit not for astronomical but military applications; since it was mostly classified, much of the research did not reach the scientific community.
An French group independently developed an AO system for the Observatoire d'Haute Provence, which employed a Shack-Hartmann sensor and a deformable mirror with 19 actuators (COME-ON, (Rousset et al., 1990)). The same system was later upgraded and installed at ESO's 3.6m telescope at La Silla, Chile, where it finally became the first AO user instrument under the name of ADONIS (Beuzit et al., 1994). Meanwhile, a different group developed a new sensor type, the curvature sensor, along with a new kind of deformable mirror, the bi-morph mirror, which was installed at the Canada-France-Hawaii telescope (CFHT) and after several upgrades evolved into the PUEO system (Roddier, 1988).
The success of these early AO systems prompted other observatories to develop similar ones for other 3-4m class telescopes, like Mt. Wilson, the Italian Telescopio Nazionale Galilei on La Palma or the William Herschel telescope. Of these follow up systems, ALFA was the first to go into operation; it additionally used a laser guide star (LGS) with varying success, that has now been decommissioned in order to free up resources for LGS projects at larger telescopes.
All of the AO systems mentioned above were able to rival the infrared resolution of the HST under good seeing conditions; recently, AO entered a new stage by obtaining images surpassing HST in image quality with the newly installed NACO at ESO's VLT(Brandner et al., 2002). Several other AO projects for 8m class telescopes are currently under development or actual deployment and promise to reach unprecedented image quality (e.g. GEMINI, SUBARU etc.).

Current trends in adaptive optics

With all the success of AO correction of astronomical imaging, there are two drawbacks which have to be addressed for further development: the first is sky coverage, the second anisoplanacy.
Every AO system needs a guide star as a beacon for the correction of distorted wavefronts. Since, for good correction quality, a high temporal sampling is needed with all wavefront sensor types, the guide star has to be bright enough, i.e. has to deliver a high enough photon flux, to make such measurements feasible. Even under most favorable conditions a star of at least 16th magnitude is needed for nearly all AO systems.

Due to the second problem, anisoplanacy, the corrected field of view (FOV) for an AO is limited to several arcseconds, which means that the bright star has to be very close to an interesting astronomical object (see also next section). In consequence, systems using natural guide stars as corrective beacons are limited to a sky coverage of a few percent only.
The problem of guide stars can in principle be dealt with by using an artificial beacon, projected by a powerful laser into the sodium layer at a height of approximately 90km. There are, however, some difficulties connected with the use of laser guide stars, an account of which can be found in Ageorges and Dainty (2000).
While laser guide stars are helping to overcome the lack of suitable stars for AO correction, they do net help in eliminating anisoplanacy; but, since this problem is a consequence of the exclusive correction of aberrations in the telescope pupil, it can be tackled by extending the range of correction to layers above the aperture. This technique is known as multi-conjugate AO (MCAO), aiming to measure and compensate aberrations originating in various heights of the atmosphere. There are two main approaches for the technical implementation, atmospheric tomography (Tallon and Foy, 1990) and layer-oriented MCAO (Diolaiti et al., 2001); while tomography requires several bright guide stars and thus most probably a costly laser system, layer-oriented MCAO promises to reach very high sky coverage using only natural beacons (Ragazzoni et al., 2002). As of today, however, no operational MCAO system exists, so this interesting technique still has to prove its potential at a telescope.

ALFA

The adaptive optics system ALFA (Adaptive Optics with a Laser for Astronomy) is operated by the Max-Planck-Institut für Astronomie (MPIA) at its 3.5m telescope located at Calar Alto in Spain. It was installed at the telescope in 1996 and after several upgrades is used for scientific observations since 1998. Its features include a 97 actuator continuous face deformable mirror and remotely exchangeable lenslet arrays for its Shack-Hartmann sensor. Originally, a LGS was part of ALFAs design, operating with varying success (Rabien et al., 2000), but this component was put out of operation in 2000 in favor of a laser for VLTs CONICA system.
From 1998 to 2000 a number of very successful improvements were introduced into the system: the use of Karhunen-Loeve instead of Zernike modes for measurement and correction, more accurate centroiding algorithms for the Shack-Hartmann sensor and the keystone design lenslet array considerably increased average correction Strehl ratios as well as loop stability (Kasper et al., 2000a). Today, ALFA is capable to use stars with visual magnitudes as faint as $m_R = 14$ as guide stars and still deliver K-Band Strehl ratios of 10-20% near the diffraction limit. Using guide stars brighter than $m_V = 9$, the Strehl ratio regularly exceeds 50% under good seeing conditions.
With the technical performance goal reached, attention was turning to the reduction and interpretation of scientific data obtained with ALFA correction.

Why PSF reconstruction is needed - an introductory example

As already mentioned, the success of AO comes at a price. In uncorrected, i.e. seeing limited observations, the imaging properties of the optical system are more or less the same over the whole field of view; in long-exposure imaging, if aberrations occur, they are static and mostly known . In that sense, the telescope is *isoplanatic*. With an AO system, however, the point spread function (PSF) is neither time- nor space-invariant. While time dependence is not dramatic and comparable to that of an uncorrected system, the space-variance is a fundamental difference; it is caused by the different viewing directions of the AO system (at the guide star) and the science object (mostly not coincident with the

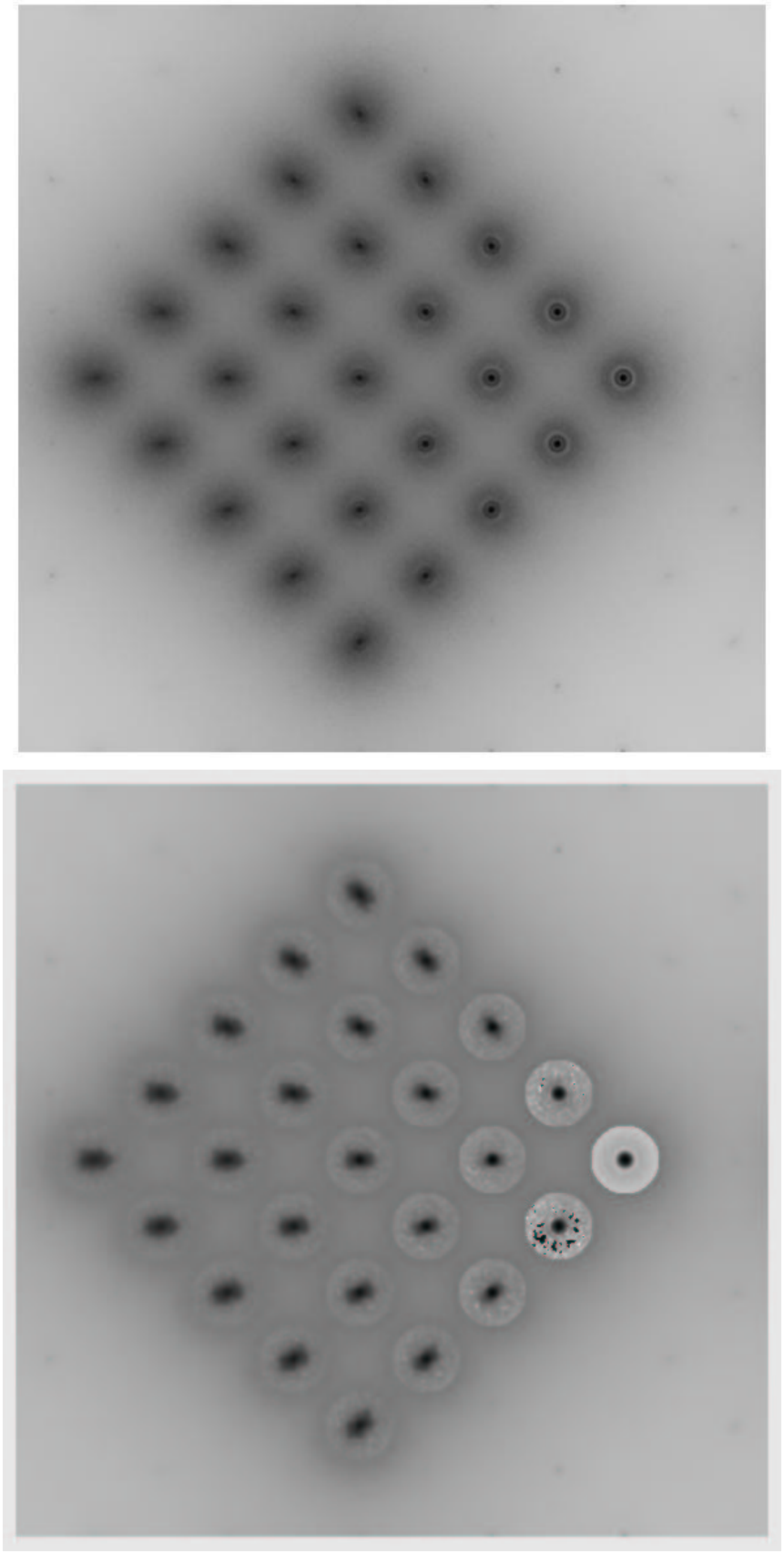

Figure 1.1: *Long-exposure image of a simulated star field corrected by an adaptive optics system, grayscale is inverted for better visibility. Horizontal and vertical distances between stars are 4 arcseconds (top). Same image deconvolved with the guide star PSF (bottom).*

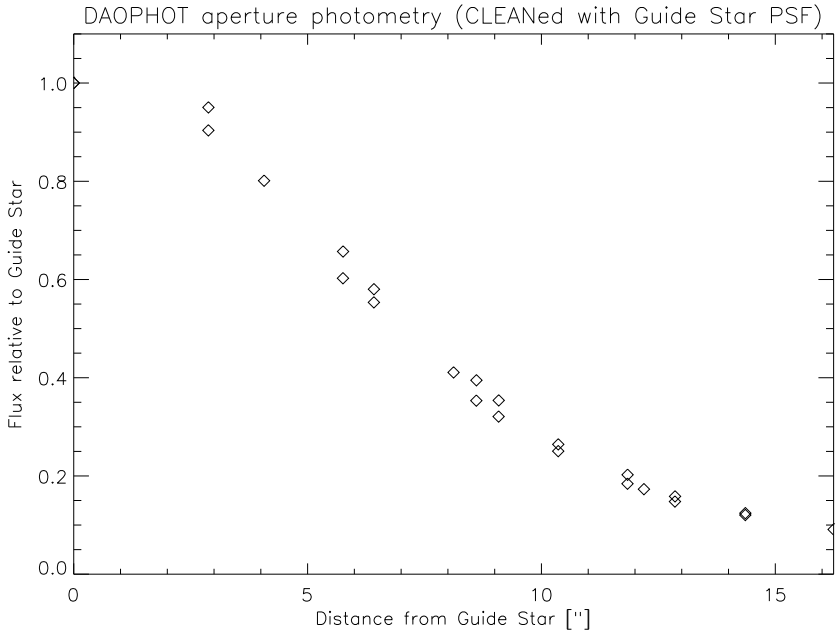

Figure 1.2: *Result of aperture photometry on deconvolved image.*

guide star). Imaging with a single-layer AO system is therefore *anisoplanatic*. Of course, even the off-axis performance of AO correction is better than seeing-limited imaging, but many of the data reduction techniques that rely on space-invariance of the PSF have to be used with care on AO corrected images. To illustrate this, a simulation on a very convenient diamond shaped star-field was carried out (details on the parameters used can be found in Chapter 2.3). Figure 1.1 shows a long-exposure image of this simulation; correction was done with measurements on the rightmost star. Two effects are clearly visible: with increasing distance to the guide star, correction quality drops and the PSFs are larger than the diffraction limit; additionally, the off-(correction)-axis PSFs are all elongated in the direction of the guide star. Now, e.g., if an estimate of the relative brightness of the stars is desired, photometry has to be done. There are basically two ways to accomplish this: either PSF or aperture photometry. The first of these assumes that the system PSF is known within a given accuracy, while the second collects flux within an aperture of given size centered on a star. Obviously, both methods rely on a constant PSF, or at least a PSF with a constant size.

In order to show the consequences of "naive" application of these techniques to an AO compensated image, the result of the simulation was first deconvolved using the CLEAN algorithm (Högbom, 1974) and the guide star PSF. The result of this deconvolution is shown in the bottom image of figure 1.1[1]. While obviously some improvement has been reached, indicated by the higher contrast and smaller halo of even the most distant stars, both the elongation and the increasing PSF size are still clearly visible. Now, aperture photometry is performed on the CLEANed image, with the aperture size being adapted to the guide star PSF, i.e. the instrument resolution. All stars in the simulation have the same brightness, but, as figure 1.2 shows, photometry delivers a completely different result, with flux estimates relative to the guide star dropping to 10% of the actual value at a distance of 16". Although this simulation exaggerates a bit, since the chosen atmospheric conditions are comparatively bad (see

[1]The brighter circular areas around the stars are a consequence of the CLEAN algorithm.

chapter 2.3), it clarifies the pitfalls of unreflected application of standard photometric techniques to AO assisted imaging.
It should be noted that anisoplanacy is not the only reason for the need to reconstruct the system PSF. A common situation is that the object of interest lies within the isoplanatic patch but is much fainter than the guide star; in order to achieve a good SNR on the science goal, the guide star has to be heavily overexposed, rendering useless the PSF obtained from its image. Similarly, if the beacon used for correction is not a point source but an extended object (e.g. a LGS, an asteroid etc.), its image is by definition not a PSF.

Goal of this work

The goal of this work is to find a way to reconstruct the on- and off-axis PSF of the ALFA system from wave front sensor signals. For on-axis reconstruction, an algorithm was introduced by Veran et al. (1997) for the PUEO AO at CFHT, using a curvature wave-front sensor. For several reasons (most notably noise estimation), this algorithm has to be modified before being applicable to a Shack-Hartmann type system. Additionally, off-axis reconstruction requires knowledge of the distribution of turbulence throughout the atmosphere, measured simultaneously with AO observations.

Chapter 2

Turbulence and Adaptive Optics

Atmospheric turbulence is the main source of resolution limitations of ground-based optical and infrared astronomy. Adaptive optics has been devised as a means to overcome these limitations and served this purpose with increasing success over the last decades; however, to use AO enhanced images for scientific ends, a fair knowledge of the properties of the used optical system is mandatory. As these properties are neither space- nor time-invariant for AO systems, this is a non-trivial task.
This chapter will introduce the theoretical concepts necessary to obtain a good estimation of an AO system's optical properties, depending on controllable (AO system) and non-controllable (atmospheric turbulence) parameters.
We start with a short review of Kolmogorov's theory of turbulence and its effects on astronomical imaging. Some detail will be given on the first and second order perturbations, i.e. phase variations and scintillation respectively, caused by the atmosphere. In this context the concept of SCIDAR, a means to measure the distribution of atmospheric turbulence, will also be discussed.
The next section deals with the general principle and the setup of a typical AO system. Although other types of sensors will be mentioned, the discussion concentrates on Shack-Hartmann type systems with a modal correction approach, since ALFA follows this design.
Section 2.3 reviews the foundations of on-axis (i.e. guide star) PSF reconstruction by introducing and examining the optical transfer function components contributing to a long-exposure image of a point-like source. Since these concepts were originally conceived for a curvature sensor type AO system (Veran et al., 1997), some differences and problems are to be taken into account. This scheme will then be extended to off-axis PSF reconstruction.
Finally, the example presented in the introduction will be tackled with the instruments developed in the preceding sections, in order to show the improvements possible with a known PSF.

2.1 Effects of Turbulence on Astronomical Imaging

This section starts with a review of Kolmogorov's theory of turbulence as applied to the atmosphere. The most important effects of turbulence on wavefronts incident on the earth's atmosphere are variations in phase due to refractive index fluctuations in turbulent layers and amplitude modulations originating in diffraction at these layers. A very good and complete introduction to these problems can be found in Roggemann and Welsh (1996), a more compact one in the second chapter of Hardy (1998).
Both phase and amplitude modifications caused by turbulence will be examined in separate subsections, with the amplitude subsection extended by a description of a method to measure the vertical

structure of atmospheric turbulence.

2.1.1 Atmospheric Turbulence

The earth's atmosphere is a system far from equilibrium. The diurnal cycle as well as local variations such as cloud cover, large bodies of water etc. cause differences of the local energy input, which give rise to bulk motions of air. Inside large low or high pressure systems this flow of air is mainly concentrated in horizontal layers. If the Reynolds number of these flows, defined as $Re = L_0 v_0 / k_v$ (with L_0 the characteristic length of the flow, v_0 its characteristic velocity and the kinematic viscosity k_v), is higher than one, turbulence will occur. With L_0 being typically in the range of $10 - 100$ m, v_0 around $5 - 15$ m/s and the k_v of air given by 10^{-5}, Re is usually about 10^3, so turbulence in airflow is the rule rather than the exception.

Turbulence Models

Kolmogorov developed a simple model for turbulence that describes the distribution of energy in structures (eddies) of different sizes by a power law (Pope, 2000). It is based on the assumption that energy is transferred from large to ever smaller vortexes until the characteristic scale of the very smallest ones reaches a size that lets the Reynolds number drop to the laminar regime where energy is finally dissipated. According to Kolmogorov the distribution of energy in the turbulent structures can

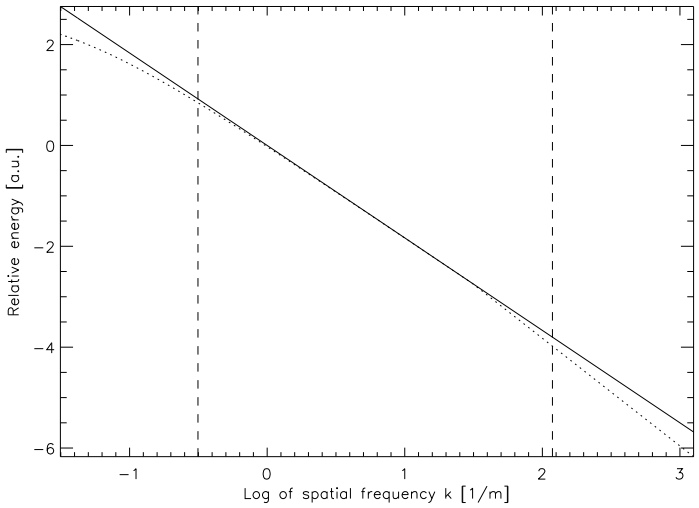

Figure 2.1: *Kolmogorov (solid) and von Karman (dotted) turbulence energy spectra. The vertical lines show the limits of the outer and inner scale.*

be described by a power law in spatial frequency space,

$$E(\vec{\kappa}) = |\vec{\kappa}|^{-11/3}, \tag{2.1}$$

with the spatial wavenumber $\vec{\kappa}$. Obviously this equation is only valid in the case of isotropic turbulence, generally a sensible assumption for the free atmosphere. A more important restriction is the valid range of this energy spectrum, the so-called *inertial range*, between an outer scale L_0 that gives the size of the largest structure and the inner scale l_0 where turbulent movement finally breaks down.

The outer scale usually is on the order of meters near the ground up to several tens of meters in the free atmosphere, while the inner scale varies from millimeters to centimeters. This situation is indicated by the dashed lines in figure 2.1. Of course the model of a sharp cutoff in energy at both ends of the power law is quite unnatural. To overcome this problem, the Kolmogorov spectrum has been modified in several ways, the most widely used modification being the *von Karman*-spectrum, given by

$$E(\vec{\kappa}) = (|\vec{\kappa}| + \kappa_0)^{-11/6} \exp\left(-|\vec{\kappa}|^2/\kappa_i^2\right), \tag{2.2}$$

where $\kappa_0 = 2\pi/L_0$ and $\kappa_i = 5.92/l_0$. This spectrum is also plotted in figure 2.1 for the same set of atmospheric parameters as the Kolmogorov one.

Index of Refraction Variations and the Structure Function

The variations in energy and size of the turbulent structures lead to local variations of temperature and pressure in a given turbulent layer. But as the index of refraction of air is a function of those quantities, given by

$$n(P,T) - 1 = \frac{77.6P}{T} 10^{-6}, \tag{2.3}$$

where temperature T in K and pressure P in hPa, turbulence affects the propagation of optical waves through the atmosphere. The refractive index is a passive quantity that has no influence on turbulence itself and it can be shown (Obukhov, 1949) that it follows the same spatial frequency law as the energy distribution; i.e. for the Kolmogorov case

$$\phi_n(|\vec{(}\kappa)|) = 0.033 C_n^2 \kappa^{-11/6}, \tag{2.4}$$

with the *refractive index structure constant* C_n^2. In calculations and simulations, the divergence at $\kappa = 0$ is very inconvenient. Hence, instead of equation 2.4, the structure function of phase fluctuations, or simply *phase structure function*, (readily deducible from index of refraction fluctuations by Fermat's principle) is used, given by (Obukhov, 1949)

$$D_\phi(r) = < |\phi(r_0) - \phi(r_0 + r)|^2 > = 2.914 k^2 C_n^2 r^{5/3} \delta h, \tag{2.5}$$

This equation gives the average phase difference between two parallel rays of wave number $k = 2\pi/\lambda$ a distance r apart due to a turbulent layer with structure constant C_n^2 and thickness δh.In the so-called thin layer model, atmospheric turbulence is regarded as being concentrated in a (small) number of layers, usually a ground and a tropopausic layer, sometimes extended by several intermediate layers. At astronomical observation sites, this model is generally a fair approximation (see also Section 3.3); in reality however, the atmosphere should be regarded as a continuous turbulent medium, with the structure constant defined as a function of height h over the telescopes pupil, $C_n^2 = C_n^2(h)$.Thus, the integrated phase difference can be expressed as

$$D_\phi(r) = 2.914 k^2 \sec(z) \int_0^\infty dh C_n^2(h) r^{5/3}, \tag{2.6}$$

with notations as given above and the airmass $\sec(z)$ inserted to account for viewing directions other than vertical. This equation implies the introduction of the *Fried Parameter* r_0 (Fried, 1965) as

$$r_0 = \left(2.914 k^2 \sec(z) \int_0^\infty C_n^2(h) dh\right)^{-3/5}, \tag{2.7}$$

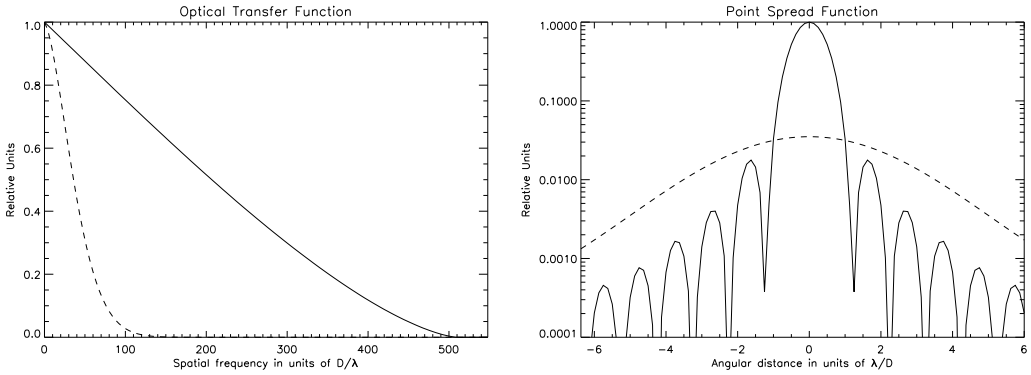

Figure 2.2: *Effects of turbulence on image quality for a circular aperture. OTF (left) and PSF (right) of diffraction limited (solid) and turbulence limited (slashes) imaging.* D/r_0 *was chosen to be 10, resulting in a Strehl ratio (see text) of 0.035 for the turbulence limited case.*

which allows Equation 2.6 to be rewritten:

$$D_\phi(r) = 6.88 \left(\frac{|\vec{r}|}{r_0} \right)^{5/3}. \tag{2.8}$$

The Fried parameter r_0 is a very useful quantity for the characterization of atmospheric turbulence since it has two quite intuitive physical interpretations: first, it gives the size of a (circular) aperture over which the root mean square (rms) of phase aberrations of the incident wavefront is about one radian; second, it defines the minimal diameter of a telescope that will deliver the maximal angular resolution for the given atmospheric conditions. At an observation wavelength of 500 nm, r_0 is usually in the range of 5 to 15 cm, much smaller than the typical size of astronomical telescopes. So, in uncorrected long-exposure observations, increasing the diameter of a telescope does not improve angular resolution but only sensitivity by enlarging the gathering area for incoming photons.
With the statistics of phase aberrations known, the effect of turbulence on image quality and telescope performance can now be examined. Two simple approximations and their consequences will be considered in the subsequent sections.

2.1.2 First Order Effects - Geometrical Optics

The first order approximation of imaging through a turbulent atmosphere relies wholly on geometrical optics, i.e. the diffraction of incident waves by turbulent structures is neglected; only the differential retardation of phase between adjacent rays due to the local differences in the index of refraction is taken into account. For good observation sites, this approximation already describes the major part of image degradations introduced by the atmosphere.

Optical Transfer Function

The imaging properties of an astronomical telescope can be fully described by the *optical transfer function* (OTF) of the system. In the case of imaging through turbulence the total OTF is described by the product of the telescopes' OTF $T(\vec{r})$, which is just the autocorrelation of its pupil function, and an

atmospheric OTF $A(\vec{r})$, defined by (Roddier, 1981)

$$A(\vec{r}) =< \exp\left(i[\phi(\vec{r}') - \phi(\vec{r}' + \vec{r})]\right) >= \exp\left[-\frac{1}{2}D_\phi(\vec{r})\right] \tag{2.9}$$

The PSF of the system is then given by the Fourier transform of the product $T(\vec{r})A(\vec{r})$. The quantity $D_\Phi(r)$ in equation 2.9 of course not only refers to the phase structure function given in equation 2.6 but to any phase structure function that can be defined on a telescope pupil. This will be of further importance when looking at partially corrected wavefronts as produced by adaptive optics systems. For the time being, figure 2.2 shows the effects of (Kolmogorov) turbulence on the imaging performance of an astronomical telescope with a circular aperture. In this example, the ratio D/r_0 has been chosen to be 10. As can be seen, the OTF drops to zero much faster than in the diffraction limited case, resulting in the filtering of high spatial frequencies. The consequence is that the peak intensity of the PSF is considerably flattened and its FWHM strongly increased. It should be noted that these results are valid for long-exposure imaging only, since,in equation 2.9, the ensemble average of phase aberration realizations is given. Short-exposure imaging depends very much on the momentary configuration of the phase in the pupil plane, which leads to an OTF that also transports high spatial frequency information. This fact is exploited by *Speckle imaging* techniques (Labeyrie, 1970), see also figure 2.4.

Strehl Ratio

Figure 2.2 also serves to introduce another useful quantity to characterize the performance of an imaging system: the *Strehl ratio* (Strehl, 1902). It is defined by the ratio of the actual peak intensity $I(p)$ to the theoretical (i.e. diffraction limited) peak intensity I_{th} of the PSF, $S = I(P)/I_{th}$. If the aberration function $\Phi(\rho, \theta)$ of an optical system is given, the Strehl ratio can be calculated via (Hardy, 1998)

$$S = \frac{1}{\pi^2}\left|\int_0^1\int_0^{2\pi} e^{ik\Phi(\rho,\theta)}\rho d\rho d\theta\right|. \tag{2.10}$$

A problem of this equation is that the aberration function has to be known explicitly, whereas in uncompensated and compensated astronomical imaging the phase fluctuations are at best known statistically. Therefore several simplifications of equation 2.10 have been found, notably the widely-used Marechal approximation given by

$$S \approx e^{-(\sigma_p)^2}, \tag{2.11}$$

where σ_p is the standard deviation of the phase over the aperture (Hardy, 1998). The Marechal approximation is valid up to an phase rms of about 2 rad. Turbulence degraded wavefronts are mostly well above this limit, hence a simple expression for this case is not available.

Anisoplanacy

Another important geometrical effect of imaging through a turbulent atmosphere is *angular anisoplanatism*. It is a consequence of the fact that rays from different viewing directions will pass through different sections of the atmosphere (see figure 2.3). While in uncompensated imaging anisoplanacy is only significant in short-exposure observations, it is a big problem for adaptive optics. Using equation 2.6 as a starting point and assuming $D >> r_0$, the mean-square error $< \sigma_\theta^2 >$ due to anisoplanacy can be calculated by replacing r with $r = \theta h \sec(z)$, where θ as shown in figure 2.3. This calculation yields

$$< \sigma_\theta^2 >= 2.914k^2(\sec(z))^{8/3}\theta^{5/3}\int_0^\infty dh C_n^2(h)h^{5/3}. \tag{2.12}$$

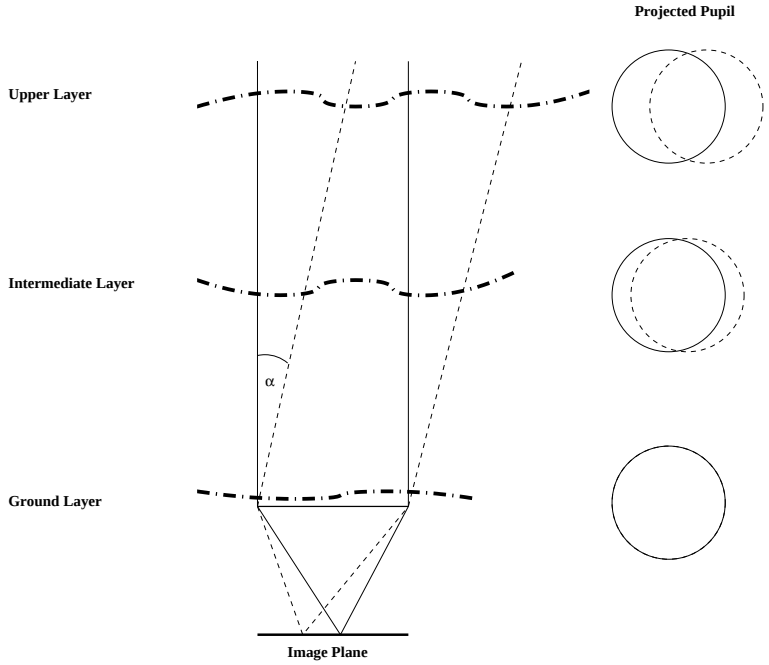

Figure 2.3: *The origin of anisoplanacy. Incident plane waves from directions that are an angle α apart pass through different sections of turbulent layers above ground.*

Similar to the definition of the Fried parameter, it is possible to define an angle θ_0 as

$$\theta_0 = \left[2.914k^2(\sec(z))^{8/3}\int_0^\infty dhC_n^2(h)h^{5/3}\right]^{-3/5}, \tag{2.13}$$

such that

$$< \sigma_\theta^2 >= \left(\frac{\theta}{\theta_0}\right)^{5/3}. \tag{2.14}$$

θ_0 is called the *isoplanatic angle*; its interpretation corresponds to that of r_0, defining the angular distance between two sources at infinity for which the difference in phase aberrations is approximately 1 rad. In contrast to the Fried Parameter, however, that is only dependent on the total integrated structure function, the isoplanatic angle shows a strong dependency on the vertical structure of the turbulence profile. As one would naively expect, high turbulent layers contribute strongly, while layers at or near ground level have virtually no influence on the differential error of two incident wavefronts.

To illustrate the effect of anisoplanacy on uncorrected imaging, the simulation package TURBULENZ (App. A) was used to calculate short and long exposure images of two stars about 12 arcseconds apart; the applied turbulence model was chosen such as to result in an isoplanatic angle of 8 arcseconds.

Figure 2.4 shows the results: while the short-exposure (speckle) images are clearly different, the overall shape and size of the long-exposure images is about the same. It is also visible that the speckle images contain much higher spatial frequencies than the integrated ones; the reason for which was already mentioned in section 2.1.1.

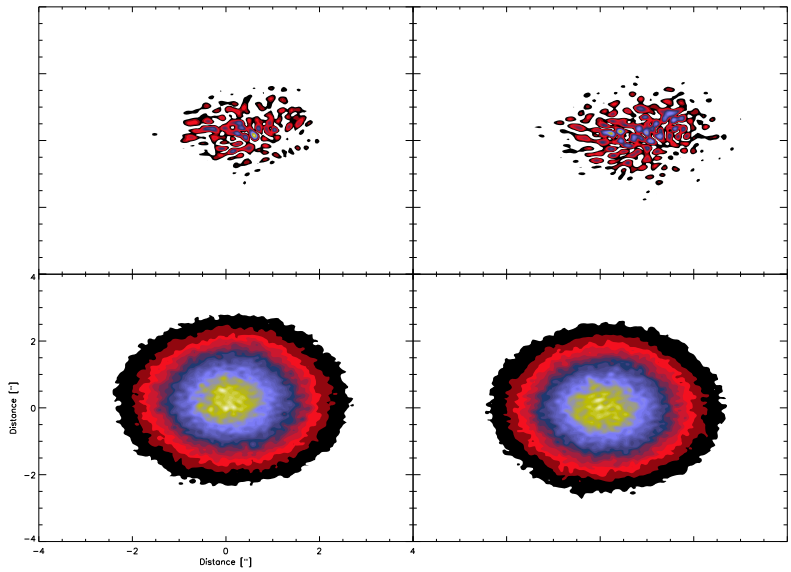

Figure 2.4: Short (top) and long-exposure (bottom) images of two stars 12 arcseconds apart in turbulent conditions corresponding to $\theta_0 = 8''$.

Temporal Effects

Up to now, the temporal evolution of turbulence was largely ignored, only ensemble averages of instantaneous realizations of phase disturbances were considered. Under real observing conditions, however, temporal effects cannot be disregarded.
Usually the validity of the Taylor hypothesis of frozen flow is assumed, stating that the structure of turbulence itself is fixed while the corresponding section of the layer is moving through the viewing area of the telescope. While this is generally a good approximation for smaller telescopes up to a pupil diameter of four meters, evolution of these structures does play a role for larger observatories. For a single layer moving at constant speed $\vec{v}$ the Taylor hypothesis can be formally stated by

$$\phi(\vec{x}, t + \delta t) = \phi(\vec{x} - \vec{v}\delta t, t), \tag{2.15}$$

resulting in a temporal phase structure function

$$D_\phi(\vec{v}, t) = < |\phi(\vec{x,t}) - \phi(\vec{x} - \vec{v}\delta t, t)|^2 > . \tag{2.16}$$

This equation translates temporal evolution into spatial distances. Note that this introduces anisotropy into the phase structure function, dependent on the direction of wind. If exposure times are short (or long) enough, however, these effects will be negligible. Long enough means that any correlations present on the medium time scale (several tens of ms) cancel out in the long-term limit, while short enough can be quantified by the *Greenwood frequency* f_G (Greenwood, 1977), a measure of the required bandwidth for any attempt to measure sensible wavefront aberrations. For a single turbulent layer, f_G is given by $f_G = 0.43v/r_0$, while for a turbulence distribution

$$f_g = \left[0.102k^2 \sec(z) \int_0^\infty dh C_n^2(h) |\vec{v}(h)|^{5/3}\right]^{3/5}, \tag{2.17}$$

with the vertical wind speed profile $\vec{v}(h)$ (Greenwood, 1976). As an example, typical tropopausic layer conditions with wind speeds on the order of $15\ m/s$ and an r_0 of $50\ cm$ in the K-Band result in a required bandwidth of 12.9 Hz, a demand easily met by modern sensors and control systems.

2.1.3 Second Order Effects - Scintillation and SCIDAR

Although the geometrical approximation described in the previous section already accounts for the major part of turbulence effects on imaging through the atmosphere, wave diffraction does of course also take place. Its most prominent influence on astronomical imaging is that of *scintillation*, the origin and features of which will be explained in this section. As turbulence at astronomical sites is generally quite weak, the so-called *Rytov approximation* can be used.

The Rytov Approximation

It has been shown quite early (Bergmann, 1946) that the assumption of geometrical optics is not sufficient if propagation path lengths are in excess of kl_0^2; then, diffraction effects at turbulent eddies have to be taken into account. In principle it would be necessary to solve the Maxwell equation

$$\nabla^2 E + k^2(1+\Delta n)^2 E - \nabla(\nabla E) = 0, \tag{2.18}$$

for the electric field E and the local deviation of the index of refraction from unity, Δn. Dropping the last term (depolarization) and substituting $E = \exp(\psi) = \exp(\chi + iS)$ yields

$$\nabla^2\psi + (\nabla\psi)^2 + k^2(1+\Delta n)^2 = 0. \tag{2.19}$$

Now, ψ is substituted by $\psi = \psi_0 + \psi_1$, where ψ_0 represents the non-fluctuating component (the incident wave) and ψ_1 describes fluctuation due to turbulence. If $|\nabla\psi_1|$ is neglected in comparison to $|\nabla\psi_0|$ and Δn^2 in comparison to $2\Delta n$ then ψ_1 satisfies

$$\nabla^2\psi_1 + 2\nabla\psi_0\nabla\psi_1 + 2k^2\Delta n \approx 0, \tag{2.20}$$

which has a solution given by Fante (1975)

$$\psi_1(r) = \frac{k^2}{2\pi E_0(r)} \iiint d^3r' \Delta n(r') E_0(r') \frac{\exp(ik|\vec{r}-\vec{r'}|)}{|\vec{r}-\vec{r'}|}, \tag{2.21}$$

where $E_0 = \exp(\psi_0)$. This solution has a much wider range of applicability than the geometrical one. It has been found (Gracheva et al., 1970) that if the propagation path is such that the Rytov variance $\sigma_r^2 = 1.23k^{7/6}C_n^2x^{11/6}$ is smaller than 0.3, the Rytov approximation is excellent. Equation 2.21 has a very simple physical interpretation that states that the Rytov approximation is equivalent to independent diffraction of the *incident* wave at a series of turbulent phase screens (Lee and Harp, 1969), i.e. inclusion of multiple diffraction is not necessary. A very important point to note is that the form of the phase structure function in equation 2.6 statistics is not changed at all, since the phase $\exp(\mathrm{Im}(\psi_1))$ is still proportional to Δn. The amplitude of an incident plane wave, however, which is constant under the geometrical approximation, is strongly affected; a closer look at the consequences will be taken in the subsequent paragraphs.

Intensity Fluctuations in an Aperture

Figure 2.5 shows intensity fluctuations in an image of the aperture of the Calar Alto 1.23m telescope. The best characterization of these fluctuations can be found by calculating the covariance of the logarithm of the amplitude fluctuations at two aperture locations $\vec{\rho_1}$ and $\vec{\rho_2}$,

$$B_\chi(\vec{\rho_1},\vec{\rho_2}) =< \chi_1(\vec{\rho_1})\chi_1(\vec{\rho_2}) >,$$

with $\chi_1(r) = \mathrm{Re}(\psi_1(r))$. $B_\chi(\rho_1,\rho_2)$ is related to the intensity fluctuations (Fante, 1975)

$$b_I(\vec{\rho_1},\vec{\rho_2}) = \frac{< I(\vec{\rho_1})I(\vec{\rho_2}) > - < I(\vec{\rho_1}) >< I(\vec{\rho_2}) >}{< I(\vec{\rho_1}) >< I(\vec{\rho_2}) >} \tag{2.22}$$

via

$$B_\chi(\vec{\rho_1},\vec{\rho_2}) = \frac{1}{4}\ln\left[1 + b_I(\vec{\rho_1},\vec{\rho_2})\right]. \tag{2.23}$$

For the case of an incident plane wave, B_χ is given by (Fante, 1975)

$$B_\chi(\vec{\rho}) = 4\pi^2 k^2 \int_0^\infty dx \int_0^\infty d\kappa\kappa J_0(\kappa\vec{\rho})\phi_n(\kappa,x)\sin^2\left[\frac{\kappa^2 x}{2k}\right], \tag{2.24}$$

with $\vec{\rho} = \vec{\rho_1} - \vec{\rho_2}$, spatial frequency κ, Φ as defined in equation 2.4, and x the distance of the turbulence from the aperture plane of the telescope.

Figure 2.6 plots the Rytov variance against the scintillation index σ_i for the Rytov theoretical results and experimental data (Fante, 1975). The theoretical results for an infinitesimally small aperture are obtained by calculating $\sigma_I^2 = \exp\left[4B_\chi(0,0)\right] - 1$ using equation 2.24. It is obvious that the Rytov approximation is in excellent agreement with measurements for $\sigma_1 << 1$ while it completely fails to describe the saturation behavior of scintillation in severe turbulence. However, astronomical sites usually are well below the upper limit of validity of the Rytov approximation (see also chapter 3.3). For completeness' sake it should be mentioned that analytical approximations for strong turbulence also exist, most notably the *Markov approximation* (Tatarski, 1971), which is e.g. used in calculation concerning horizontal laser beam propagation.

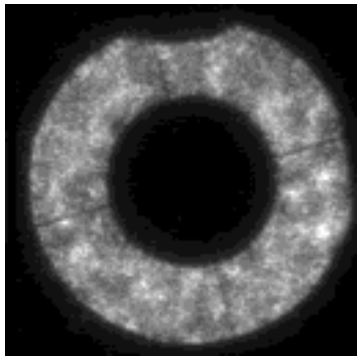

Figure 2.5: *Intensity fluctuations in the aperture plane of the Calar Alto 1.23m telescope.*

Effects on Imaging

Many of the relations presented in the previous paragraph are only valid for an infinitesimally small aperture. If effects of scintillation on imaging are considered, however, aperture averaging has to be taken into account. To derive the brightness fluctuations of the image of a star in the image plane of a telescope, one therefore calculates

$$< I^2 >= \iint_P d^2\vec{\rho_1} \iint_P d^2\vec{\rho_2} B_I(\vec{\rho_1},\vec{\rho_2}), \tag{2.25}$$

where integration is carried out over the pupil P of the telescope. Aperture averaging basically results in easing the effect of scintillation, since locations well inside the aperture do not contribute to the

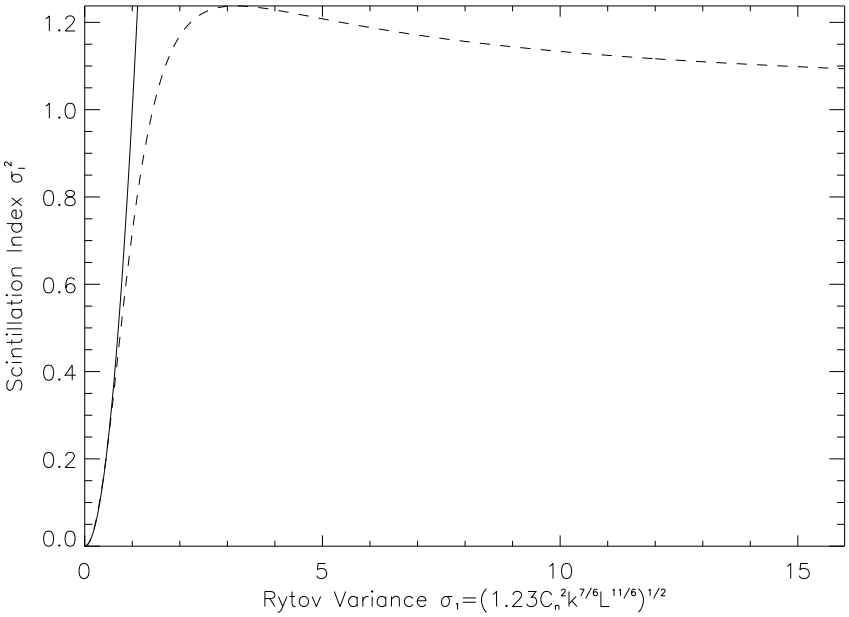

Figure 2.6: *Scintillation index measured in an infinitesimal aperture. Rytov approximation (solid) and fit to measured values (dashed).*

integrated brightness fluctuations any more. Only points near or at the fringe of the pupil have considerable influence; thus a significant reduction of the magnitude of fluctuations is expected for growing aperture size, a fact many times experimentally confirmed (Homstad et al., 1974).
Intensity fluctuations are, however, not the only effect of scintillations, a bigger problem is posed by their influence on the system OTF. Roddier and Roddier (1986) showed that even if phase aberrations caused by turbulence are perfectly removed, a performance degrading OTF term

$$A(\vec{r}) = \exp(-0.14 r_0^{-5/3} \sec(z)^{11/6} \lambda^{5/6} \int_0^\infty dh h^{5/6} P(h) I_1[|\vec{f}|(\cos(z/\lambda h))^{1/2}]), \tag{2.26}$$

remains, where $P(h)$ is the normalized $C_n^2(h)$ profile and

$$I_1(\rho) = \int_0^\infty dr r^{-8/3}[1 - J_0(2\pi r\rho)][\sin(\pi r^2)]^2, \tag{2.27}$$

with J_0 the Bessel function of order zero. Its overall effect is a limit on the maximum Strehl ratio obtainable by phase correction, given by the asymptotic value of the scintillation OTF term. For infrared imaging, this limitation is negligible, in the visual band it can be as low as 0.8.

2.1.4 Measuring $C_n^2(h)$: SCIDAR

The vertical structure of C_n^2 is the determining factor for many imaging distortions caused by the turbulent atmosphere. Therefore, it is highly desirable to obtain time-resolved information on it, either for image post-processing purposes or even for the selection of sites suitable for astronomical observatories. Although atmospheric sounding or weather balloons have been used to this end, another technique has proved its potential in this important task: Scintillation Detection and Ranging

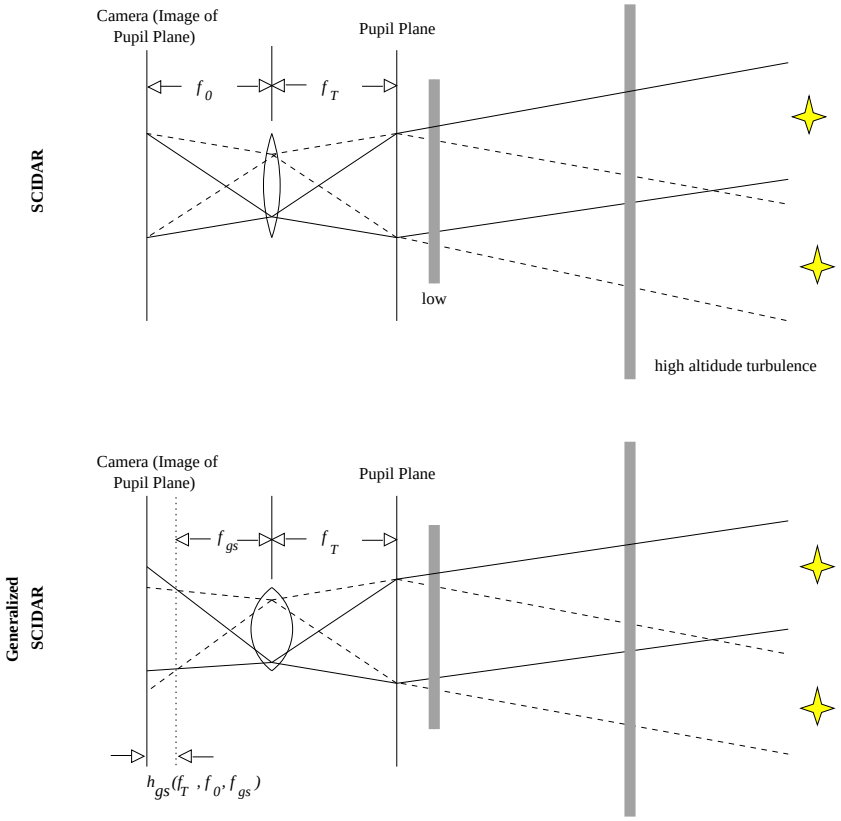

Figure 2.7: *Setup of a SCIDAR and a generalized SCIDAR system.*

(SCIDAR). The principle of this method was developed by Vernin and collaborators (Vernin et al., 1979) and has since been much enhanced, notably by the generalized SCIDAR approach (Fuchs et al., 1998). In this section, the setup of a typical SCIDAR system will be described before looking at the kind of data obtainable with such a device and the information on atmospheric turbulence derivable from it.

SCIDAR system setup and measurements

Figure 2.7 shows the configuration of a SCIDAR system. Its working principle builds on the amplitude variations imposed on plane waves imaged through the atmosphere, as described in the previous section. As shown in the figure, light originating from binary stars passes through different sections of the atmosphere. If the binary is chosen such that the cross-sections of the projected pupils overlap at all heights of interest, the spatial amplitude patterns of the overlap region as measured on the aperture will be the same albeit shifted by $\delta r = h\theta$ with respect to each other, with h the distance of the layer and θ the angular separation of the binaries. However, the amplitude variations comprising those patterns need a distance of a few kilometers to build up to a measurable signal, thus measuring turbulence near or at ground level is impossible with SCIDAR. Fuchs et al. (1998) found a way to overcome this limitation, by placing a different lens into the optical path such that the conjugate height of the observation plane is shifted from the pupil to a plane virtually below it (see figure 2.7). This extension is known as *generalized* SCIDAR.

With this extension done, the next step in measuring $C_n^2(h)$ consists of taking a large number of individual images of the virtual pupil with exposure times on the order of milliseconds (otherwise movements of the turbulent layers and their structural evolution would smear out the amplitude pattern). Subsequently, the mean-normalized auto-covariance of all the images is calculated. To illustrate the SCIDAR measurement process in a controlled setting, a simulation, again using TURBULENZ was carried out; the left image in figure 2.8 shows the result of the auto-covariance calculation for 1000 frames. The peaks visible in the left image are oriented in the direction of the binary's separation. A slice taken through the image in the separation direction can be written as (Klückers et al., 1998)

$$C_I(r,\theta) = \frac{L_1^2 + L_2^2}{(L_1+L_2)^2} b_I(r,0) + \frac{L_1 L_2}{(L_1+L_2)^2}[b_I(r,\theta) + b_I(r,-\theta)], \tag{2.28}$$

with the brightnesses B_1 and B_2 of the binaries' components, b_I being related to B_χ via equation 2.23. Another slice, taken perpendicular to the given one, contains only the first term of equation 2.28 and a noise estimate away from the origin; by subtracting it from the first slice, the first term in equation 2.28 can therefore be eliminated. Assuming the validity of the Rytov approximation, a relation between $B_\chi(r,\theta)$ and $C_n^2(h)$ can be found from equation 2.24 (Tyler, 1992)

$$\begin{aligned} B_\chi(r,\theta) = \int_0^\infty dh C_n^2(h) h^{5/6} \\ \int_0^\infty d\kappa \kappa^{-8/3} J_0\left(\frac{k}{h\sec(z)}^{1/2}(r - \theta h \sec(z))\kappa\right) \sin^2(\kappa^2) + n(r,\theta), \end{aligned} \tag{2.29}$$

where $\sec(z)$ is the airmass of the binary, $n(r,\theta)$ a noise term, everything else defined as before.

Obtaining $C_n^2(h)$ and $\vec{v}(h)$

Integration over κ in equation 2.29 can be done numerically. Using discrete sampling (e.g. by measuring amplitude fluctuations with a CCD), equation 2.29 corresponds to

$$\vec{p} = K\vec{x} + \vec{n}, \tag{2.30}$$

where $\vec{p}$ is the extracted auto-covariance profile, K a kernel matrix calculated from the κ integral, $\vec{n}$ the noise term and $\vec{x}$ the desired quantity, $C_n^2(h)$. This relation is analogue to a Fredholm equation of second kind (Press et al., 1993) and can therefore be solved by an iterative method. In this work, a conjugate gradients (CG) method was used, although different techniques have also been successfully applied (Avila, 1998).

Figure 2.9 and table 2.1 show the results of a simulated SCIDAR run with three turbulent layers at 0, 2 and 10 km distance from the aperture plane respectively. The data reduction was done using a SCIDAR software package, SCAVENGER (see app.B), that was developed in the context of this work. The "measured" parameters are obviously in very good agreement with the preset ones.

On the right-hand side of Figure 2.8 the cross-covariance of time-lagged aperture images is shown. The three layers are still clearly visible, but their positions are shifted according to the wind speed and wind direction in the respective layer. Table 2.2 lists the parameters used in the simulation together with those obtained from the cross-covariance. Again, these results are in very good agreement. Similar data reductions have been done for Calar Alto data and can be found in section 3.3.

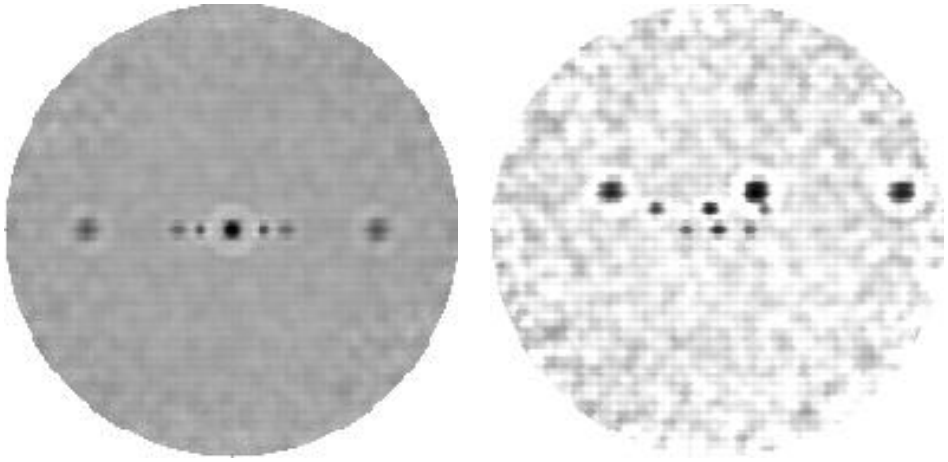

Figure 2.8: *Auto-covariance (left) and Cross-covariance (right) of a simulated three-layer turbulence SCIDAR measurement.*

	Model	Simulation
r_0 [m]	0.181	0.190 ± 0.013
θ_0 ["]	4.5	4.78 ± 0.33

Table 2.1: *Simulation settings of Fried parameter and isoplanatic angle compared to results obtained with* SCAVENGER

Limitations of SCIDAR

There are two main limitations to SCIDAR measurements: the first is the validity of the Rytov approximation, the second the finite size of the measuring aperture and its associated noise.
As already stated in section 2.1.3, the Rytov approximation is only valid if σ_r is lower than 0.3. This leads to a condition on $C_n^2(h)$

$$C_n^2(h) < 2.44k^{-7/6}x^{-11/6}, \tag{2.31}$$

where x is the distance from the measurement plane, implying $x = h\sec(z) + h_{gs}$ with zenith angle z and generalized SCIDAR pupil plane "depth" h_{gs}. Under all but exceptionally bad observing conditions, turbulence at astronomical sites is well below this limit, and hence does not pose a problem.
Additionally, the sensitivity of SCIDAR measurements is limited by the size of the receiving aperture, exposure time and star brightness. Prieur et al. (2001) found the noise per frame in SCIDAR measurements to be

$$\delta J_j(x) = \frac{5.23\ 10^{-2}\lambda^{5/3}x^{-5/6}d_0^{1/2}(C_2(0) + 1/N_{ph})}{BD\sqrt{\arccos(\theta x/D) - (\theta x/D)(1-(\theta x/D)^2)^{1/2}}}, \tag{2.32}$$

where d_0 is the distance of the dominant scintillation causing layer (identified by the highest peak in the reduced auto-covariance profile), $C_2(0)$ the center value of the unreduced auto-covariance, N_{ph} the number of photons received on the detector, D the pupil diameter, θ the separation of the binaries and a brightness ratio dependent factor B. This noise term results in a limitation of SCIDAR accuracy very close and very far away from the measurement plane.

		v [m/s]	Direction [Degrees]
Layer 1 (0 km)	Model	0.0	undef.
	Simulation	0.0	undef.
Layer 2 (2 km)	Model	4.80	-20.0
	Simulation	4.56 ± 0.29	$-21.95 \pm 1.63.$
Layer 3 (10 km)	Model	15.0	45.0
	Simulation	14.82 ± 1.24	46.3 ± 0.80

Table 2.2: *Simulation settings for wind speed and direction compared to results.*

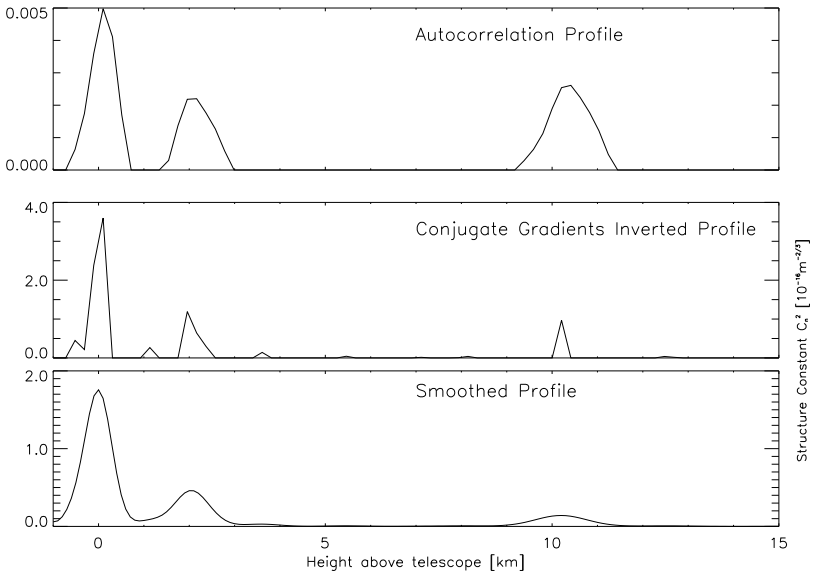

Figure 2.9: *Results of the SCIDAR simulation: Extracted autocorrelation profile (top), result of the conjugate gradient inversion (center), and final result smoothed with the instrumental resolution (bottom).*

As a summary, care has to be taken in selecting suitable binaries for SCIDAR measurements as well as using an appropriate generalized setup for the desired measurement range. Unfortunately, suitable binaries are not very abundant, which is why attempts are made to obtain C_n^2-profiles from single star measurements (Chun and Avila, 2002).

2.2 Adaptive Optics Systems

After getting acquainted to the source of imaging distortions caused by the atmosphere, it is now time to present the cure for some of its symptoms - adaptive optics. First, a quick look at the general setup of a pupil-conjugated AO system is taken. As most modern AO systems (including ALFA) use modal rather than zonal control for turbulence correction, the subsequent section will introduce this important concept, before continuing with a closer look at each of the system components.

2.2.1 General AO System Setup

The idea behind AO is to measure phase distortions introduced into the system by atmospheric turbulence and correct for them accordingly. The most widespread system today is that of a pupil-conjugated AO, i.e. phase is measured and corrected in the pupil plane of the receiving telescope. Figure 2.10 shows the schematic optical setup of such a system. A distorted wavefront is entering the telescope and is collimated to reconstruct the phase distribution in the aperture. It then hits a deformable mirror (DM) having (in the ideal case) the opposite shape of the distortions and therefore reconstructs a plane wave. After this the beam is parted by a beam splitter, one part moving on to be imaged by a science camera, the other being analyzed by a wavefront sensor (WFS) that checks for deviations from a plane wave. DM and WFS are connected to a real time control system (RTC) that uses the deviations as obtained from the WFS to adjust the DM accordingly.
In practice, a dichroic mirror is used instead of a beamsplitter, such that e.g. wavefront distortions are measured in the visible while the science camera images in the near infrared. This approach maximizes the amount of starlight available for wavefront measurements, a critical point in AO.

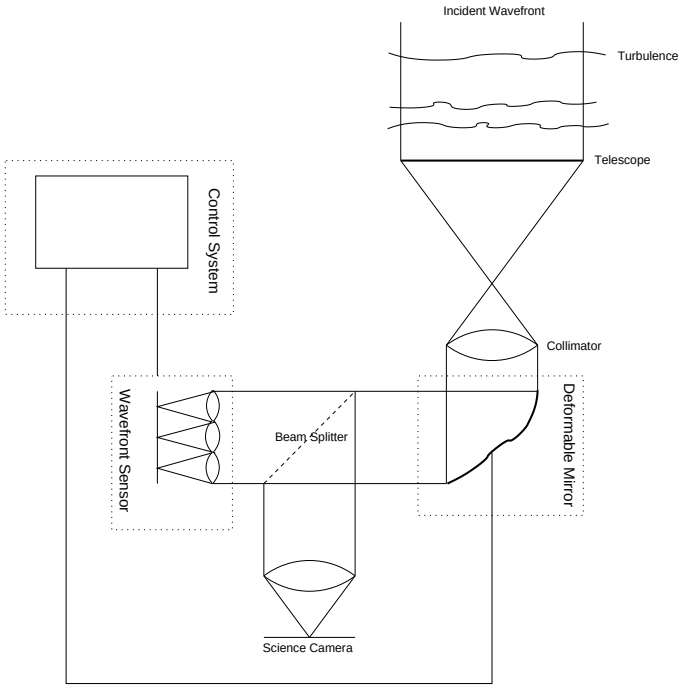

Figure 2.10: *Schematic optical setup of a pupil-conjugated AO system. Components treated in this text are marked with dashed boxes.*

2.2.2 Modal Decomposition of Phase Disturbances

The phase of a distorted wavefront incident on the pupil of a telescope can be described by a function $\phi(\vec{r},\vec{t})$. However, it is more convenient to decompose ϕ into a set of orthonormal basis functions $F_i(\vec{r})$ defined on the unit circle or an annular aperture,

$$\int d^2\vec{r} W(\vec{r}) F_i(\vec{r}) F_j(\vec{r}) = \delta_{ij}, \tag{2.33}$$

where $W(\vec{r})$ is the pupil weighting function, defined to be of constant value within the aperture and zero outside, such that an integration over the pupil is unity. With these functions every wavefront can be written as

$$\phi(\vec{r},t) = \sum_{i=0}^{\infty} a_i(t) F_i(\vec{r}), \tag{2.34}$$

which has the immediate advantage of separating time from space dependence. Due to the orthonormality property of the $F_i(\vec{r})$, the coefficients $a_i(t)$ are given by

$$a_i(t) = \int d^2\vec{r} W(\vec{r}) \phi(\vec{r},t) F_i(\vec{r}). \tag{2.35}$$

Since mostly the time average statistics of the coefficients are of interest, the explicit time dependence will be ignored in the subsequent discussions.

Zernike Polynomials

An obvious choice of the function set are *Zernike polynomials*, widely used in the optical community since the lowest order ones can be easily identified with well-known aberrations, like defocus, astigmatism etc. Their use in the context of atmospheric turbulence has first been examined by Noll (1976). The shape of the first ten Zernike polynomials $Z_i(\rho,\theta)$ is shown in figure 2.11.
Using the Kolmogorov turbulence model, the modal variance matrix of the coefficients $V_a =< a_i aj >$ over an aperture of radius R is given by

$$< a_i a_j >= \int d\vec{r} \int d\vec{r}' W(\vec{r}) W(\vec{r}') Z(\rho,\theta) < \phi(R\vec{r}) \phi(R\vec{r}') > Z_j(\rho',\theta'). \tag{2.36}$$

An analytical solution of this equation can be found by transforming to Fourier space and using equation 2.1 (Noll, 1976). Table 2.3 shows the result for the first ten Zernike polynomials, excluding piston and scaled to $(D/r_0)^{5/3} = 1$. An first approximation of the total variance of a turbulent wavefront in the telescope pupil is given by the trace of this matrix, $tr(\langle a_i a_j \rangle)$. Supposing that an AO system is capable of measuring and removing variance due to the first m Zernikes, an estimate of the maximum Strehl ratio obtainable by this (idealized) system can be found using equation 2.11

$$S = e^{-\sum_{j>m} <a_j a_j>} = e^{-\sigma^2(m)}. \tag{2.37}$$

Noll found an expression for $\sigma^2(m)$ asymptotically valid for large m

$$\sigma^2(m) \approx 0.2944 m^{-\sqrt{3}/2} \left(\frac{D}{r_0}\right)^{5/3}, \tag{2.38}$$

e.g. assuming a seeing of 1" in the visual (corresponding to an r_0 of 60 cm at 2.2μm), after removal of the first ten Zernike modes the residual variance is $0.0401(D/r_0)^{5/3}$, which gives a maximum Strehl

$$\begin{pmatrix}
0.448 & 0 & 0 & 0 & 0 & 0 & -0.0141 & 0 & 0 & 0 \\
0 & 0.448 & 0 & 0 & 0 & -0.0141 & 0 & 0 & 0 & 0 \\
0 & 0 & 0.232 & 0 & 0 & 0 & 0 & 0 & 0 & -0.0039 \\
0 & 0 & 0 & 0.232 & 0 & 0 & 0 & 0 & 0 & 0 \\
0 & 0 & 0 & 0 & 0.232 & 0 & 0 & 0 & 0 & 0 \\
0 & -0.0141 & 0 & 0 & 0 & 0.0062 & 0 & 0 & 0 & 0 \\
-0.0141 & 0 & 0 & 0 & 0 & 0 & 0.0062 & 0 & 0 & 0 \\
0 & 0 & 0 & 0 & 0 & 0 & 0 & 0.0062 & 0 & 0 \\
0 & 0 & 0 & 0 & 0 & 0 & 0 & 0 & 0.0062 & 0 \\
0 & 0 & -0.0039 & 0 & 0 & 0 & 0 & 0 & 0 & 0.0024
\end{pmatrix}$$

Table 2.3: Covariance matrix of the first ten Zernike polynomials. Values are given for $(D/r_0)^{5/3} = 1$.

ratio for a 3.5m telescope of 0.47. As the uncorrected Strehl ratio of such a telescope is usually on the order of 0.01 this is already a tremendous improvement in performance with only a comparatively small number of modes corrected. However, the marginal gain in performance with each additional corrected mode,

$$\frac{\partial S}{\partial m} \approx m^{-(\sqrt{3}+2)/2} S \tag{2.39}$$

is falling with approximately the square of the number of modes corrected.
All the results given above hold only for strict Kolmogorov turbulence conditions with an infinite outer scale. As already mentioned above, however, the Kolmogorov model is quite unrealistic. Winker (1991) calculated the effect of a finite outer scale on the Zernike decomposition of turbulence on a circular aperture; he basically found a strong influence on the first few terms of the expansion, leading to an altogether reduced variability in these contributions (ibid.); higher order terms are only marginally affected, implying an exclusive use of these parts of the expansion to derive atmospheric parameters defined in the Kolmogorov framework (like the Fried parameter) from measurements.
It should be mentioned that Zernike polynomials can be generalized from a circular support to an annular support, which is more adapted for use on modern astronomical telescopes (Mahajan, 1994), but an even more effective approach will be presented in the next paragraph.

Karhunen-Loeve functions

The non-zero off-diagonal elements of the Zernike covariance matrix in the context of Kolmogorov turbulence suggest that there exists a more efficient basis set; this efficiency is meant in the sense that fewer expansion terms represent the same or even higher amount of distortions introduced by turbulence. Following Wang and Markey (1978), such a basis can be found from a two-dimensional Karhunen-Loeve (KL) integral equation, defining the KL eigenfunctions $F_i(\vec{r})$ for the general covariance of a stochastic process,

$$\int d^2\vec{r'} W(\vec{r'}) F_i^*(\vec{r'}) \left\langle \phi(\vec{r'})\phi(\vec{r}) \right\rangle = \Lambda_i^2 F_i(\vec{r}), \tag{2.40}$$

where Λ_i^2 is the variance of the ith mode. KL functions for Kolmogorov statistics have been calculated by Wang and Markey (1978) for a circular and by Cannon (1996) for an annular support. The first ten

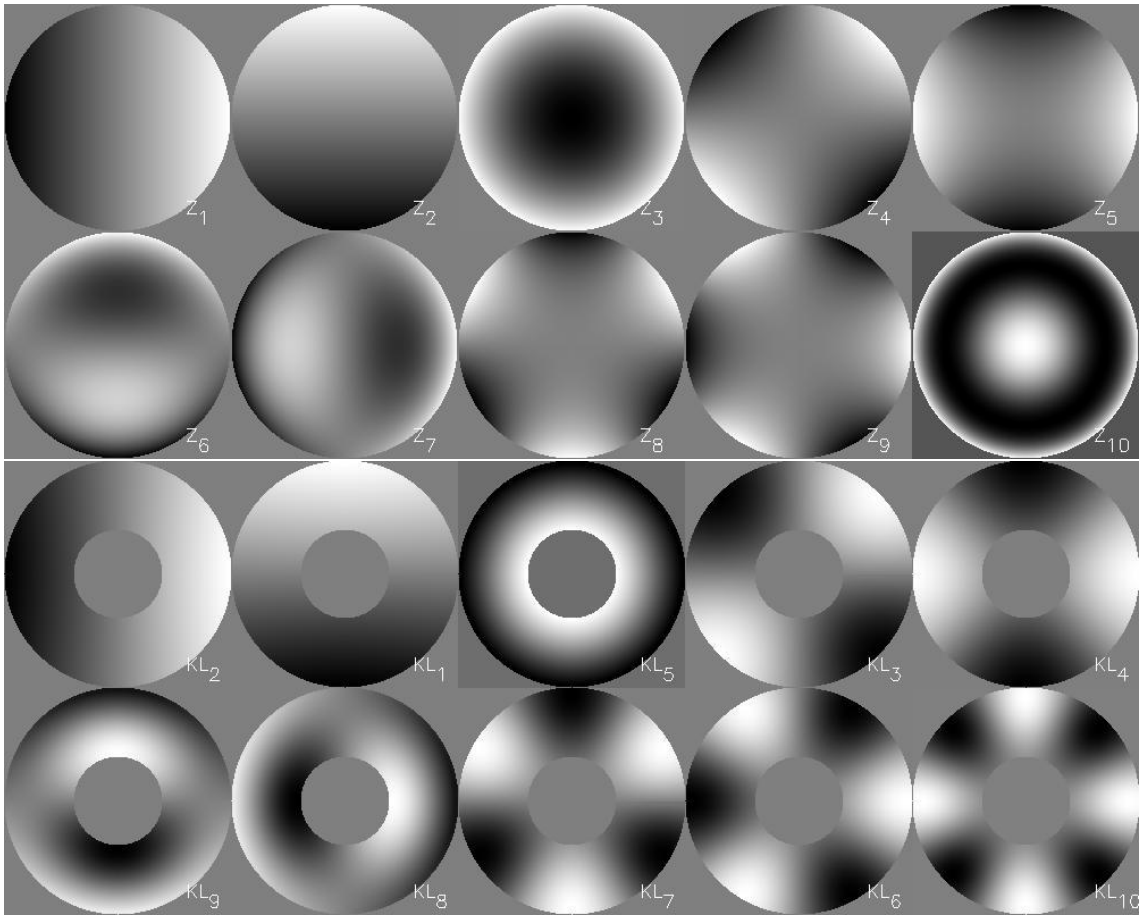

Figure 2.11: Images of the first ten circular Zernike (top) and KL (bottom) functions. KL functions are calculated for Kolmogorov turbulence conditions and an annular aperture with an inner radius $r_i = 0.39\frac{D}{2}$; additionally, they are reordered to show the similarity between the two function sets.

annular KL functions, a subset of those actually used in the ALFA system, are shown in Figure2.11, table 2.4 shows the normalized covariance matrix of the first KL functions calculated for the Calar Alto 3.5m telescope central obscuration and Kolmogorov turbulence; by definition, it is diagonal.

$$\begin{pmatrix}
0.515 & 0 & 0 & 0 & 0 & 0 & 0 & 0 & 0 & 0 \\
0 & 0.515 & 0 & 0 & 0 & 0 & 0 & 0 & 0 & 0 \\
0 & 0 & 0.0279 & 0 & 0 & 0 & 0 & 0 & 0 & 0 \\
0 & 0 & 0 & 0.0279 & 0 & 0 & 0 & 0 & 0 & 0 \\
0 & 0 & 0 & 0 & 0.0144 & 0 & 0 & 0 & 0 & 0 \\
0 & 0 & 0 & 0 & 0 & 0.0078 & 0 & 0 & 0 & 0 \\
0 & 0 & 0 & 0 & 0 & 0 & 0.0078 & 0 & 0 & 0 \\
0 & 0 & 0 & 0 & 0 & 0 & 0 & 0.0055 & 0 & 0 \\
0 & 0 & 0 & 0 & 0 & 0 & 0 & 0 & 0.0055 & 0 \\
0 & 0 & 0 & 0 & 0 & 0 & 0 & 0 & 0 & 0.0032
\end{pmatrix}$$

Table 2.4: Covariance matrix of the first ten KL functions for Kolmogorov conditions and $r_i = 0.39$. Values are given for $(D/r_0)^{5/3} = 1$.

2.2.3 Sensors

Phase aberrations can only be corrected if an efficient way of measuring them is found. Several types of sensors have been developed for that purpose. This section will focus on the Shack-Hartmann type sensor (SHS), widely used for its simplicity and also implemented into the ALFA system. After this, the curvature sensor (CWS) will be discussed, a relatively recent design (Roddier, 1988), that exhibited excellent performance in low order AO systems; PSF reconstruction from WFS data was first developed for this kind of sensor. The youngest type of sensor, beyond the scope of this work, is the pyramid sensor (PWS) that is only now being introduced into AO systems (Ragazzoni and Farinato, 1999) and promises to combine the advantages of the SHS and the CWS.

Shack-Hartmann Sensor

The principle behind the SHS was used as early as 1900 (Hartmann, 1900) to measure wavefront aberrations of optical systems. Then, masks with circular holes were placed behind a lens, with the images so obtained serving as a measure of local wavefront slopes. Shack and Platt (1971) improved the system by using small lenses (lenslets) instead of the holes and arrange them such that a whole wavefront could be examined. Figure 2.12 shows a SHS setup. A distorted wavefront enters from the left and sub-images are formed by the analyzing lenslets. If the average slope of the wavefront portion imaged by a subaperture is flat, then the image spot is not displaced with respect to its reference position, otherwise for the angular displacement α_x in the x-direction (Primot et al., 1990):

$$\alpha_x = \frac{\Delta x}{fF} = \frac{\lambda}{2\pi A_{sa}} \int_{A_{sa}} \frac{\partial \phi(\rho, \theta)}{\partial x} d\vec{r}, \tag{2.41}$$

and likewise for the displacement in the y direction. Here, A_{sa} denotes the area of the subaperture, Δx the spot displacement in the image plane, f the focal length of the lenslet, and F the magnification between the pupil of the sublenslet and the pupil of the telescope.

Equation 2.41 implies that a SHS measures the first derivative of the wavefront at the lenslet locations, thus information on a constant offset (piston) is completely lost. As a phase bias does not affect image quality, this is not a problem for conventional imaging; for interferometry, however, piston is a notorious complication of matters.

Measurement of the actual spot displacement in the image plane of the SHS can be done either by using quadcells (Roddier, 1999) or a CCD detector array. In the CCD case, spot position estimations are usually a modification of center of mass estimation

$$\Delta x = \frac{\sum_i x_i I_i}{\sum_i I_i}, \tag{2.42}$$

with pixel offset from the reference positions x_i and pixel intensity I_i. For a closed-loop system, estimation algorithms have to be both fast and accurate. In his PhD thesis, Kasper (2000) examined several such algorithms, finding a doubly weighted pixel averaging algorithm in combination with pixel masking to be most reliable and also very fast. The algorithm raises all intensity values to the 1.5th power, its expected SNR in the photon limited case, before applying equation 2.42. Additionally pixels with a low photon count are excluded from the weighting process.

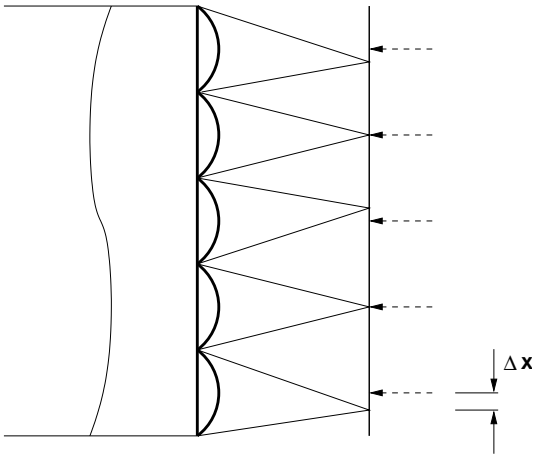

Figure 2.12: *Working principle of a Shack-Hartmann sensor.*

As the SHS averages over a given portion of a wavefront, it cannot "see" perturbations with spatial frequencies smaller than its sampling; it is therefore necessary to be careful in choosing the size of the subapertures, which in the ideal case should be matched to r_0; this is much easier accomplished in the infrared than in the visual regime. However, the number of photons available for centroiding a subspot also depends on subaperture size, which implies a choice of sensor parameters for given atmospheric conditions to attain the optimal results.

In contrast to other types of sensors, the SHS is also suitable for extended correction sources like planets or galaxy cores. Even the granulation on the photosphere of the sun has been successfully used to obtain diffraction-limited images (von der Lühe et al., 2002).

Curvature Sensor

The curvature sensor was invented by Francois Roddier (Roddier, 1988). The working principle is based on the fact that local curvature of a wavefront will, when imaged, cause the corresponding focal point to shift away from the focal plane of the imaging system. Hence, intensity measurements in planes before and after the image plane will find intensity differences corresponding to the curvature (see figure 2.13). Using a geometrical approximation, the normalized intensity differences are given by (Roddier, 1988)

$$c(\vec{r}) = \frac{I_1(\vec{r}) - I_2(\vec{r})}{I_1(\vec{r}) + I_2(\vec{r})} = \frac{f(f-p)}{2p}\left[\frac{\partial}{\partial\rho}\phi(\rho\theta)\delta_c - \nabla^2\phi(\rho\theta)\right], \tag{2.43}$$

with f and p as defined in figure 2.13, and δ_c the impulse distribution around the pupil edge. One of the advantages of the CWS over the SHS is that only intensities in subapertures have to be measured; no centroiding is necessary, which reduces the computational load in the control system. As will

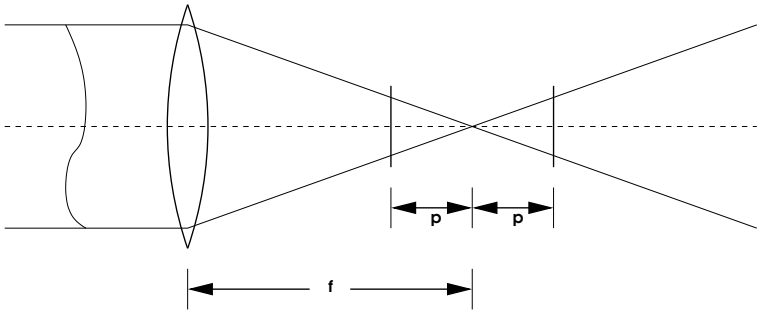

Figure 2.13: *Working principle of a curvature sensor.*

be seen in section 2.3, this also makes measurement noise estimation quite straightforward. Figure 2.14 shows the sampling geometry of a CWS. In practical implementations, a sinusoidally modulated mirror is used instead of two separate sensor planes, which considerably simplifies the setup of a CWS system (Roddier, 1988).

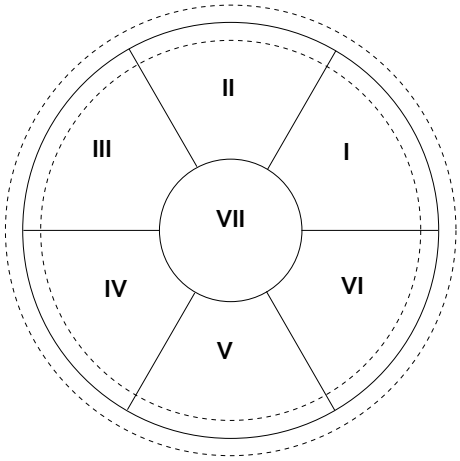

Figure 2.14: *Sampling geometry for a CWS sensor. The dashed lines depict the width of the impulse distribution around the edge of the pupil.*

Another interesting feature of the CWS is its adaptable gain. Equation 2.43 shows that the strength of the signal can be adjusted by varying the distance of the measurement planes p. The geometrical approximation demands that $\theta_b(f-p) < dp/f$, with θ_b the guide object angular size and d the size of the subaperture. Since d/f is usually much bigger than θ_b this can be further simplified to

$$p < \theta_b \frac{f^2}{d}. \tag{2.44}$$

In closed loop operation, θ_b will diminish due to correction and therefore allow the signal to be amplified by reducing the distance p, which will work to stabilize the loop.

Measurement noise

Of course all sensors will be subject to measurement noise, on the one hand caused by the signal photons themselves, on the other hand by sky background photons which, however, can be neglected for sensors measuring in the visual band. Rousset et al. (1993) showed that all WFSs operating with subapertures have a similar dependence on the signal photon noise

$$\sigma^2 \sim \frac{1}{n_{ph}} \left(\frac{\theta d}{\lambda} \right)^2, \tag{2.45}$$

with the phase measurement error variance σ^2, n_{ph} the number of photoelectrons per subaperture and exposure time, and d the diameter of the (circular) subaperture. θ refers to the angular size of the reference source, given either by its actual size, or its virtual size caused by seeing or diffraction. Usually, d and λ are fixed, so a better SNR is obtained by using bright and point-like sources and/or highly efficient photon sensors.

2.2.4 Modal Reconstruction

This section will concentrate on the mathematical description of modal phase distortion measurements and reconstruction using a SHS.
As described before, a SHS delivers slope measurements of sections of a disturbed wavefront according to its geometry. These slopes, in x- and y-direction, can be ordered into a n-dimensional *gradient vector* $\vec{g}$, (with $n = 2n_{sub}$, twice the number of subapertures) describing the set of measurements for each timestep. Of course, the actual values of such a vector will depend on the momentary configuration of the turbulent wavefront; but as became clear in the framework of modal decomposition, this wavefront can also be regarded as a (generally infinite-dimensional) *modal coefficient vector* $\vec{a}_\infty$. A measurement can then be written as

$$\vec{g} = \mathbf{D}_\infty \vec{a}_\infty + \vec{n}, \tag{2.46}$$

with the *interaction matrix* $\mathbf{D}_\infty$ and the unavoidable measurement noise vector $\vec{n}$. The interaction matrix as defined here is of dimension $\infty \times n$, very inconvenient for practical calculations. This fact is remedied by partitioning equation 2.46 as follows

$$\vec{g} = \mathbf{D}\vec{a} + \mathbf{D}_\perp \vec{a}_\perp + \vec{n}, \tag{2.47}$$

where $\mathbf{D}$ denotes a reduced interaction matrix operating on a number of m modes $\vec{a}$, which are actually controlled by the system. $\mathbf{D}_\perp$ is again an infinite matrix, describing the propagation of the non-controlled modes $\vec{a}_\perp$ on the gradients. This is justified by the fact that all AO systems can only correct for a limited number of modes and, additionally, that this number is generally limited by the number of available gradients.

Phase Estimation from Gradient Measurements

The modified measurement equation can even be more simplified by observing that, since modal coefficients are normally distributed with zero mean (Roddier, 1981), the expression $\mathbf{D}_\perp \vec{a}_\perp$ corresponds to an additional Gaussian noise term. This measurement noise $\vec{n}$ and this noise therefore form again a Gaussian noise term $\vec{e}$, leading to the final measurement equation

$$\vec{g} = \mathbf{D}\vec{a} + \vec{e}. \tag{2.48}$$

For the operation of an AO system, where an estimate of the controlled modal coefficients $\hat{\vec{a}}$ has to be found from the measured value of gradients, this poses an inverse problem

$$\hat{\vec{a}} \approx \mathbf{R}\vec{g} \tag{2.49}$$

with a $n \times m$ reconstruction matrix $\mathbf{R}$. Kasper (2000) extensively studied the suitability of different approaches to find such a matrix. The superior and most general non-iterative solution turned out to be the *Maximum a Posteriori* approach (Melsa and Cohn, 1978), which gives (Law and Lane, 1996)

$$\mathbf{R}_{MAP} = \left(\mathbf{D}^T \mathbf{V}_{\vec{e}}^{-1} \mathbf{D} + \mathbf{V}_{\vec{a}}^{-1}\right)^{-1} \mathbf{D}^T \mathbf{V}_{\vec{e}}^{-1}, \tag{2.50}$$

where $\mathbf{V}_{\vec{e}}$ is the noise covariance matrix and $\mathbf{V}_{\vec{a}}$ is the covariance matrix of modal coefficients. Both matrices will be examined more closely below.
More simple estimators can be found directly from expression 2.50, by dropping various terms: assuming that no prior knowledge is available on the covariance of modal coefficients, setting $\mathbf{V}_{\vec{a}}^{-1} = 0$ results in the *weighted least squares* estimate

$$\mathbf{R}_{WLS} = \left(\mathbf{D}^T \mathbf{V}_{\vec{e}}^{-1} \mathbf{D}\right)^{-1} \mathbf{D}^T \mathbf{V}_{\vec{e}}^{-1}. \tag{2.51}$$

If additionally, the measurement error is assumed to be uniform and uncorrelated equation 2.51 reduces to

$$\mathbf{R}_{LS} = \left(\mathbf{D}^T\mathbf{D}\right)^{-1}\mathbf{D}^T, \tag{2.52}$$

the *least squares* estimator, most widely used in AO for its simplicity. The least squares estimator is closely connected to the *singular value decomposition* (SVD) technique (see e.g. Gershenfeld (1999)). The framework of SVD also allows to study a limitation imposed on SHS type system, called *modal cross talk*, which limits the number of controllable modes due to possible misinterpretation of linear combinations of higher order modes as a single low order mode (Kasper et al., 2000b). In the case of ALFA, this modal cross talk allows a maximum of 42 modes corrected when using a 28 subaperture lenslet and KL functions are used; for Zernike polynomials, the limitations are even worse.

Modal reconstruction error

Using the least squares estimator and turning back to equation 2.48, the covariance matrix of the reconstruction error is given by (Dai, 1996)

$$\left\langle (\vec{a}-\hat{\vec{a}})(\vec{a}-\hat{\vec{a}})^T \right\rangle = \mathbf{C}\left\langle \vec{a}_\perp \vec{a}_\perp^T \right\rangle \mathbf{C}^T + \mathbf{R}_{LS}\left\langle \vec{n}\vec{n}^T \right\rangle \mathbf{R}_{LS}^T, \tag{2.53}$$

with the *cross-talk matrix* $\mathbf{C} = \mathbf{R}_{LS}\mathbf{D}_\perp$. It is a description of the propagation of high-order modes on the low-order controlled modes, an effect generally termed *aliasing*. Thus, the two terms in the reconstruction error matrix correspond to aliasing noise and propagated measurement noise respectively. The behavior of the two noise components is quite different: while measurement noise can be diminished by choosing very bright guide stars, aliasing noise is always present; as will be seen, it therefore plays an important role in the framework of PSF reconstruction.
Unfortunately, $\mathbf{D}_\perp$ cannot be calculated analytically for most sensor/modal basis set combinations, and measurement is impossible for obvious reasons. Therefore, it can only be found by a simulation of the sensor measurement process.

Estimation of the modal covariance matrix

The MAP estimator already emphasizes the importance of the Modal Covariance Matrix $\mathbf{V}_{\vec{a}}$. This importance lies in the fact that it carries all information on stochastic properties of the turbulent spectrum at hand, because ensemble averages of wavefront disturbances are Gaussian with zero mean (Roddier, 1981). The knowledge of this matrix is not only crucial for the application of the MAP estimator, but also provides atmospheric turbulence parameters like r_0 and can be used for an estimation of the outer scale size (Barchers and Ellerbroek, 1999).
There is a fundamental difference between the modal covariance matrix as obtained from open- versus closed-loop measurements: while in the open-loop case it, ideally, delivers accurate information on the turbulence present in the atmosphere, the closed-loop measurements will provide the characteristics of the *modified* atmospheric spectrum as caused by the interplay of actual turbulence and the AO system. The starting point is the estimation equation

$$\hat{\vec{a}} = \mathbf{R}\mathbf{D}\vec{a} + \mathbf{R}\mathbf{D}_\perp\vec{a}_\perp + \mathbf{R}\vec{n}, \tag{2.54}$$

which, using the LS estimator results in

$$\hat{\vec{a}} = \vec{a} + \mathbf{C}\vec{a}_\perp + \mathbf{R}_{LS}\vec{n}. \tag{2.55}$$

Now, if $\vec{n}$ is assumed to be uncorrelated (as it should be in a well-setup system) and cross-correlations between $\vec{n}$ either $\vec{a}$ and $\vec{a}_\perp$ are neglected (justified by the delay in every real control system, see below), the modal covariance matrix is given by

$$\mathbf{V}_{\vec{a}} = \left\langle \vec{a}\vec{a}^T \right\rangle = \left\langle \hat{\vec{a}}\hat{\vec{a}}^T \right\rangle - \mathbf{R}_{LS} \left\langle \vec{n}\vec{n}^T \right\rangle \mathbf{R}_{LS}^T - \mathbf{C} \left\langle \vec{a}_\perp \vec{a}_\perp^T \right\rangle \mathbf{C}^T - \left\langle \vec{a}\vec{a}_\perp^T \right\rangle \mathbf{C}^T - \mathbf{C} \left\langle \vec{a}_\perp \vec{a}^T \right\rangle . \quad (2.56)$$

If the bandwidth of the system is high enough, it is perfectly justified to drop the two cross-correlation terms in this expression (Veran et al., 1997), thus yielding in the open-loop case (Kasper, 2000)

$$\mathbf{V}_{\vec{a},op} \approx \left\langle \hat{\vec{a}}\hat{\vec{a}}^T \right\rangle - \mathbf{R}_{LS} \left\langle \vec{n}\vec{n}^T \right\rangle \mathbf{R}_{LS}^T - \mathbf{C} \left\langle \vec{a}_\perp \vec{a}_\perp^T \right\rangle \mathbf{C}^T . \quad (2.57)$$

The closed-loop case differs only in the sign of the aliasing noise (Veran et al., 1997)

$$\mathbf{V}_{\vec{a},cl} \approx \left\langle \hat{\vec{a}}\hat{\vec{a}}^T \right\rangle - \mathbf{R}_{LS} \left\langle \vec{n}\vec{n}^T \right\rangle \mathbf{R}_{LS}^T + \mathbf{C} \left\langle \vec{a}_\perp \vec{a}_\perp^T \right\rangle \mathbf{C}^T . \quad (2.58)$$

The sign change can be illustratively explained by the differences of open- and closed-loop operation; in open-loop, high-order modes will tend to add to the measurements of the low-order modes at each time step and thus overestimate their energy, while in closed-loop, the system (over-)compensates for the perceived low-order modes and thus tends to underestimate their energy.
In principle, all of the quantities in equations 2.57 and 2.58 are deducible from the system. $\hat{\vec{a}}$ can be calculated from the sensor measurements, while the recovery $\vec{n}$ for SHS systems is one of the subjects of this work (see section 3.2). The calculation of $\mathbf{C}$ requires knowledge of $\mathbf{D}_\perp$, which is usually retrieved by modeling system response, as mentioned above. The covariance matrix of the non-controlled modes $\left\langle \vec{a}_\perp \vec{a}_\perp^T \right\rangle$ is not directly measurable and thus assumed to follow Kolmogorov statistics. Its contribution can be found by scaling the theoretical covariance matrices (tables 2.3 and 2.4) with r_0. This leaves the problem of finding r_0, derivable by an iterative algorithm from open-loop modal measurements (Kasper, 2000):

1. Assume $r_0 = \infty$,
2. calculate $\left\langle \vec{a}\vec{a}^T \right\rangle$ using equation 2.57,
3. estimate r_0 from the result of step 2 and the theoretical covariance matrix,
4. iterate from step 2 until convergence of r_0.

A similar scheme can be employed in the case of closed-loop operation, as will be seen below.
As a final note, $\mathbf{V}_{\vec{a}}$ as obtained from equation 2.58 can be reentered directly into a MAP estimator, since it delivers the closed loop statistics of the controlled mode. Unfortunately, for better results, the MAP should be extended to non-controlled modes to yield superior results, which again requires an estimation of the atmospheric r_0.

2.2.5 Control System

In the discussions above, there were frequent references to the control component of an AO system, without giving further detail. This will now be made up for. While the discussion is already based on ALFA's control architecture, technical details will only be given in section 3.1.
Most, if not all, AO systems to date are based on the principle of *feed-back control*, in which the controlled quantity is reintroduced into the loop through sensor measurements. Figure 2.15 show the

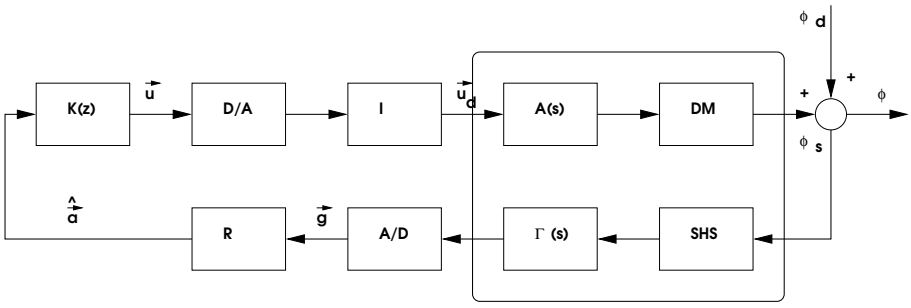

Figure 2.15: Feedback control system architecture used for ALFA. The box indicates the open-loop components.

control system architecture employed in ALFA. The output of the system ϕ on the right, is the sum of the disturbed wavefront ϕ_d entering from the atmosphere an the momentary shape of the DM ϕ_s. This wavefront is then analyzed by the SHS, delivering measured gradients $\vec{g}$, from which estimates of the momentary residual modal aberration $\hat{\vec{a}}$ are calculated via the reconstruction matrix $\mathbf{R}$ as described above. The estimates now enter the actual controller, or *compensator* $K(z)$ which determines appropriate modal drive signals $\vec{u}$ that are, after being translated to a suitable format $\vec{u}_d$ via a D/A and a so-called *injection matrix* $\mathbf{I}$, sent to the DM, where the cycle starts over. Of course, all operation take a finite amount of time, and thus have to be represented by transfer functions describing its dynamics, the *actuator transfer function* $A(s)$ describing the response of the DM to driving signals, and $\Gamma(s)$, considering the combined effects of integration time on the SHS, centroiding, and calculation of the compensation signals. Note that s and z refer to the Laplace and z-transforms, frequently used in control system theory (Dorf and Bishop, 2001). Details on the shape of the transfer function in the case of the ALFA control system can be found in Looze et al. (1999).
The compensation algorithm implemented in AO systems is often a variant of the so-called PID-controller, where the letters stand for *proportional*, *integration*, and *differentiation* respectively. This means, that the compensation signal will depend proportionally on the actually measured signal (usually either amplified or dampened by a *gain* g), but also in certain ways on the integrated past signal and the difference of subsequent ones. The overall effect of such a control system on a disturbed signal (such as an individual mode in modal control) is conveniently described in the Fourier domain. A very important concept in this context is that of the correction transfer function $h_{cor}(f)$ and the noise transfer function $h_n(f)$, which can be found either experimentally or analytically from the impulse response of a control system (Abramovici and Chapsky, 2000). Since the power spectral density (PSD) of a signal is directly related to its variance via integration, the calculation of the closed-loop PSD allows a direct estimate of the performance of the control system. If $P_{res}(f)$ denotes the residual PSD of a controlled mode after compensation of the atmospheric signal PSD $P_{atm}(f)$ and noise, in turn described by a PSD $P_n(f)$, then (Gendron and Lena, 1994)

$$P_{res}(f) = |h_{cor}|^2 P_{atm}(f) + |h_n|^2 P_n(f). \tag{2.59}$$

Additionally, the noise and correction transfer functions are related by

$$h_{cor}(f) \approx 1 - h_n(f). \tag{2.60}$$

Figure 2.16 shows the modulus of $h_{cor}(f)$ and $h_n(f)$ for various loop gain factors. As can be seen, the control loop strongly attenuates the energy at the low-frequency end of the temporal spectrum, an

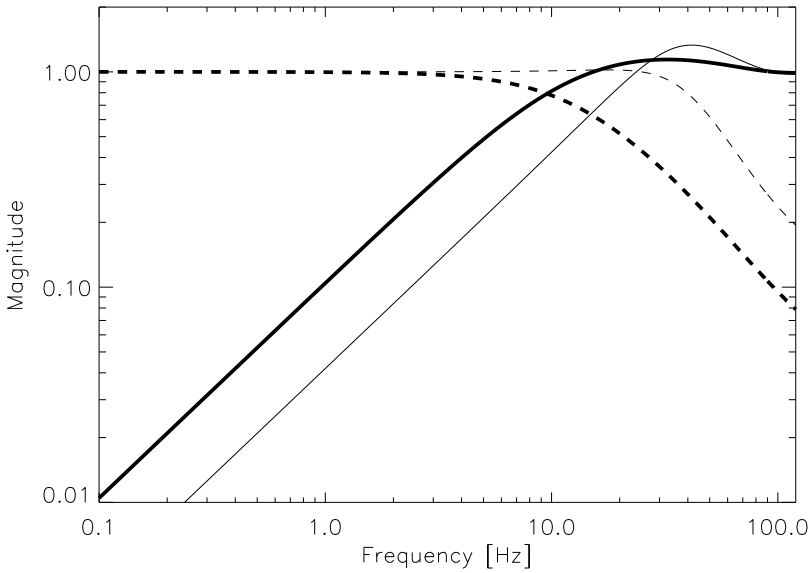

Figure 2.16: Modulus of the correction (solid) and noise (dashed) transfer functions of the ALFA control system for a gain of 0.5 (thin) and 0.2 (fat).

effect which can be even increased by using a higher gain. However, the trade-off is an amplification of energy to the high-frequency end. This control loop behavior is perfectly adapted to the temporal spectrum of atmospheric turbulence in modal control, which shows high energy at low frequencies and a steep fall-off toward higher frequencies (Conan et al., 1995).

2.3 Point Spread Function Reconstruction

The introduction already pointed out that the temporally and spatially varying PSF of pupil-oriented AO limits the scientific use and accuracy of astronomical images obtained with its help. Here, the means to overcome this limitation will be discussed: on- and off-axis PSF reconstruction from WFS data.
On-axis PSF estimation was originally developed for a system employing a curvature type WFS (Veran et al., 1997). Some of the techniques used there cannot be readily applied to an SHS AO, although some steps in this direction have already been taken for the ADONIS instrument (Harder and Chelli, 2000).
This section will first introduce the underlying principles for on-axis PSF reconstruction, before discussing the off-axis extension as introduced by (Fusco et al., 2000). A review of the example given in the introductory chapter will show that - under ideal circumstances - these techniques offer a considerable improvement of the current situation.

2.3.1 Principles: The Long-Exposure OTF

Section 2.1.2 introduced the concept of the long-exposure OTF for an astronomical telescope, from which the PSF can be obtained by a simple Fourier transformation. It was already mentioned that the used phase structure function $D_\phi(\vec{r})$ was not limited to Kolmogorov or von Karman type spectra alone. If the structure function of the residual phase for an operating AO system is introduced as

$$D_{\phi_\epsilon}(\vec{r},\vec{\rho}) = \left\langle |\phi_\epsilon(\vec{r},t) - \phi_\epsilon(\vec{r}+\vec{\rho},t)|^2 \right\rangle, \tag{2.61}$$

it could serve as a basis for an estimate of the system's PSF. The quantity ϕ_ϵ denotes the residual phase entering the AO system, given by

$$\phi_\epsilon(\vec{r},t) = \phi_d(\vec{r},t) - \phi_s(\vec{r},t), \tag{2.62}$$

with notations as above (figure 2.15). However, the explicit dependence on $\vec{r}$ in equation 2.61 poses a problem, since simple multiplication with the telescope OTF is not possible anymore. Fortunately, D_{ϕ_ϵ} can be replaced by its mean over $\vec{r}$

$$\bar{D}_{\phi_\epsilon}(\vec{\rho}) = \frac{\iint P(\vec{r})P(\vec{r}+\vec{\rho})D_{\phi_\epsilon}(\vec{r},\vec{\rho})d\vec{r}}{\iint P(\vec{r})P(\vec{r}+\vec{\rho})}, \tag{2.63}$$

where $P(\vec{r})$ is the telescopes pupil function, one inside the aperture and zero outside. With this replacement, the total OTF B_{tot} of the system becomes

$$B_{tot}(\vec{\rho}) = \exp\left[-\frac{1}{2}\bar{D}_{\phi_\epsilon}(\vec{\rho})\right] T(\vec{\rho}), \tag{2.64}$$

where $T(\vec{\rho})$ is the telescope OTF as introduced in section 2.1.2. Now, following similar lines as in the discussion of modal reconstruction, ϕ_d can be decomposed into a part $\phi_{d||}$ that is controlled by the system (low-order modes) and a part $\phi_\perp$ that is not (high-order modes):

$$\phi_d(\vec{r},t) = \phi_{d||}(\vec{r},t) + \phi_\perp(\vec{r},t). \tag{2.65}$$

From this, the residual phase of the part controlled by the system follows as:

$$\phi_{\epsilon||}(\vec{r},t) = \phi_{d||}(\vec{r},t) - \phi_s(\vec{r},t). \tag{2.66}$$

By entering this decomposition into equation 2.63, $\bar{D}_{\phi_\epsilon}$ can be written as (Veran et al., 1997)

$$\bar{D}_{\phi_\epsilon}(\vec{\rho}) = \bar{D}_{\phi_{\epsilon||}}(\vec{\rho}) + \bar{D}_{\perp}(\vec{\rho}) + F(\phi_{\epsilon||}, \phi_{\perp}), \tag{2.67}$$

with the last term depending on correlations between $\phi_{\epsilon||}$ and $\phi_{\perp}$, which are generally very small or even zero, depending on the modal function set used. At the very least, they can be neglected in comparison to the other contributions (Harder and Chelli, 2000). So, the final OTF consists of three components,

$$B_{tot}(\vec{\rho}) = B_{\epsilon||}(\vec{\rho}) B_{\perp}(\vec{\rho}) T(\vec{\rho}), \tag{2.68}$$

with the contribution of the non-controlled high-order phase aberrations $B_{\perp}(\vec{\rho})$ and the residual phase of the controlled low-order aberrations $B_{\epsilon||}(\vec{\rho})$.
It is now possible to go back to the modal decomposition approach of section 2.2. Supposing a modal set $\{F_i\}$, with m controlled modes, the atmospheric signal ϕ is

$$\phi(\vec{r}, t) = \sum_{i=1}^{m} \epsilon_i(t) F_i(\vec{r}) + \sum_{j=m+1}^{\infty} a_{j\perp}(t) F_j(\vec{r}). \tag{2.69}$$

Note that $\vec{\epsilon} := \vec{a}$ is used to denote the controlled modes, to emphasize the fact that in a closed-loop a system these quantities should be small and residual. The two first terms of equation 2.67 are now given by

$$\bar{D}_{\phi_{\epsilon||}}(\vec{\rho}) = \sum_{i,j}^{m} \left\langle \vec{\epsilon}\vec{\epsilon}^T \right\rangle U_{ij}(\vec{\rho}), \tag{2.70}$$

and

$$\bar{D}_{\phi_{\perp}}(\vec{\rho}) = \sum_{i,j}^{i,j>m} \left\langle \vec{a}_{\perp}\vec{a}_{\perp}^T \right\rangle U_{ij}(\vec{\rho}), \tag{2.71}$$

where the U_{ij} depend on the used modal basis set and can be calculated using

$$U_{ij}(\rho) = \frac{\iint P(\vec{r}) P(\vec{r}+\vec{\rho}) \left[F_i(\vec{r}) - F_i(\vec{r}+\vec{\rho})\right] \left[F_j(\vec{r}) - F_j(\vec{r}+\vec{\rho})\right] d\vec{r}}{\iint P(\vec{r}) P(\vec{r}+\vec{\rho}) d\vec{r}.} \tag{2.72}$$

For some modal basis sets, notably Zernike and KL functions on a circular support, these functions have been calculated analytically (Dai, 1995); as most telescopes have a central obscuration, these analytical solutions have only limited use. Therefore, it is necessary to calculate them numerically. As will be seen in chapter 3.4, it is sufficient to use only the first 237 U_{ij} of a basis set, since errors in other quantities of the reconstruction process are by far dominant above a certain spatial frequency.
The telescope OTF, the last term in equation 2.68 is not only the autocorrelation function of the telescope pupil, but can also account for any static aberration in the system occurring in the light-path after the DM. This is important, since static aberrations before the DM are corrected by the AO, as if caused by the atmosphere, aberrations after the dichroic mirror are, however, "out of reach". So, in a measurement setup:

Static Aberrations:
The telescope component of the system OTF, $T(\vec{\rho})$ is obtained by measuring a reference source, like a fiber or a very bright guidestar for which correction is nearly perfect. Fourier transforming its PSF gives the desired OTF.

2.3.2 From WFS measurements to the On-axis PSF

The formulation of the contributions of the residual of the controlled modes to the closed-loop PSF in equation 2.70 points directly to equation 2.58, which is also valid here:

$$\left\langle \vec{\epsilon}\vec{\epsilon}^T \right\rangle \approx \left\langle \hat{\vec{\epsilon}}\hat{\vec{\epsilon}}^T \right\rangle - \mathbf{R}_{LS} - \left\langle \vec{n}\vec{n}^T \right\rangle \mathbf{R}_{LS}^T + \mathbf{C} \left\langle \vec{a}_\perp \vec{a}_\perp^T \right\rangle \mathbf{C}^T. \tag{2.73}$$

Again, while $\left\langle \hat{\vec{\epsilon}}\hat{\vec{\epsilon}}^T \right\rangle$ is directly available from the WFS measurements and R_{LS}, there remains the problem to determine the measurement noise covariance matrix $\left\langle \vec{n}\vec{n}^T \right\rangle$ and the contribution of aliasing to the desired quantity.
In the original paper (Veran et al., 1997), it was proposed to deduce the noise covariance matrix directly from Poisson noise estimates of the Avalanche Photo Diodes (APD) used in the curvature system. This scheme is not directly applicable to a SHS system for two reasons: first, in contrast to APDs the CCDs usually used for an SHS have a non-negligible readout noise which contaminates the assumed photon Poisson noise and leads to a Gaussian noise distribution; second, centroiding is the most computationally intensive task in a SHS system; but it is also the place, where any calculations on the integrated intensity of the individual subapertures could be done; due to computational constraints, it is therefore not possible. Noise determination, especially real- or near-real-time remains a big problem in the application of the PSF reconstruction technique to the SHS and will be discussed extensively in chapter 3.2.
Suppose for the time being that the noise covariance matrix has been found. Still, the aliasing contribution is left to calculate. As mentioned in section 2.2 the covariance matrix of the non-controlled high-order modes, $\left\langle \vec{a}_\perp \vec{a}_\perp^T \right\rangle$ is assumed to follow Kolmogorov statistics and the cross-talk matrix $\mathbf{C}$ is found from sensor modeling. Again, the (original) Fried parameter r_0 of the momentary atmospheric turbulence has to be determined to scale the high-order contribution accordingly. This can be accomplished using a modified form of equation 2.57 (Veran et al., 1997)

$$\left\langle \vec{a}\vec{a}^T \right\rangle \approx \left\langle \vec{m}\vec{m}^T \right\rangle - \mathbf{C} \left\langle \vec{a}_\perp \vec{a}_\perp^T \right\rangle \mathbf{C}^T - \mathbf{R}_{LS} \left\langle \vec{n}\vec{n}^T \right\rangle \mathbf{R}_{LS}^T \int |h_n(f)|^2 df, \tag{2.74}$$

where $\left\langle \vec{m}\vec{m}^T \right\rangle$ is the covariance matrix of the mirror commands interpreted in the modal framework,

$$\phi_s = \sum_{i=1}^{m} m_i(t) F_i(\vec{r}). \tag{2.75}$$

This means that the mirror commands issued have to be recorded in order to apply equation 2.74. Supposing now that a way to establish the noise covariance matrix is found as well, the iterative algorithm for the determination of r_0 is usable again with the only difference of using equation 2.74 instead of 2.57 in step 2, leading to:

Recovering the Parameters:
During observation, three quantities need to be recorded: the measured residual modal covariance matrix $\left\langle \hat{\vec{\epsilon}}\hat{\vec{\epsilon}}^T \right\rangle$, the noise covariance matrix $\left\langle \vec{n}\vec{n}^T \right\rangle$, and the mirror command covariance matrix $\left\langle \vec{m}\vec{m}^T \right\rangle$. From their values, and the assumption of Kolmogorov turbulence together with a suitable sensor model, an estimate of r_0 is found from equation 2.74. Now the actual modal covariance matrix $\left\langle \vec{\epsilon}\vec{\epsilon}^T \right\rangle$ is calculated from equation 2.73.

After this is done, everything needed to reconstruct the PSF is known.

Putting it all together:
The structure function of the residual controlled modes to the system OTF is calculated using equation 2.70, the contribution of high-order modes using equation 2.71 with the theoretical modal covariance matrix scaled by r_0. The structure functions are then entered into equation 2.68, yielding the system OTF. From that the PSF is found by Fourier transformation.

2.3.3 Leaving the Optical Axis - Anisoplanatic Contribution

Unfortunately, the PSF thus reconstructed is only valid for the guide star itself and objects very close by, i.e. objects within the isoplanatic patch (cf. 2.1.2). The differences in the propagation path between the guide star and locations away from it give rise to another source of residual wavefront aberrations that, however, can be captured in yet another contribution to the total OTF (Fusco et al., 2000), the *anisoplanatic transfer function* (ATF)

$$B_{ani}(\vec{\rho},\alpha) = \exp\left[-\frac{1}{2}D_{ani}(\vec{\rho},\alpha)\right], \tag{2.76}$$

where α is the angular distance from the guide star and D_{ani} is the isoplanatic structure function. The computation of the isoplanatic structure function is rather complicated, but assuming that all controlled modes are perfectly corrected on-axis, an expression can be found (Chassat, 1989)

$$D_{ani}(\vec{\rho},\alpha) = \sum_{i=1}^{m}\sum_{j=1}^{\infty} 2\left[C_{ij}(0) - C_{ij}(\alpha)\right] U_{ij}(\rho). \tag{2.77}$$

The C_{ij} are called *angular correlation functions* of the used modal basis set (Chassat, 1989); for circular Zernike polynomials, there even exists an analytical expression. The most general expression, assuming Kolmogorov turbulence, is given by (Chassat, 1992)

$$C_{ij}(\alpha) = \left(\frac{D}{r_0}\right)^{5/3} \frac{\int_0^\infty dh C_n^2(h)\sigma_{ij}(\alpha,h)}{\int_0^\infty dh C_n^2(h)} \tag{2.78}$$

with

$$\sigma_{ij}(\alpha,h) = \frac{0.023}{2^{5/3}} \iint d^2\vec{f} Q_i(\vec{f}) Q_j(-\vec{f}) |\vec{f}|^{-11/3} \exp\left[-\frac{4i\pi h}{D}\vec{f}\vec{\alpha}\right]. \tag{2.79}$$

Here, the Q_i are the normalized Fourier transforms of the modal basis set, D is the pupil diameter and $\vec{\alpha}$ is the displacement vector of the off-axis positon with respect to the guide star.
When another modal basis set than Zernikes is used, the $\sigma_{i,j}$ have to be calculated numerically, fortunately only once. If a $C_n^2(h)$-profile of the atmosphere is available, e.g. using SCIDAR, the ATF can finally be found.

Anisoplanatic contributions:
If the PSF of a star away from the guide star is to be reconstructed, a measurement of the $C_n^2(h)$-profile is necessary; if this is found, the modifications of the on-axis OTF can be found by inserting the profile into equation 2.78 and calculating the ATF using equations 2.77 and 2.76.

2.3.4 Summary and Tasks

Figure 2.17 summarizes schematically the steps necessary to obtain accurate estimates of the on- and off-axis PSF of an AO system. The flow of data from the measurements of the gradients $\vec{g}$,

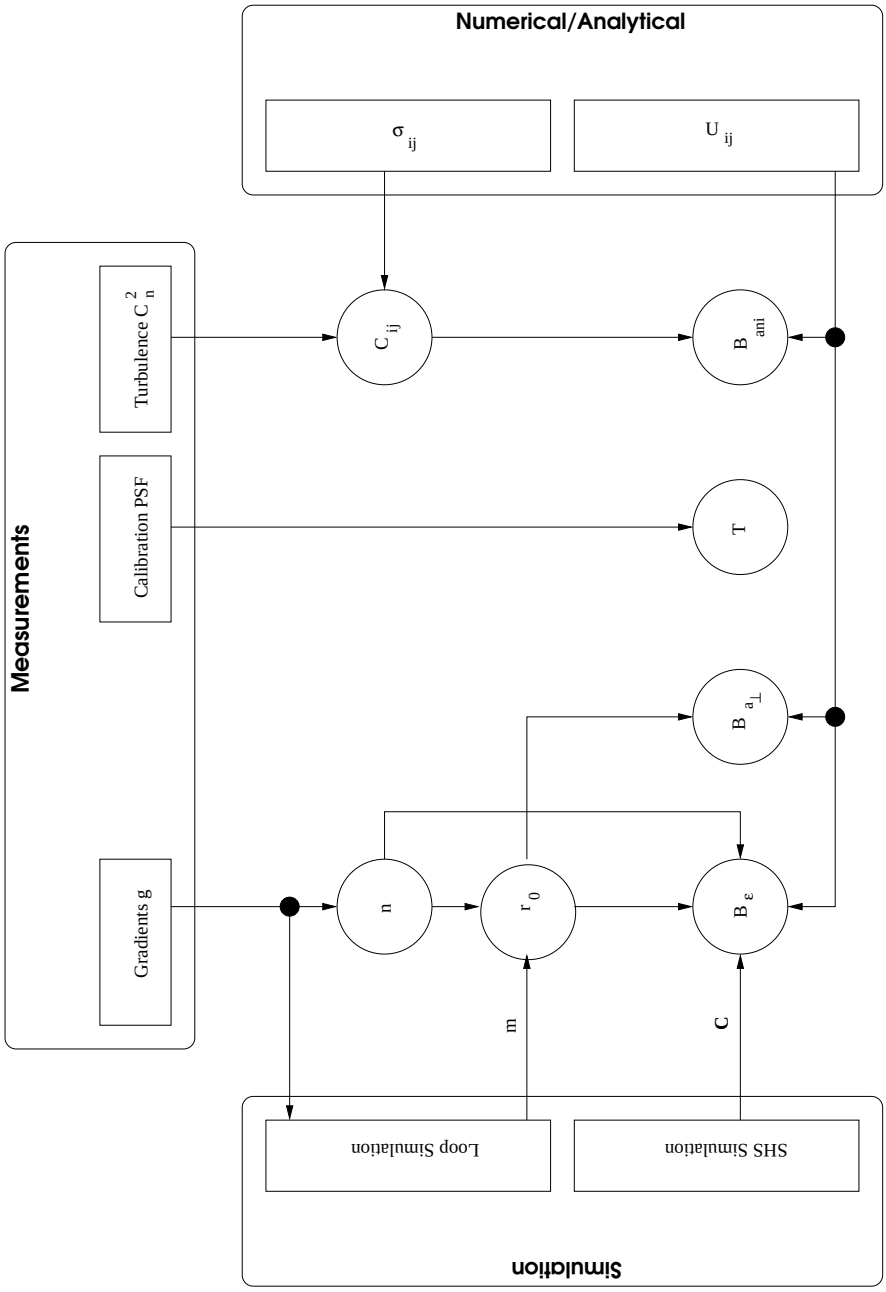

Figure 2.17: Schematics of the on- and off-axis PSF reconstruction process.

the calibration PSF, and the $C_n^2(h)$ profile is depicted. The boxes enclosing the "Simulation" and "Numerical/Analytical" contributions indicate sub-tasks that are more comprehensively described in appendix C. Several tasks that were necessary to be tackled within this work:

- Development of a method to obtain reliable estimates of the noise covariance matrix from closed-loop data; preferably in real-time.
- Implementation of a closed-loop Fried parameter estimation procedure and a test of its reliability.
- Simultaneous measurements with a SCIDAR instrument and ALFA; this served as a further check of reliability of closed-loop atmospheric parameter estimation and a basis for off-axis PSF reconstruction.
- Numerical calculation of the U_{ij} and $\sigma_{i,j}$ for the modal basis sets used with ALFA.
- Implementation of the PSF reconstruction process for the ALFA system.

2.4 Introductory Example Revisited

The tools and prerequisites to reconstruct on- and off-axis PSFs from WFS data were presented in the preceding section. Going back to the introductory example, the methods will now be validated in a controlled, i.e. simulated, environment. Although not all aspects of the reconstruction process are part of the simulation, it still serves both as a limiting case, highlighting the possible performance and achievable accuracy of the method with all quantities perfectly known and a check of the workability of the algorithm.

2.4.1 Simulation Parameters

The diamond-shaped starfield (see top image of figure 2.22) consists of 25 equally bright stars arranged with constant horizontal and vertical offsets of 4". Table 2.5 gives the atmospheric configuration of the simulation along with the total turbulence parameters derived from it.

Layer No.	Height [m]	Fried Parameter r_0 ["]
1	0	0.3
2	2000	0.5
3	10000	0.75

Total r_0	22.3cm
Isoplanatic Angle θ_0	4.5"

Table 2.5: *Layer configuration of the simulation.*

For the simulation, a number of 500 independent realizations of turbulent phasescreens were calculated; correction was performed on the rightmost star of the field. At each step, the aperture phase distribution of this star was decomposed into 237 KL modes. Its first 27 modal coefficients were then multiplied by Gaussian random numbers with zero mean and a arbitrarily chosen standard deviation of 0.1, in order to simulate a non-perfect correction. The degraded coefficients were subsequently used to synthetisize the aperture plane phase corrector (corresponding to the DM) that was then subtracted from the pupil phase of each star before imaging. In contrast to most real systems, where wavefront sensing and imaging are done at different wavelengths, the simulation performed both tasks at the same wavelength of 2.2 μm[1]. As a 3.5m telescope with the same configuration as Calar Alto's was simulated, image plane sampling was set to 0.04"/pixel, to adequately sample the diffraction limited FWHM of the PSF of around 0.13".
Additionally, at each time step the following quantities were saved:

1. The value of the first 27 KL modal coefficients, corresponding to the mirror configuration $\vec{m}$ in equation 2.74.

2. The difference of $\vec{m}$ and the degraded coefficients that were used for the calculation of the phase corrector, corresponding to the low-order mode residuals $\vec{\epsilon}$ in equation 2.73.

3. The image plane intensity distribution of each star.

While the modal coefficient data is sufficient to carry out the on-axis reconstruction, off-axis reconstruction needs the knowledge of the $C_n^2(h)$ profile. For this purpose, a corresponding SCIDAR simulation was carried out with the same atmospheric configuration, but at a wavelength of 500 nm

[1]Since the dispersion of air between the visual band and the near infrared is negligible, this does not make a difference for the results.

and the scintillation simulation option activated (see appendix A). With this additional data, the methods of section 2.3 can be applied; there are, however, some simplifications as compared to a "real" systems, notably the absence of measurement noise and modal aliasing[2].

2.4.2 On-axis PSF

First, the on-axis, i.e. the guide star PSF will be reconstructed. As shown in section 3.3, the quantities needed are the covariance matrix $< \vec{\epsilon}\vec{\epsilon}^T >$ of the residual low-order modal coefficients, the covariance matrix $< \vec{a}_\perp \vec{a}_\perp^T >$ of the non-controlled high order modes, and the OTF $T(\vec{\rho})$ of the unaberrated system.
With the absence of noise and aliasing, $< \vec{\epsilon}\vec{\epsilon}^T >$ is directly given by the covariance of the recorded residual modal coefficients. From this matrix, an estimate of r_0 is found by fitting to the theoretical covariance of KL modes for Kolmogorov turbulence (table 2.4), yielding $r_0 = 23.4 \pm 0.2$ cm, slightly higher than the expected value of 22.3 cm (see table 2.5). The discrepancy is probably due to the fact that while the simulation largely follows Kolmogorov statistics, it has an effective outer scale (see appendix A) that lowers the variance of the first few modes, leading to an overestimation of r_0. Nevertheless, the estimated r_0 is used to scale the high-order covariances for the non-controlled KL modes, giving $< \vec{a}_\perp \vec{a}_\perp^T >$. Finally, $T(\vec{\rho})$ is calculated for an annular aperture with a secondary obstruction of $d_i/D = 0.39$. The total on-axis OTF obtained by combining the results according to equation 2.64, which in turn yields the PSF estimation by a Fourier transform. Figure 2.18 shows a comparison of the "measured" and reconstructed PSF and OTF. As can be seen, the agreement is nearly perfect, with all residuals very low. In fact, the largest errors are visible in the y-cut of the PSF, but this seems to be due to a subtle shift between the image PSF and the reconstruction; the reason for this is probably a small residual tilt on the simulated corrected pupil plane phase (since the decomposition method involves a transformation from Cartesian to polar coordinates, this might be a visible effect of numerical errors in the mapping (Cannon, 1996)).
The near perfection of the on-axis PSF reconstruction is not entirely unexpected: first, the low-order residuals are known *exactly*, i.e. no statistical ambiguities or noise/aliasing estimation errors are present, and, secondly, while there is a small error in the estimation of the high-order contribution, its effect on the PSF/OTF is barely visible. Lastly, the simulated turbulence spectrum is by definition of Kolmogorov type (save the effective outer scale), eradicating this additional potential error source as opposed to measurements in the real atmosphere.

2.4.3 Off-axis PSF

The next step is the reconstruction of an off-axis PSF, the result of which is expected to be much closer to reality. In contrast to the on-axis case, all the variances are now only estimated quantities, i.e. they are not directly measurable.
The $C_n^2(h)$ profile needed for the reconstruction was calculated from the SCIDAR simulation using the SCAVENGER package; the resulting profile is shown in figure 2.19; while it reproduces the simulation parameters quite well, it also shows the smear-out effect of SCIDAR measurements. The total turbulence parameters calculated from this profile are $r_0 = 22.7 \pm 0.04$ cm and $\theta_0 = 4.73 \pm 0.07$" in very good agreement with the expected values.
As in important side-note, it should be mentioned that the isoplanatic angle can also be estimated from the decay of Strehl ratios with increasing distance from the guide star; by combining equations 2.11

[2] Of course, the finite sampling of the aperture plane constitutes a potential source of aliasing; however, for this simulation the sampling was 8 pixels per (total) r_0, high enough for this effect to be negligible.

and 2.14, one gets

$$\theta_0 = \alpha \left[-\ln \left(\frac{S}{S_0} \right)^{-3/5} \right], \tag{2.80}$$

where α is the distance from the guide star, S the Strehl ratio at this distance, and S_0 the on-axis Strehl ratio. For the simulation this estimation method gives $\theta_0 = 9.21 \pm 1.25$". This, however, is no surprise, since equation 2.14 is only valid for *perfect* on-axis correction, i.e. a residual phase rms of 0. Since, in reality as well as simulation, AO correction is only partial, Strehl ratio decay is always much less dramatic[3] than implied by the $C_n^2(h)$ profile. This fact should be kept in mind when comparing $C_n^2(h)$ derived isoplanatic angles to Strehl ratio estimations in section 3.3, effectively stating that the theoretically derived θ_0 places a lower limit on the observed values.

Continuing in the reconstruction process, the turbulence profile is entered into equation 2.78 in order to obtain an estimate of the ATF contribution to the off-axis PSF. Multiplication of this ATF with the on-axis OTF yields the results shown in figure 2.20 for a star 12" away from the guide star (marked by a box in figure 2.22). Although not nearly as perfect as for the on-axis case, the quality of the reconstruction is still very good with residuals lower than 10% of the PSF signal. Indeed, the difference in the radially averaged PSF is much smaller than in the directional cuts, emphasizing the influence

[3] In fact, the actual degradation of the correction with increasing distance to the guide star depends on a lot of factors such as the turbulence profile, the modal basis set used, system performance etc. (Roddier, 1999) and can in principle be found by a thorough examination of equation 2.78. This topic, however, is beyond the scope of this work.

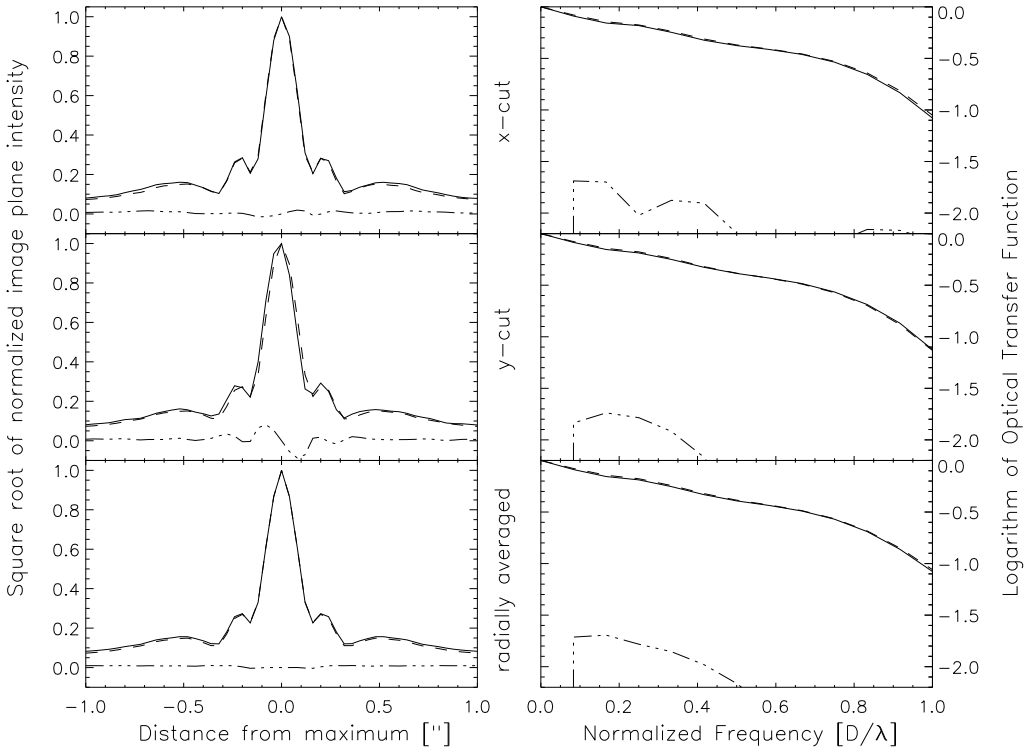

Figure 2.18: *Comparison of measured (solid) and reconstructed (dashed) PSFs. x-cut (top), y-cut (center), and radial average (bottom) of the guide star PSF (left) and OTF (right). The difference between each pair of curves is also shown (dash-dotted).*

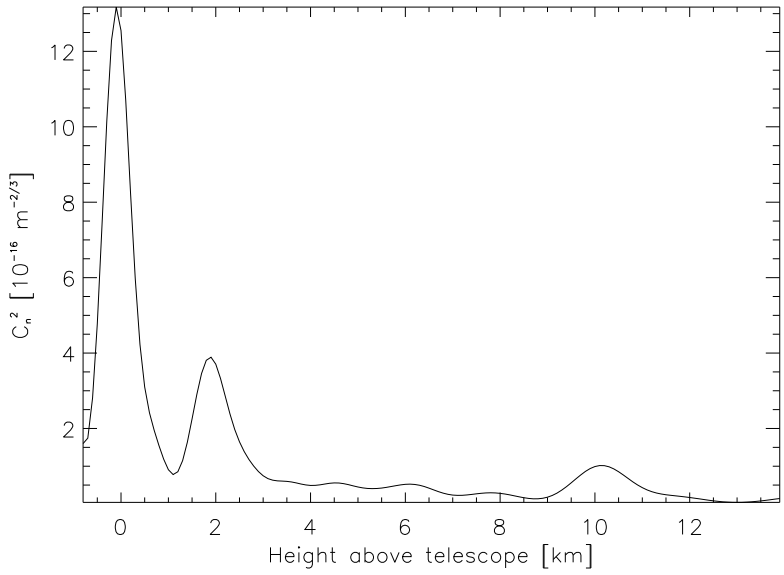

Figure 2.19: *$C_n^2(h)$-profile reconstructed from a simulated SCIDAR measurement with the same parameters as the starfield simulation.*

of the high-frequency "bumps" in the x- and y-direction, which might be due to the limited number of image frames used in the simulation (leading to a relative low SNR in terms of Speckle noise). This high-frequency discrepancy is even better visible in the OTF comparison.
Altogether, the reconstruction results for both the on- and off-axis case are very satisfactory and show the potential of the technique.

2.4.4 Deconvolution and Photometry

Finally, the simulated image is treated the same way as in chapter 1, this time using the locally reconstructed PSFs for the CLEAN deconvolution. To accomplish this, a quadratic grid of reconstructed PSFs was generated, extending 20" in each direction from the guide star with a spacing of 2". Using this, the image was CLEANed using nearest-neighbor PSFs for the reduction, stopping when the first image pixel turned negative. The result of the deconvolution is shown in the bottom image of figure 2.22. In stark contrast to the results of chapter 1, this time the deconvolution successfully retrieves the original stellar pattern (as in figure 1.1, the shaded regions around the stars are a consequence of the finite size of the deconvolution PSFs; black areas are regions where the clean algorithm reduced image intensity to zero).
Performing aperture photometry on the CLEANed image clarifies the tremendous impact of data reduction with a locally reconstructed PSF. Figure 2.21 shows that the flux of the stars relative to the flux of the guide star is now estimated as 0.98 ± 0.04.
The simulation showed that PSF reconstruction works in a controlled environment and promises to decisively increase the accuracy of measurements performed on stellar images. In the section 34, the results of an implementation of the methods at the AO system ALFA will be examined.

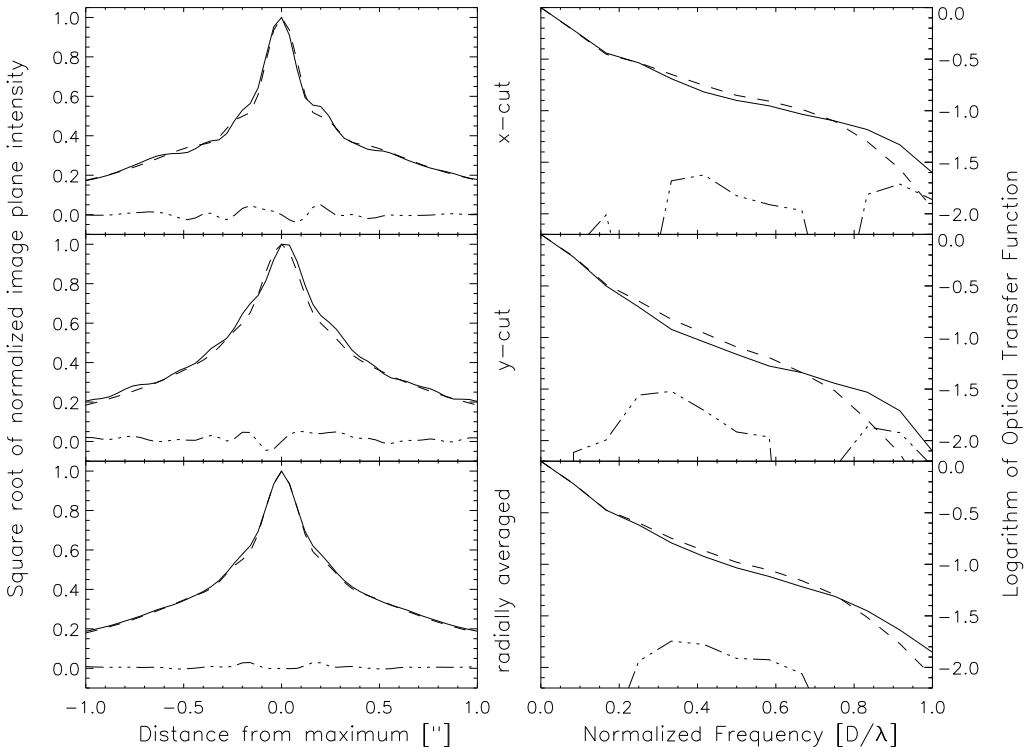

Figure 2.20: *Comparsion of measured and reconstructed PSF and OTF for a star 12" away from the guide star. Same legend as in figure 2.18.*

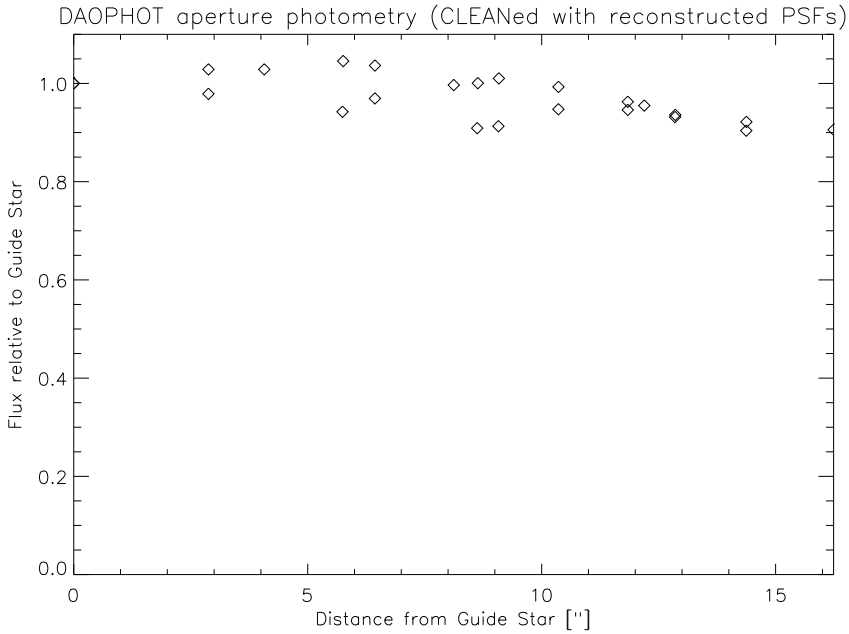

Figure 2.21: *Result of aperture photometry on deconvolved image.*

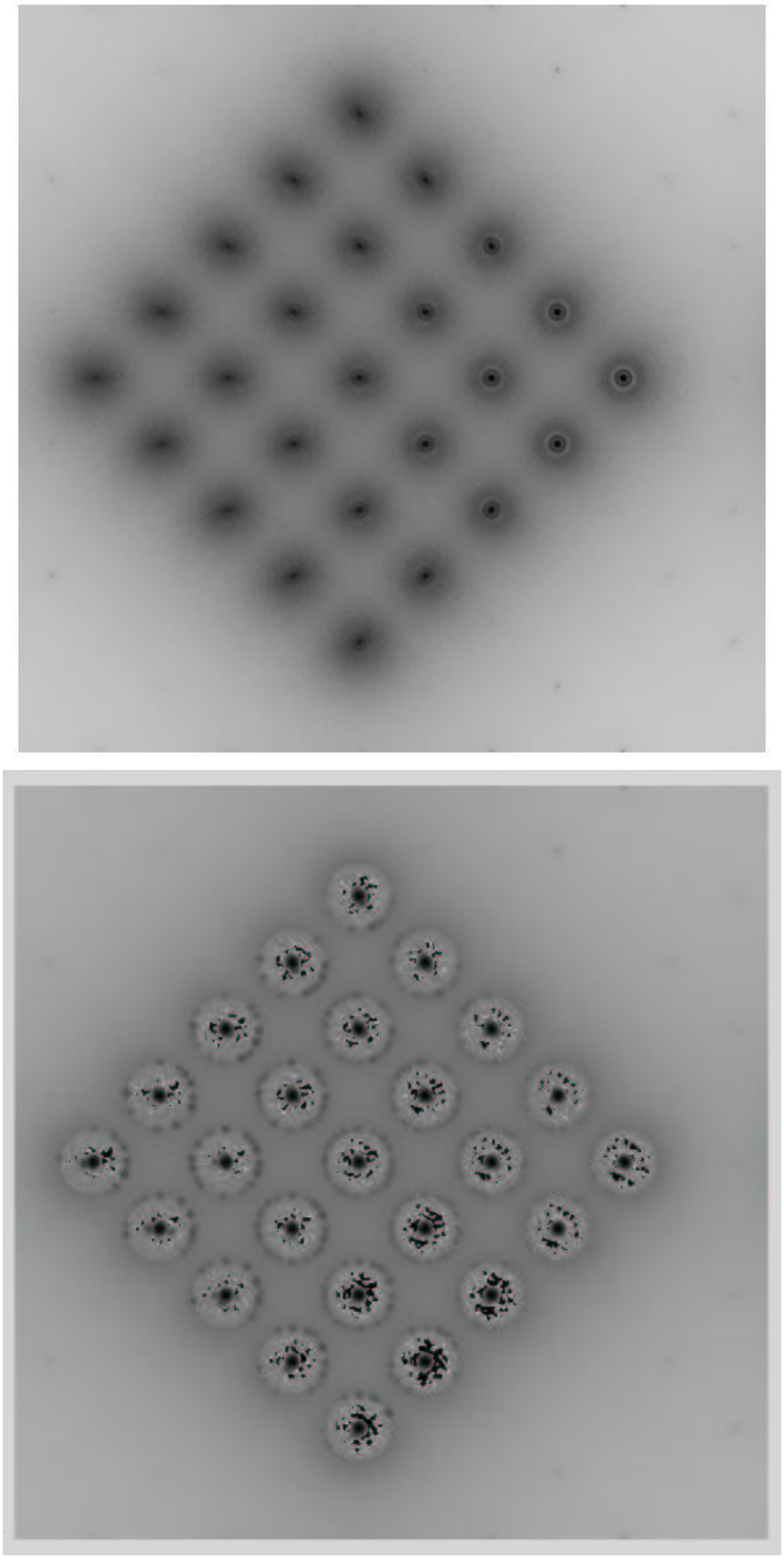

Figure 2.22: *Long-exposure image of a simulated star field corrected by an adaptive optics system, grayscale is inverted for better visibility. Horizontal and vertical distances between stars is 4 arcseconds (top). Same image deconvolved with the locally reconstructed PSF (bottom).*

Chapter 3

Application to ALFA

While the last chapter laid the theoretical groundwork of AO PSF reconstruction, this chapter will discuss its implementation and measurements using the AO system ALFA.
We start with an overview of the technical specifications of the instruments used in the observations. Beginning with ALFA, its optics, sensor type and control system, then having a short look on the infrared science camera Omega Cass, the first section concludes with a description of Imperial College's SCIDAR system.
The application of PSF reconstruction to ALFA first requires a means to estimate sensor and modal noise; while this problem is solved for open loop, problems remain in closed loop. A method to overcome this limitation will be introduced.
Subsequently, turbulence parameters like the Fried parameter, and the isoplanatic angle as obtained from ALFA/Omega measurements are viewed together with atmospheric turbulence profiles measured with SCIDAR, checking the consistency of both approaches as well as to investigate the characteristics of the atmosphere above Calar Alto. This step to obtain $C_n^2(h)$ profiles of the atmosphere simultaneously to AO measurements, is necessary for off-axis PSF reconstruction.
Eventually all insights gained in the preceding section are brought together in order to present the results of on- and off-axis PSF reconstruction for the ALFA AO system, showing the feasibility and accuracy achievable with this system.
Finally, the reconstructed PSFs are used to show that off-axis photometric accuracy can be considerably improved for AO images when using locally estimated imaging properties.

3.1 System Description

3.1.1 ALFA

ALFA is a pupil-conjugated Shack-Hartmann type AO system, described in great detail in Kasper et al. (2000a) and Glindemann et al. (1997). It is in use since 1996, with its performance having since improved by careful optimization of its wave-front sensing (Kasper, 2000) and control-system (Looze et al., 1999).

Optics

Fig.3.1 shows the main optical elements of ALFA. The two main features are a conversion of the default f/10 focus of the telescope to a f/24 focus by off-axis paraboloids, and re-imaging of the beam at the original Cassegrain focus position. The beam from the telescope is reflected by a flat mirror

that also serves for tip-tilt correction; after that, a f/10 paraboloid mirror re-images the telescope pupil on the DM, where wave-front correction takes place. The collimated beam is then reflected by a f/24 paraboloid mirror onto an IR/Visible dichroic mirror that directs infrared light back to the original focus position and is mostly transparent to visible light which is used for wavefront aberration measurements. One big advantage of this design is that no part of the wavefront sensor optics lies within the science lightpath, enabling ALFA to be used in pure active optics mode for very faint targets or observations that do not require AO correction. Additionally, it is possible to remove both the tip-tilt mirror and the beamsplitter from the lightpath, which means that the ALFA instrument can stay mounted on the telescope without interfering with other science instruments, which can be attached to the ALFA science camera mounting.

A CAD rendering of the ALFA breadboard is available in Fig.3.2. In addition to the already described components, the SHS, the tip-tilt sensor, the TV guider, the f/10 reference fiber, and an interferometer are visible.

The reference fiber is capable of transmitting point-source like (with a diameter of about 6μm) light from either a white light source (used for calibration and alignment) or a HeNe laser (used for alignment), and can be remotely moved into or out of the lightpath. The interferometer serves as a monitor when flattening the DM or checking the correctness of modal shapes when applied to the mirror.

A TV guider can also be entered into the beam and is mostly used for target acquisition. With its FOV of 4 arcminutes (as opposed to the 40 seconds of arc when e.g. using Omega Cass), it allows to find desired targets even if coordinates are insufficiently known or the telescope is mispointing strongly.

The SHS will be discussed in the next paragraph; the separate tip-tilt sensor, however, was originally necessary for LGS operation with ALFA as well as reducing demands on the DM (see below). Since it is not possible to infer tip-tilt aberrations from LGS observations, an additional NGS is needed to retrieve this information. With the help of a field select mirror, that diverts light into the tip-tilt sensor, ALFA is capable of using a different star for tip-tilt than for high-order sensing. Unfortunately, the laser subsystem of ALFA is no longer available, therefore this capability has been removed in 2003 as well. However, since the tip-tilt aberrations are the modes with the highest variance in atmospheric turbulence, the separation from the high-order correction system considerably reduces the necessary stroke of the DM actuators, allowing the use of a DM with a small dynamical range.

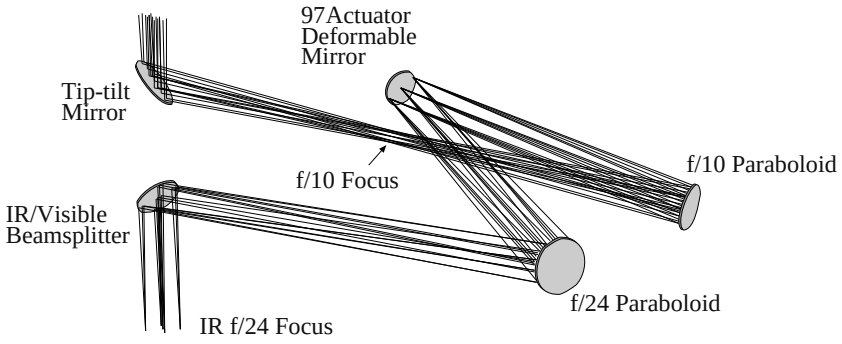

Figure 3.1: *Optical elements of the ALFA system.*

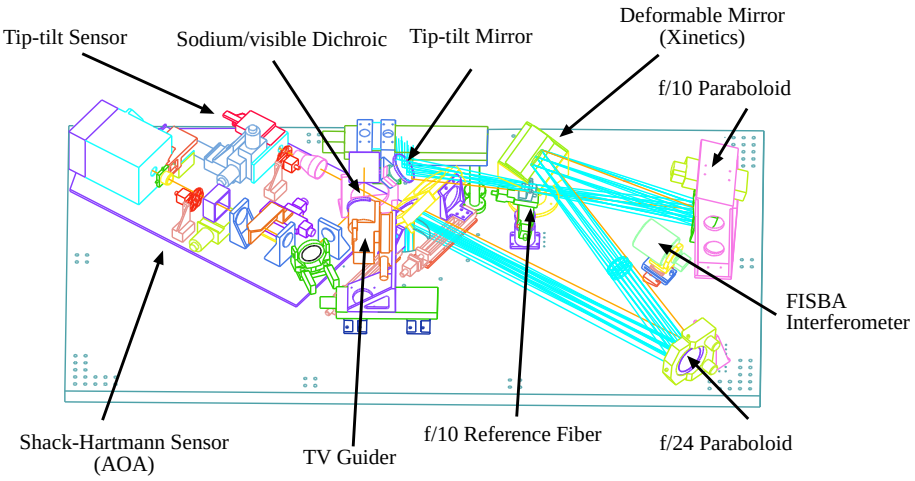

Figure 3.2: *CAD rendering of the ALFA breadboard.*

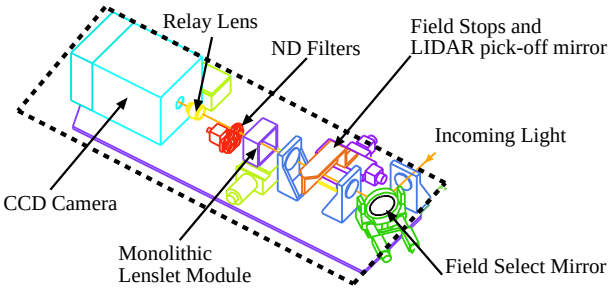

Figure 3.3: *The elements of the ALFA SHS sensor.*

Shack-Hartmann Sensor

Fig. 3.3 shows the components of the ALFA SHS, which was built by Adaptive Optics Associates, Cambridge, USA. By means of the field select mirror, a guide star up to 30” away from the telescope optical axis can be selected as a corrective beacon; this is useful for the observation of very extended astronomical objects as well as for mosaicing of NIR images.

The next element in the light path are the field stops, used to limit the SHS field of view. This is necessary if an extended light source is used as a guide star or to select one star within a dense cluster.

The monolithic microlens module is located at an image of the telescope’s pupil plane. The module consists of a motorized stage, with which the lenslet array, to be used for the wavefront analysis, can be selected. Originally, the ALFA system used hexagonal microlens arrays, of which now only that with the highest number of subapertures is still employed; the other two have been discarded in favor of a much superior setup, the *keystone* design (Kasper and Hippler, 2003). Figure 3.4 shows the microlens arrays currently in use at ALFA; the 7×7 hexagonal array, mainly used for very bright stars, the Keystone 28 (KS28) and the Keystone 7 (KS7) array; the three lenslets are depicted in figure 3.4. The big advantage of the KS compared to the hexagonal design lies in the KS perfect adaption to the annular shape of the telescope pupil; hence, all lenslets are equally illuminated, leading to similar noise behavior on each of the gradients obtained with the KS7 and KS28. The selection of the array

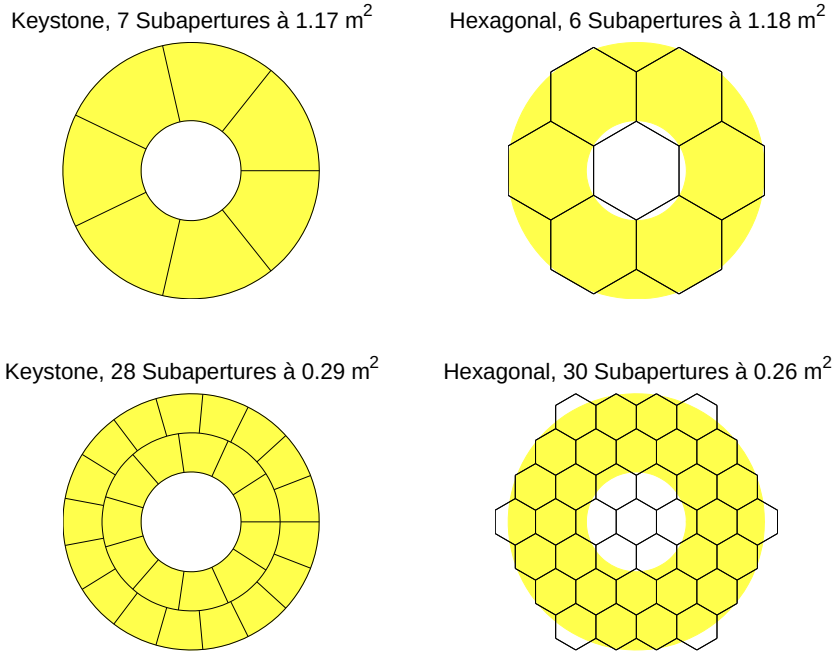

Figure 3.4: *Microlens configurations. Hexagonal* 3×3 *(top right) and* 7×7 *(bottom right), keystone 7 (top left), and keystone 28 array (bottom left). The shaded regions depict the illuminated annulus of the Calar Alto 3.5m telescope.*

suited for a measurement depends mainly on two factors: the Fried parameter and the brightness of the guide star. While, ideally, the size of the lenslets should be on the order of r_0, a certain level of illumination is needed, which sometimes dictates the use of the KS7, thus degrading correction performance. In this work, all measurements were exclusively done with the keystone design, the KS28 in the bright star case and the KS7 for faint ones.

The neutral density filters are used to darken a very bright guide star, that might impair measurements by saturation of the CCD pixels or bright reflections showing up on the SHS camera. Imaging of the spot pattern resulting from the lenslet array is done by the relay lens.

The SHS CCD camera uses a 64×64 pixel Lincoln Labs CCD (LLCCD) with a maximum framerate of 1206 Hz. Its read-out noise is about 4 electrons. As can be seen from figure 3.5, its quantum efficiency is highest between 600 and 700 nm, where it exceeds 80% . For this reason, a center wavelength of 650 nm is assumed in the calculation of the subsequent sections (this influences scaling of r_0 estimates and modal variances to the science camera observing wavelength). Also shown in figure 3.5 is the quantum efficiency of the CCD (EEV39) used in the separate tip-tilt system. As can be seen, its maximum sensitivity region lies between 500 and 600 nm, suggesting to use 550 nm as the tip-tilt measurement wavelength for scaling purposes; note that, since tip-tilt values are *not* used for Fried parameter estimation[1], the difference has no consequences on the estimation algorithm for r_0 (see section 2.3). For PSF reconstruction, however, it has to be taken into account by scaling tip-tilt variances differently than variances of the higher modes.

[1]Due to the outer scale, tip-tilt variances do not follow Kolmogorov statistics (see also chapter 2.2)

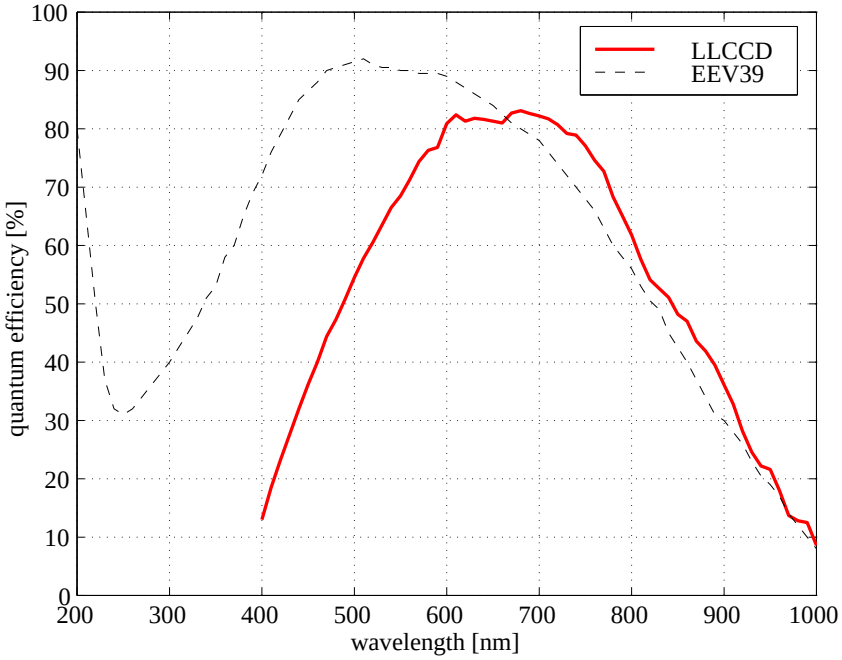

Figure 3.5: *Quantum efficiency of the SHS CCD and the tip-tilt CCD.*

Deformable Mirror

ALFA's DM is a 97 ceramic piezo actuator continuous-sheet mirror manufactured by Xinetic Inc., USA. It is capable of delivering an inter-actuator stroke of up to 2 μm with each actuator reaches its commanded position within 0.2 ms. As the piezos are arranged on an 11×11 grid, the telescope pupil is sufficiently sampled to accurately reproduce polynomials up to the 6th radial order, which includes the first 28 Zernikes and Karhunen-Loeve functions (Kasper, 2000). It has been found that the interaction between two neighboring actuators is below 10% (Wirth et al., 1998).

The linear operation range of the piezos lies between -35 and -105 Volts. If the same voltage is applied to all actuators, the rms aberration of the reflected wave is about 600nm. Since this would considerably reduce the performance of the system, an interferometer is used to flatten the DM during the calibration process; this procedure is fully automated and regularly delivers a mirror flatness of around 60nm rms (about $\lambda/10$ rms of the measurement wavelength).

Another potential performance hazard is piezo hysteresis, which has also been found to be very small (Kasper, 2000). The DM is, however, sensitive to temperature changes, occasionally requiring a re-flattening if the temperature changes substantially during an observation night.

The PSF reconstruction process needs an accurate knowledge of the modal set dependent quantities U_{ij} and σ_{ij} introduced in section 3.3. These coefficients are quite sensitive to deviations of the actual mirror shape from the theoretical values of the modes. To assess the quality of the representation of KL modes by the DM, interferometric images of the mirror surface were taken. Figure 3.6 shows a comparison of the mirror shape to the calculated modal shape for two exemplary modes. To account for deviations of the DM from flatness, two measurements at different modal strengths were taken for each mode and subsequently subtracted. As can be seen from the figure, the DM represents the

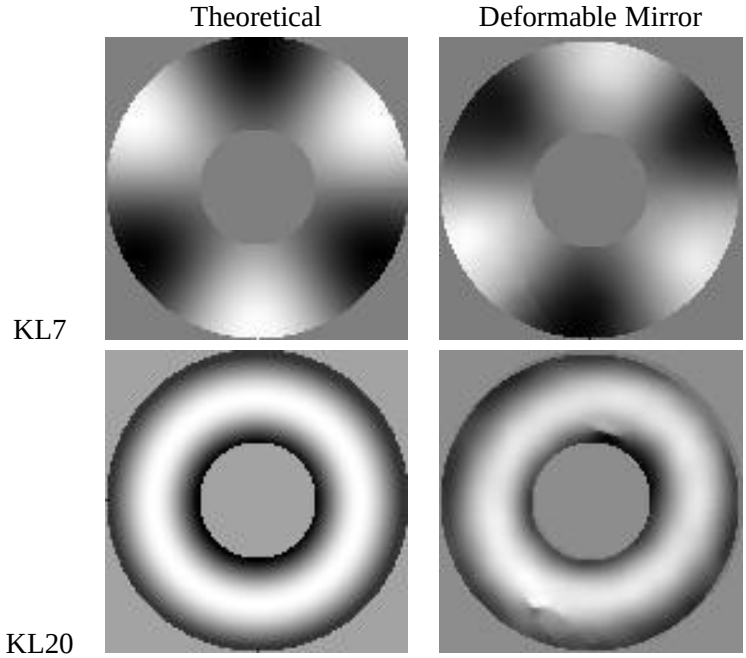

Figure 3.6: *Comparison of calculated (left column) and measured (right column) shape of the KL functions of order 7 (top) and 20 (bottom). The DM images are not de-rotated in order to highlight the difference between the KL7 mode realizations. Bumps on the KL20 DM mode are caused by non-linear responses of single actuators.*

KL modes very well[2]. In fact, if the images are de-rotated and subtracted, one finds an average rms of about 60-170 nm for the first 30 KL modes, corresponding to a phase rms of an order of 0.03-0.08 for K-band imaging, small compared to the usual residual modal aberrations after correction. Nevertheless, the U_{ij} and σ_{ij} coefficients used in sections 3.4 and 3.5 were calculated numerically from the DM measurements rather than using their theoretical values.

Control System

Some of the properties of the ALFA control system have already been introduced in section 2.2 (cf. figure 2.15). It is implemented on a VME-Bus based real-time computer system running VxWorks. The necessary matrix operations, such as centroiding, modal reconstruction and control are done on five interconnected digital signal processor (DSP) boards, containing four DSP chips each. The calculations are distributed between those processors to speed up computation. Additionally, each board has a RAM capacity of up to 8 MBytes, where intermediate information can be stored for later processing; the most important data storable are the gradients, since they contain all the information necessary to carry out the PSF reconstruction process (see also section 3.4). For a typical ALFA setup, i.e. 27 modes corrected using measurements with the KS28 array at 300 Hz, about 80 seconds worth of gradients can be recorded. Unfortunately, the loop has then to be stopped to retrieve the data; since all I/O ports of the gradient processing board are already taken, relaying gradient data to another place in the system is also not easily possible and would require a redesign of the modal control system.

[2]The rotation between the theoretical and measured modes is constant at 54 degrees; it is a consequence of the orientation of the interferometer relative to the DM and has no influence on the accuracy of the modal representation.

In any future upgrade of ALFA, this problem should be addressed to allow for longer uninterrupted observations while retaining the PSF reconstruction ability.
The implementation is capable of projecting up to 50 wavefront control modes within 833 μs, thus allowing a maximum loop frequency of 1206 Hz. This, however, is hardly used since a very bright guide star would be required to achieve acceptable SNR on the SHS for this short an integration time. Up to and including 300 Hz, the control algorithm is that of a PI controller, beyond this frequency, a LQG or optimized control algorithm is used instead (Looze et al., 1999).
The VME/VxWorks system is connected to workstations running the graphical user interface (GUI) via ethernet; this GUI is also used to control the motorized stages on the ALFA breadboard, which in turn receive their commands from the VME system via an RS-232 link. A complete presentation of the ALFA computer system can be found in Hippler et al. (1998).

Calibration and Setup

Before each observing run, a calibration of the ALFA system has to be carried out. Its main goal is to establish the relation between the DM control modes and the SHS. In principle, analytically derived relationships could also be used, but these would be very sensitive to deviations from the nominal alignment of DM and SHS, as well as the difference between theoretical KL shape and actual DM shape[3]. The calibration and setup process consists of the following steps:

1. **Reference:** First, the reference positions of the sublenslet spots on the SHS have to be defined. For this purpose, after flattening the DM, the white light reference fiber is positioned at the f/10 focus and imaged by the SHS as well as the science camera. The latter image is then used to eradicate static aberrations occurring in the non-common path after the IR/visible dichroic by applying fractions of correction modes until the Strehl ratio of the fiber image is satisfying (usually a Strehl ratio of $\sim$90% is desired). If this aim is reached, the positions of the spots on the SHS CCD are saved as reference positions.

2. **Identification of Control Modes:** Now, all of the chosen control modes are applied to the DM sequentially with a unit modal coefficient ($a_i = 1.0$) and the corresponding gradient vectors $\vec{g}_i$ calculated. Arranging these vectors in columns gives the interaction matrix $\mathbf{D}$. With the assumption of a linear relationship between DM shapes and SHS measurements, the modal decomposition of an arbitrary combination of the control modes is then given by

$$\vec{g} = \mathbf{D}\vec{a}, \tag{3.1}$$

   where $\vec{a}$ is the vector of modal coefficients. This equation corresponds to equation 2.46 in section 2.2, so that all results derived there are valid in the context of ALFA.

3. **Reconstruction:** With $\mathbf{D}$ known, the next step is the calculation of a linear reconstructor such that

$$\hat{\vec{a}} = \mathbf{R}\vec{g}. \tag{3.2}$$

   This subject was already discussed at some length in section 2.2. Although tests with a MAP estimator have been successfully performed at the ALFA system (Kasper, 2000), usually the LS estimator

$$\mathbf{R} = \left(\mathbf{D}^T\mathbf{D}\right)^{-1}\mathbf{D}^T \tag{3.3}$$

[3]Depending on how unevenness is distributed on the “flat” mirror, these differences vary from calibration to calibration.

Figure 3.7: *ALFA and Omega Cass mounted at the Cassegrain Focus of the Calar Alto 3.5 m telescope.*

is used. In this case, cross-talk limits the number of correctable modes to about 30 for the KS28 and the 7×7 hexagonal array.

4. **Compensation:** The last step is choosing the control parameters used in closed-loop operation; this mainly concerns the type of centroiding algorithm, the loop frequency, and gain.

After this procedure, the system is ready for observation. A number of quantities is saved during the calibration process which are important for the PSF reconstruction, most notably the interaction matrix $\mathbf{D}$ and the fiber PSF, from which the $T(\vec{\rho})$ part of the system OTF can be calculated.

3.1.2 Omega Cass

All star images presented in this work were taken using the Omega Cass near infrared (NIR) camera (Lenzen et al., 1998). It covers a wavelength range of 1-2.5 μm with a 1024×1024 Rockwell HAWAII array. At the telescope the camera is directly mounted beneath the ALFA breadboard (the cylindrical tube in figure 3.7). The Omega Cass camera has been specifically designed to be used together with the ALFA AO system. Apart from direct imaging, it offers the following observational modes:

- *Polarimetry* using either wire grids or Wollaston prisms,
- *Long-Slit Spectroscopy* with different slit sizes and grisms of spectral resolutions from 500-1000,
- and *Coronography* with exchangeable masks.

All of these observing modes can be controlled and changed remotely, as can a number of broadband (J,H,K,K') and narrow-band filters (e.g. Brγ, FeII(1.644) etc.).

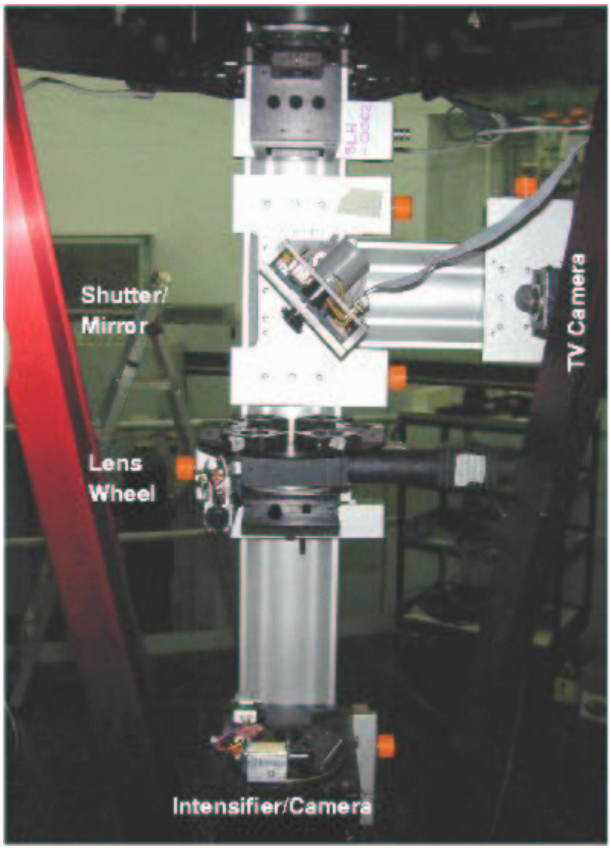

Figure 3.8: *The Imperial College SCIDAR instrument mounted at the Calar Alto 1.23 m telescope.*

When operated with ALFA, exchangeable f/25 optics are used, delivering an image plane pixel resolution of 120, 80, and 40 mas. From August 2000 to early 2002, however, mechanical problems of the optics wheel made it impossible to change the image plane resolution of the camera, which was for this period of time fixed at 80 mas. This resolution only just samples the diffraction limited FWHM of the system in K-band and had to be used for all measurements presented in this work. As will be seen in section 3.4 this limitation considerably complicates the direct comparison of reconstructed to measured PSFs, since the exact location of the PSF peak with respect to the imaging grid is unknown for each image.

3.1.3 Imperial College SCIDAR System

The SCIDAR instrument used for turbulence measurements was supplied and operated by Imperial College's Applied Optics group at the Calar Alto 1.23 m telescope. Figure 3.8 shows the instrument attached at the Cassegrain focus. The working principle of SCIDAR was already discussed in section 2.1. Its actual setup is remarkably simple; as indicated in the figure it consists of a shutter/mirror combination that redirects the focus to a TV camera used for positioning, a lens wheel which sets the conjugate "depth" of the observation plane, and an intensifier/CCD camera combination used for the measurements. Not shown in the image is an accompanying electronics rack.

The simplicity of the instrument makes it very transportable and it has been used at various telescopes

around the world; but this advantage is also one of its biggest drawbacks: on-site calibration is a very lengthy process, which in the case of our measurements required several hours at daytime and nearly a full observing night. As soon as this calibration is done, observations can be carried out without much realignment. The usual goal is to sample the aperture plane of the telescope at around 0.01 m per pixel, a size that is adapted to the typical size of scintillation speckles on the pupil.
In its default mode, the image of the pupil plane is sampled at a frequency of 383 Hz with exposure times of just about 1 ms; the short exposure times are necessary, since the relaxation time of scintillation patterns is not much longer than a few milliseconds (casting doubt on the Taylor frozen flow hypothesis (Saint-Jacques and Baldwin, 2000)).
Due to the high sampling frequency, the system produces a tremendous amount of data which cannot be processed in real-time; rather, the pupil plane images are relayed to a workstation and written on a DAT tape for later processing. Hence, as each SCIDAR profile is derived from a 2048 image block covering approximately 5 seconds, and breaks between individual shots about the same duration, several tens of gigabytes have to be stored during a typical observation night.

3.2 Noise estimation in open- and closed-loop operation

While the determination of most of the covariance matrices needed for PSF reconstruction from WFS data is sufficiently straightforward, the retrieval of the noise covariance matrix $< \vec{n}\vec{n}^T >$ is the most demanding task in applying the PUEO (Veran et al., 1997) method to SHS type systems. In the case of curvature systems, the noise can be directly derived from the intensity measurements in the subapertures. While this in principle is also possible in a SHS setup, it is much harder or outright impossible to implement; unfortunately, intensities are measured at the most busy part of the control system: the centroiding section, where any additional tasks (like noise determination) would increase the already demanding constraints on computational load at this stage. Therefore, it is desirable to find indirect methods of noise estimation; as will be seen, this is rather unproblematic for open-loop measurements, but signal modifications introduced by the closed-loop system pose a restriction on the use of this method.

3.2.1 Open-loop noise estimation

Open-loop noise estimation can be done in several ways if the gradient signal of each subaperture is recorded. The noise level is then derivable by

1. identification of unlikely gradient configurations assuming a specific turbulence model (Gendron and Lena, 1994), which, however, delivers only a global noise estimate averaged over the whole telescope pupil,

2. a fit to the noise floor in the PSD of an individual gradient signal (Harder and Chelli, 2000),

3. an analysis of the auto-covariance of a gradient signal (Gendron and Lena, 1995).

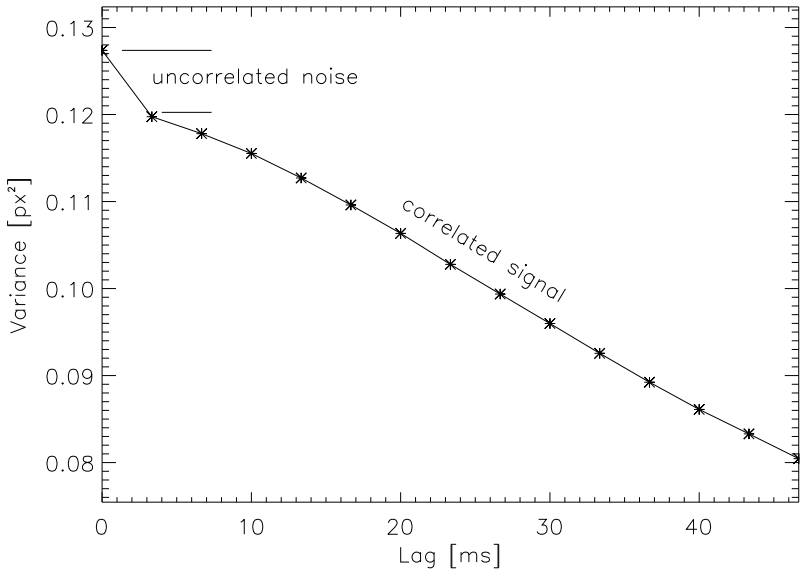

Figure 3.9: *Auto-covariance of a gradients signal; noise and signal contributions are indicated.*

Since different subapertures have different noise levels, method 1 is unsuitable for PSF reconstruction; method 2 is able to find these differences, but operates in Fourier space, making a real-time implementation impossible, since data would for a duration of time have only to be collected (low computational load) but then Fourier-transformed and fitted almost instantaneously (high computational load). Additionally, using the PSD is affected by the problems of calculating Fourier transforms on finite duration signals. This leaves method 3, which delivers subaperture noise as well and can be implemented in real-time (see below).

Principle and results

Method 3 rests on the assumption that the signal can be interpreted as a superposition of two components: a slowly decorrelating atmospheric signal, caused by the current modal configuration of turbulence in the pupil plane, and uncorrelated noise, a combination of photon noise, sky background noise and readout noise; the central limit theorem makes Gaussian noise a sensible approximation to the type of noise involved. Now, since the auto-covariance function of white noise consists of a Dirac peak at a time lag of zero, and the atmospheric signal decorrelates smoothly, the signal auto-covariance looks as depicted in Figure 3.9. Gendron and Lena (1995) showed that the atmospheric signal close to

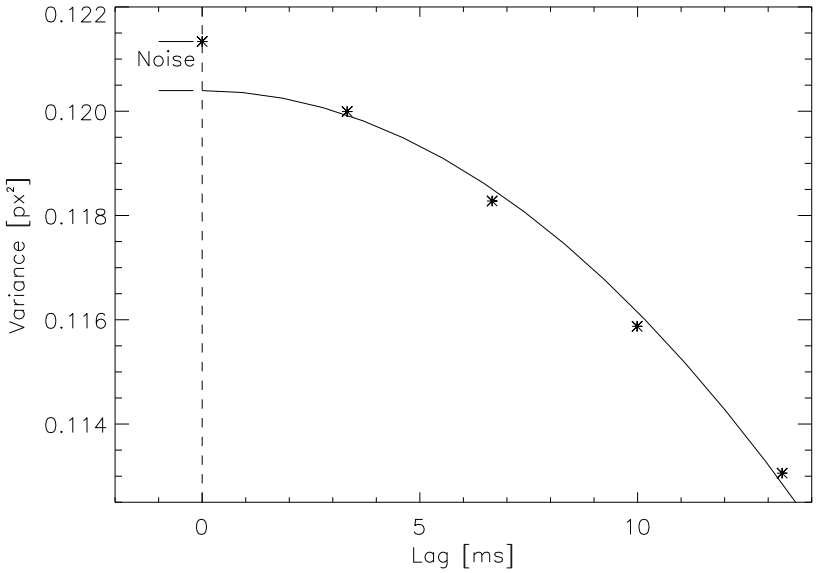

Figure 3.10: *Parabola fitted to the first 4 lagged points of a gradient auto-covariance function; noise value is indicated.*

the origin of the auto-covariance decays with $|t|^2$; since the maximum of this auto-covariance is also at time lag zero, linear contributions can be ruled out and it is sufficient to fit a function of the form

$$g(t) = a + bt^2 \tag{3.4}$$

to the first few points of the auto-covariance, where t denotes the time lag. If $A_i(t)$ denotes the auto-covariance function of the ith gradient, its estimated noise variance is then simply given by

$$\hat{\sigma}_i^2 = A_i(0) - a. \tag{3.5}$$

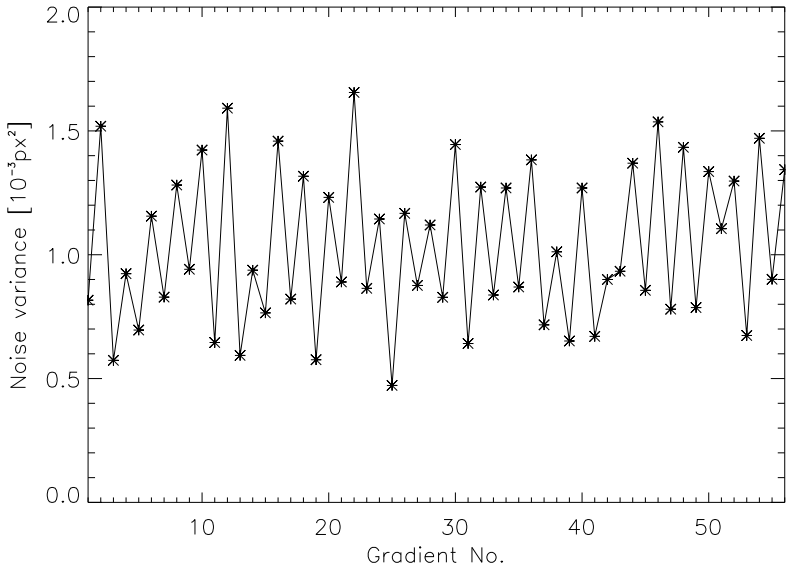

Figure 3.11: *Estimated noise on the subapertures of the KS28 array of ALFA.*

Additionally, the noise at different subapertures can also be regarded as uncorrelated, so that

$$< \vec{n}\vec{n}^T >= \mathrm{diag}(\sigma_i^2) \tag{3.6}$$

is the desired estimate of the noise covariance matrix. Figure 3.10 shows the algorithm in action; as is clearly visible, a relatively good fit is obtained with only 4 points used; in fact, fitting to more than 5 or 6 points is dangerous, as can be seen in Figure 3.9, where the auto-covariance function curves away from the parabola shape quite soon, starting at a time lag of about 20 ms.
Applying the method described above to a set of ALFA gradient measurements recorded using the KS28 array and a sampling frequency of 300 Hz yields the results shown in Figure 3.11; the gradients noise is plotted for the x- and y-directions alternatingly. Other than the systematic differences between horizontal and vertical noise variance, the actual magnitude of noise is not very different between subapertures, which is a consequence of the uniform illumination exploited by the keystone design. There are two possible explanations for the systematically higher noise in x-Gradients: either a coma aberration within the sensor optics (invisible for the correction since it would also be present during calibration) and/or CCD charge transfer inefficiency, caused by a smearing of charge by the fast read-out register in the x-direction (Kasper, 2000).

Checking the algorithm's consistency

In order to check the accuracy and the consistency of the noise estimation, the following test was carried out: recorded gradient measurements were cut into two pieces of equal length and the noise estimated independently on both parts. In total, 14 (open-loop) measurements, consisting of 18000 samples per gradient each, were used for the calculation; the data was collected using the KS28 array again, but different illumination levels were used. Figure 3.12 shows the results. Each point represents a pair of noise estimations obtained from the first and second part of a gradient time series, plotted against each other; the straight line indicates the location of noise ratios of one. The plot

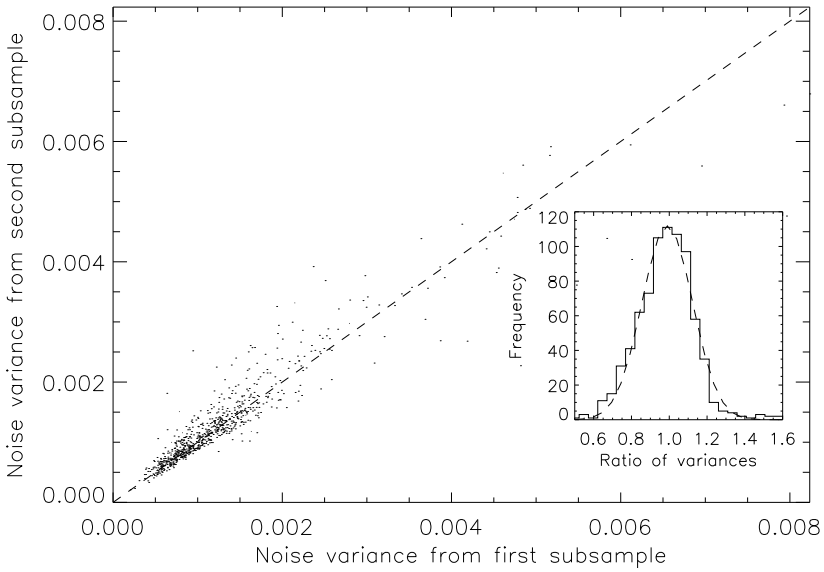

Figure 3.12: *Comparison of noise variance estimations from subsamples; the dashed line indicates a ratio of 1. The histogram of observed ratios together with a fitted Gaussian is depicted in the inset.*

only seemingly implies higher estimation inaccuracy at higher noise levels, since the higher base value exaggerates the distance from the centerline; actual estimation accuracy is estimated from the histogram of noise estimation ratios obtained. The subplot in Figure 3.12 shows this histogram with a fitted Gaussian, which implies a one σ distribution of around 0.08, meaning that on average estimates are consistent within 8 percent.

Real time implementation

As already mentioned in chapter 3.1, the setup of the ALFA control system limits the number of recordable gradients. After this limit is reached, the loop has to be stopped and the data downloaded. This of course makes continuous measurements impossible and leads to considerable delays when adjusting the loop to atmospheric conditions. Therefore it would be highly desirable to either reduce the amount of data to be recorded or, if online adjustments are necessary, even perform online data analysis with the lowest computational load possible. The noise estimation process is parted into two tasks, one to be carried out at each timestep, the other after a given number of samples is acquired. The auto-covariance at lag L of a discrete time series of length N is given by

$$A(L) = \frac{1}{N}\sum_{i=L}^{N}(x_i - \bar{x})(x_{i-L} - \bar{x}), \tag{3.7}$$

where the x_i are the measured values at time step i and $\bar{x}$ is the mean of the series. Theoretically, the mean of a gradient is zero, but tracking errors or a drift in the tip-tilt system often introduce a slight bias, so it is wise not to drop it for the calculation. Expanding equation 3.7 gives

$$A(L) \approx \frac{1}{N}\sum_{i=L}^{N} x_i x_{i-L} - \frac{1-2N}{N^3}\left(\sum_{i=L}^{N} x_i\right)^2, \tag{3.8}$$

where the approximation was done in neglecting the influence of "cutting" of the series at L on the mean value. With this formulation the algorithm is clear:

1. Decide on a number N of time steps used for an individual noise estimation and a number L_{max} of lags used for it (as seen above, 4 are usually sufficient).
2. For each gradient, initialize memory to store $\sum x_i^2$, $\sum x_i x_{i-L}$ for each L, and registers to store the past L values of the gradient
3. Repeat until N timesteps are reached: Update the sums and the past values
4. For each L, calculate the auto-covariance according to Equation 3.8 using the sums and N, store the results, clear memory and start over at step 2.

If e.g. a maximum lag of 4 and a sample size of 6000 are selected, the memory required for information storage is reduced by a factor of 1200. Note that the stored value for $L = 0$ is the variance of the measured gradients, hence all data needed for the calculation of r_0 according to equation 2.57 is delivered by this algorithm. Unfortunately, this algorithm cannot be implemented into the ALFA system, since it is impossible to access gradient measurements at other places than the centroiding control board; calculating in the control board, on the other hand, is prohibited by computational demands. This limitation will be addressed in future updates of the system.

3.2.2 Closed-loop noise estimation

The noise estimation used in the preceeding section rested on the assumption that noise in subsequent measurements is uncorrelated. While true in open-loop, this requirement is not met in closed-loop; noise is considered part of the measurement by the control system and has therefore consequences on the shape of the DM. This feedback subsequently causes temporal correlations in the noise of a subaperture.

To illustrate this behavior, a pure noise signal was fed into a simulation of the ALFA control system (see Appendix C); the response for loop delays of one and two timesteps is shown in Figure 3.13. It is clearly visible that the assumption of uncorrelated noise does not hold anymore. This makes the application of the parabola method for noise estimation dangerous, especially since the near-origin proportionality of the auto-covariance function to $|t|^2$ is not necessarily true in closed-loop. Kasper (2000) proposed to use only the difference of the first two values of the auto-covariance, $\hat{\sigma}_i \approx A(0) - A(1)$ as an estimate of noise. While that prevents the potential misfitting of a parabola, it introduces a systematic error depending on the behavior of the underlying signal, and the autocorrelation function

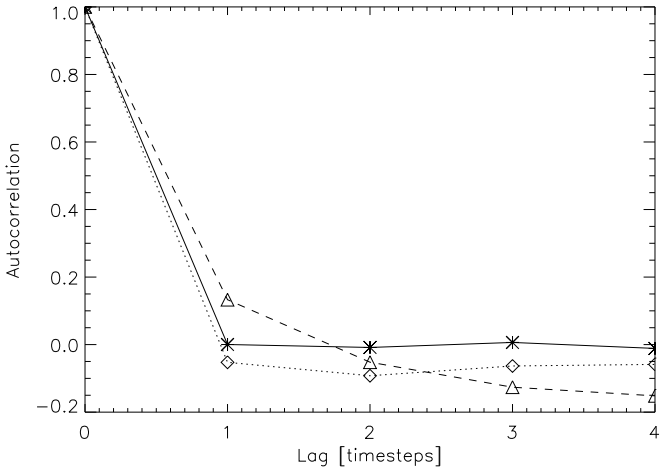

Figure 3.13: *Effect of closed-loop control on noise correlation. Input signal (asterisk and solid line), output signals for loop delay of 1 (triangles and dashed line) and 2 (diamonds and dotted line).*

of the measurement noise. A small modification of this approach (subsequently called the *direct difference method*), however, can considerably improve the accuracy of closed-loop gradient noise estimations. This modification looks as follows

$$\hat{\sigma}_i \approx [A(0) - A(1)] \frac{A(d_{loop} - 1) + A(d_{loop})}{2A(d_{loop} - 1)}, \tag{3.9}$$

where t_{loop} is the loop delay in cycles[4]. This approximation was found during an ARMA analysis (Hamilton, 1994) of gradient time series, and becomes clear if it is assumed that a gradient signal s_t at time t can be described by

$$s_t = \alpha s_{t-1} + n_t, \tag{3.10}$$

where n_t denotes the noise contribution at time t, and α is a constant describing the influence of past measurements on the momentary one. Of course, α is loosely related to the loop gain, but the exact relation depends on the actual implementation of the control system. Since, in closed loop $< s >= 0$, the auto-covariance is given by

$$A(L) =< s_t s_{t-L} > \tag{3.11}$$

Using Equation 3.10, this can be expanded to

$$A(L) = \alpha < s_{t-1} s_{t-L} > + < n_t n_{t-L} > . \tag{3.12}$$

Since noise will only be correlated at a lag $L = 0$ in this equation, it is possible to write

$$A(0) = \alpha A_{cl}(1) + \sigma_n^2, \tag{3.13}$$

$$A(1) = \alpha A_{cl}(0). \tag{3.14}$$

Isolating α in the second equation and putting it into the first then results in

$$\sigma_n^2 = (A(0) - A(1)) \frac{(A(0) + A(1))}{A(0)}. \tag{3.15}$$

This is already nearly identical to equation 3.9 for $d = 1$, save the factor of 2 in the denominator; originally, this factor was found empirically, but it can be mathematically founded by the following argumentation: strictly speaking, equation 3.10 does *not* operate on the individual x- and y-gradients of a subaperture, but on the gradient subvector $\vec{g}_i$ of the ith lenslet spot[5],

$$\vec{g}_t = \alpha \vec{g}_{t-1} + \vec{n}_t, \tag{3.16}$$

where the noise vector is taken from a radially symmetric Gaussian distribution with a variance of σ_r^2. Parting this equation to its individual components gives two equations of type 3.10 with noise terms $n_{x,t}$ and $n_{y,t}$. The magnitude of the noise, however, is not equal to σ_r^2 but has to be calculated as the x/y-directional expectation value given the radial distribution:

$$\begin{aligned} \sigma_x^2 &= \frac{1}{2\pi\sigma_r^2} \iint_{-\infty}^{\infty} dx dy \; x^2 e^{-\frac{r^2}{2\sigma_r^2}} \\ &= \frac{1}{2\pi\sigma_r^2} \int_{-\infty}^{\infty} dy \; e^{-\frac{y^2}{2\sigma_r^2}} \int_{-\infty}^{\infty} dx \; x^2 e^{-\frac{x^2}{2\sigma_r^2}} \\ &= \frac{1}{2\pi\sigma_r^2} \sqrt{2\pi\sigma_r^2} \sqrt{2\pi\sigma_r^2} \frac{\sigma_r^2}{2} \\ &= \frac{1}{2}\sigma_r^2, \end{aligned} \tag{3.17}$$

[4]Rounded to the nearest integer.

[5]In a modal control system, the control loop effectively shortens the displacement vector present in each subaperture.

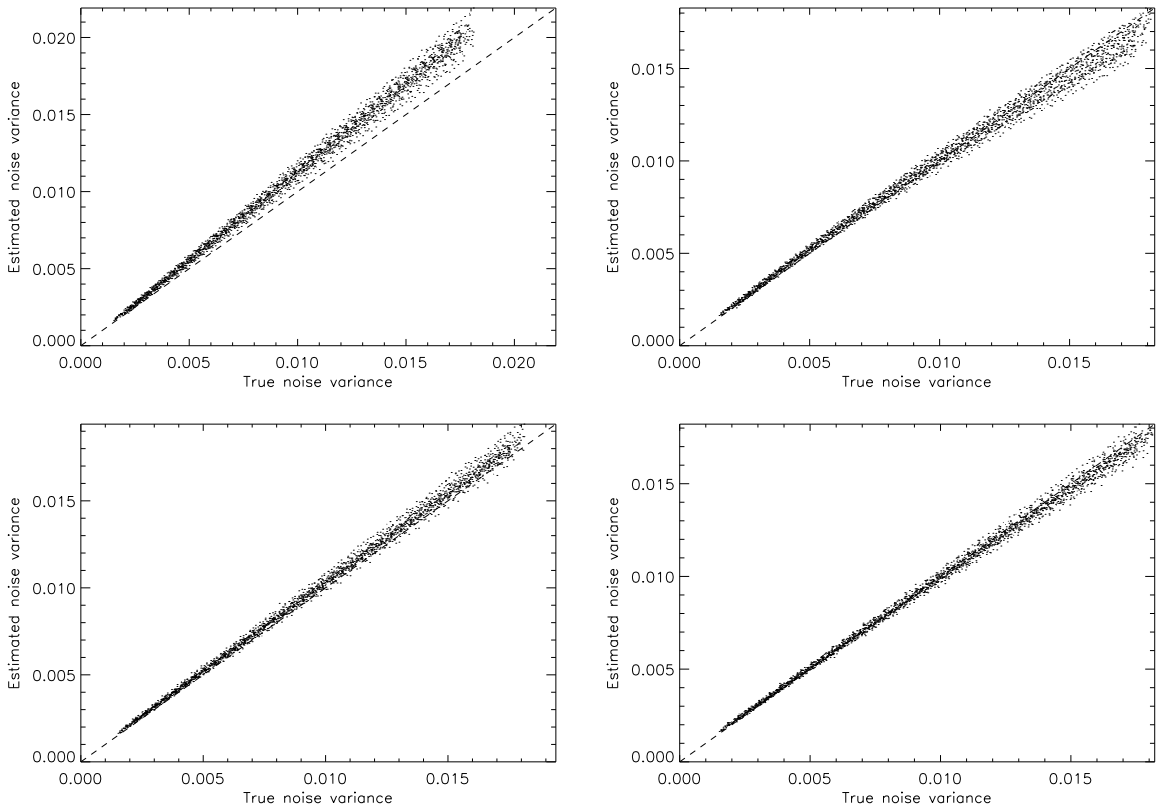

Figure 3.14: *Assessment of noise estimation accuracy for the direct difference (left) and the weighted difference approach (right) for loop delays of one cycle (top) and two cycles (bottom).*

and likewise for σ_y^2. This means, that for equation 3.10 to be valid on an individual direction, the noise contribution has to be multiplied by $\sqrt{2}$, leading to the desired factor of 2.
Furthermore, the method can be generalized to higher loop delays: the first term is just the direct difference method value, with the second term taking the role of a corrective factor, that estimates the influence of the noise feedback on the decay of the auto-covariance function, resulting in equation 3.9 (subsequently called the *weighted difference method*).
A simulation was used to compare the noise estimation accuracy of the direct difference and the weighted difference approaches. A recorded open-loop gradient file with a very low noise level was augmented with pure Gaussian noise of increasing magnitude; the modified gradient file was then used as input to a ALFA closed-loop simulation, using the corresponding interaction matrix obtained from the ALFA observing run. The closed-loop gradients forming the output of the simulation were then subjected to the two different noise estimation approaches. Figure 3.14 shows a comparison of the results for loop delays of 1 and 2 cycles. There is a clear tendency of noise overestimation in the direct difference approach, best visible at high noise levels; the result is an average overestimation of the noise actually present by about 9%. Although the weighted difference method shows a higher spread of estimates at high noise, the noise found is on average only 1.1% lower than the expected value, clearly a big improvement over the direct difference method. The differences are less pronounced for a loop delay of 2, with the first method overestimating at an average of 3.8% and the new method by 1.0%.

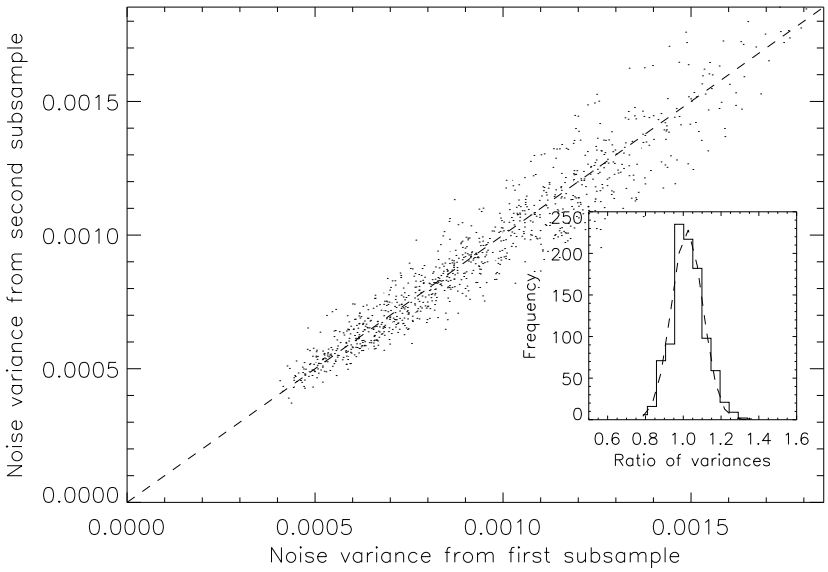

Figure 3.15: *Comparison of noise variance estimations from subsamples; the dashed line indicates a ratio of 1. The histogram of observed ratios together with a fitted Gaussian is depicted in the inset.*

It should be noted that the weighted difference approach is not suitable for loop delays higher than 2, where the direct difference delivers better results. This, however, is not a strong restriction, since high loop delays do only appear at very high correction frequencies (at about 600 Hz for ALFA). For future systems, a delay of close to 1 is expected to be the rule rather than the exception, since hardware speeds of DSPs are constantly increasing.

Estimation Consistency and Real-Time Implementation

Finally, a similar consistency check as for the open-loop case was carried (see figure 3.15 out and again found the values from the sub-series to be consistent within 8%.
A big advantage of the presented method is the fact that the real-time implementation presented for the open-loop data can also be used without changes. The knowledge of the first three autocorrelation coefficients of each gradient is sufficient to reliably estimate the noise levels in closed-loop operation.

3.3 Obtaining atmospheric parameters

The performance of an AO system is strongly influenced by the momentary configuration of the atmospheric turbulence parameters r_0, and θ_0. It is therefore highly desirable to achieve accurate estimates of these quantities, which can be used to optimize the settings of the AO's adjustable parameters or help in the interpretation of scientific data obtained using the AO.
This section deals with measurements of atmospheric parameters obtained by SCIDAR and from simultaneous observations with ALFA/Omega Cass, addressing the following questions:

- shape of a typical Calar Alto turbulence profile $C_n^2(h)$
- temporal stability of both the Fried parameter r_0 and the isoplanatic angle θ_0,
- and the consistency and reliability of parameter estimates from open- and closed-loop control system data.

Furthermore, the knowledge of the $C_n^2(h)$ profiles is essential for off-axis PSF reconstruction, as discussed in chapter 2.3. The results of this section have been partially published in (Weiß et al., 2002a) and (Weiß et al., 2002b).

3.3.1 Measurements and Data reduction

As described in Chapter 2, SCIDAR observations have to be done on bright visual binaries. Tables 3.1 and 3.2 give the essential data on the stars used for the measurements presented here. Note that the

Object Name	RA	Dec	M_{tot}	ΔM	$\Delta\alpha$ [“]	Δh [m]
γDel	20:46:39.2	+16:07:27.0	4.76	1.13	9.6	186
95Her	18:01:29.9	+21:35:42.5	4.3	0.1	6.6	284

Table 3.1: Binaries used for SCIDAR atmospheric profiling

vertical resolution of SCIDAR measurements is related to the angular separation $\Delta\alpha$ of the binary's components and the pixel sampling d_s in the SCIDAR analysis plane by $\Delta h = d_s/\Delta\alpha$. On August 31,

Object Name	Guide Star	RA	Dec	M_V	Exp. time [s]	Filter
γDel	HD 197963	20:46:38.9	+16:07:26.9	5.14	1.00	K+Brγ
IC 1396	HD 206267	21:38:57.6	+57:29:30.5	5.83	0.84	K

Table 3.2: Guide stars used for ALFA/Omega Cass measurements

2000, both instruments were pointed to the same target during all observations of 95Her and γDel; on September 1, 2000, however, SCIDAR measurements were carried out on γDel while ALFA/Omega Cass observed the open cluster IC 1396, about 40 degrees away from the SCIDAR binary, in order to check for possible dependencies of atmospheric parameters on the viewing direction. Elevation angles for both objects, however, were nearly identical.

SCIDAR Data

The data reduction process for SCIDAR data basically followed the lines already explained in section 2.1. Each of the measurements consists of 2048 pupil images recorded at a temporal sampling frequency of 383 Hz, which were used to calculate the mean-normalized auto-covariance of the scintillation in the SCIDAR analysis plane. With the help of SCAVENGER (see appendix B) a profile according to equation 2.28 was extracted and the inverse problem of equation 2.29 solved by conjugate gradients in order to obtain an estimate of the momentary $C_n^2(h)$-profile; this profile was then scaled to the zenith direction from the actual binary elevation. With this result, estimates of the atmospheric parameters were calculated using equation 2.7 for r_0 and equation 2.13 for θ_0.
Of course SCIDAR measurements are affected by noise, most notably by a sampling error in the observation plane and photon noise amplified by the intensifier. While the photon noise is quite small for a given distance range (Prieur et al., 2001), the sampling error one was found to be of significance. The sampling goal of the used setup was $d_s = 0.01$ m/pixel on the SCIDAR camera. Measuring the size of the pupil image for several parts of a single run revealed a variation on the order of about one pixel, giving $d_{s,meas} = 0.0104 \pm 0.0001$ m/pixel, effectively constituting a height sampling error. This error might be caused by vibrations or flexure of the SCIDAR instrument; although, at about 1%, it seems relatively small, it translates to an error of around 5% in the determination of r_0 and θ_0 from $C_n^2(h)$ profiles through uncertainties in the knowledge of dh. Finally, the contribution of errors in the solution of the inverse problem was taken into account by assigning the noise estimates of the conjugate gradient inversion process to each point in the $C_n^2(h)$ profile.

Omega Cass Data

Omega Cass images of γDelphini and IC 1396 were used to estimate r_0 and θ_0 using the configuration as listed in table 3.2.
By measuring the FWHM of each bright star in the field of view of open-loop images (two for γDel, four for IC 1396) r_0 was obtained using

$$\hat{r_0} = \lambda/\mathrm{FWHM}, \tag{3.18}$$

with the error estimated by the Fried parameter differences between the stars. Additionally, 15 single exposures respectively, spreading over a time of approximately 25 seconds due to readout delay, were taken from a set of 60 images total to expose a possible time dependence of r_0.
The isoplanatic angle was estimated from closed-loop images by a similar procedure, determining the Strehl ratio S of each star (again two for γDel but this time only three [6] for IC 1396), and fitting the results to

$$\hat{\theta_0} = \alpha_i \left(-\ln \frac{S_i}{S_0} \right)^{-1/2}, \tag{3.19}$$

where α_i is the distance of the ith star from the guide star, S_i its Strehl ratio, and S_0 the Strehl ratio of the guide star; the estimation error is naturally given by the fitting error. Note that there is some debate on the value of the exponent in this equation, with a theoretical value of $3/5$ for perfect on-axis correction. For low-order correction, however, Roddier (1999) argued that $1/2$ should be used with the exact value depending on the number and type of corrected modes.

[6] The guide star was overexposed and thus not usable.

Loop Data

Gradients were recorded in both open- and closed-loop imaging mode. In all cases, the KS28 array and a sampling frequency of 300 Hz was used, with a closed-loop gain setting of 0.5 on the first day and 0.4 (due to worse seeing) on the second. Thus, the 18000 gradient sets in each measurement correspond to 60 seconds of observation. Open-loop data was straightforwardly processed by estimating noise as described in the previous chapter and using equation 2.57, while closed-loop data was first subjected to the ALFA loop simulation to obtain the variances of the mirror modes, with noise estimated from the gradients with the weighted difference method. With this information, r_0 was then estimated according to equation 2.74.

3.3.2 Survey of SCIDAR Measurements

The measurements presented here are from two 50 minute sections of the August 31 (subsequently Day 1) and September 1, 2000 (Day 2) measurements; they were selected since they offer a fairly continuous coverage of this period of time, were recorded in generalized SCIDAR mode (making the ground layer visible) and coincided with gradient measurements at the ALFA system.

Overview

Figure 3.16 shows a survey of the selected SCIDAR results of August 31, 2000. The center plot gives the color-coded $C_n^2(h)$ profiles over time, while the top and bottom plots show the values of the Fried parameter r_0 at 500 nm and the isoplanatic angle θ_0 at 2.2 μm, as derived from the profiles. Seeing conditions during the measurement were excellent with 0.6" FWHM in V-Band. The same quantities on September 1, 2000 are shown in figure 3.17; on this day, the seeing was more typical for Calar Alto with an FWHM of 1.1" in V-Band.
The structure of turbulence on both days shows a strong domination of the ground layer. This is expected, since the thermal interaction of air and surface as well as obstacles and the geography of the site are a source of turbulence even in low winds. There are, however, two notable differences of the ground layer configurations on the two days: while the maximum C_n^2 value is only about 1.5×10^{-16} $\mathrm{m}^{-2/3}$ on Day 1, it reaches a peak value of 6.0×10^{-16} $\mathrm{m}^{-2/3}$ on Day 2. Additionally, turbulent activity seems to be confined to the immediate ground level on the first day, extending only to around 500 m (coinciding with the instrumental resolution), it clearly exceeds 1 km in height on the second day. The consequence of these differences is directly visible in the r_0 estimates won from the profiles, yielding 17.5±2.7 cm on Day 1 and only 10.2±0.01 on Day 2. Turbulence eases off at about 10 km from ground level, which, taking into account that the Calar Alto observatory is situated at approximately 2.2 km, corresponds to the typical tropopausic level. The turbulence between ground level and tropopause, however, is very different on the two days. Day 2 exhibits a very simple structure with basically only ground and tropopausic layers present, while for Day 1 a whole region of relatively strong turbulent activity can be identified, ranging from 3 to 10 km above ground. Within this region, at distances of 3, 6 and 9 km respectively, variation of turbulence strength is strongest, sometimes more than doubling from the underlying level of activity. The most stable of these disturbances is at 6 km, which seems to steadily built up during the observation period, while both the 3 km and 9 km layers show only intermittent presence. All in all, the Day 2 turbulence structure is much more stable, where relatively weak variations occur only in layers already present. The only interesting feature is the slow ascent and descent of the tropopausic layer between 9 and 10 km, a phenomenon that might be related to atmospheric gravity waves (the *Brunt-Vaisala* period of tropospheric waves is typically around 10 minutes (Nappo, 2002)).

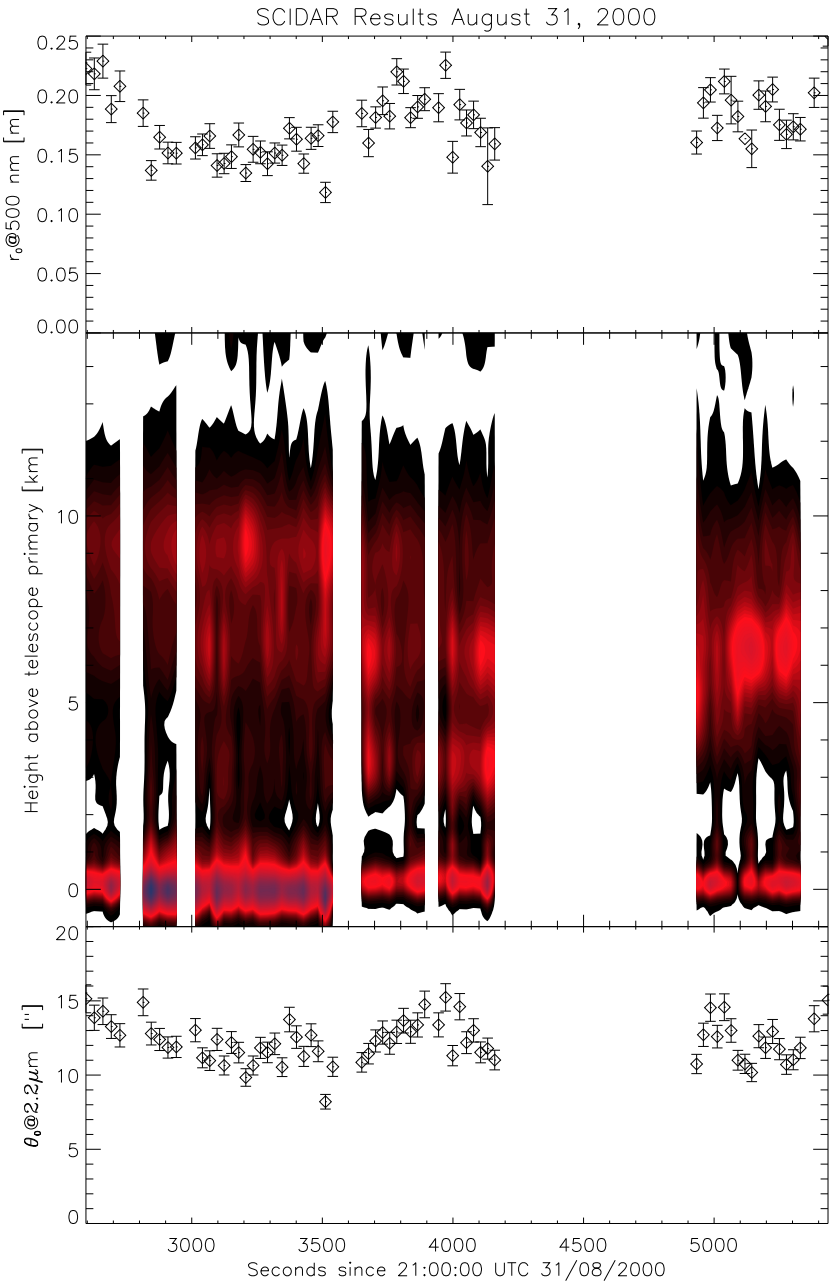

Figure 3.16: *Overview of SCIDAR results for August 31, 2000. Legend on the right of figure 3.17.*

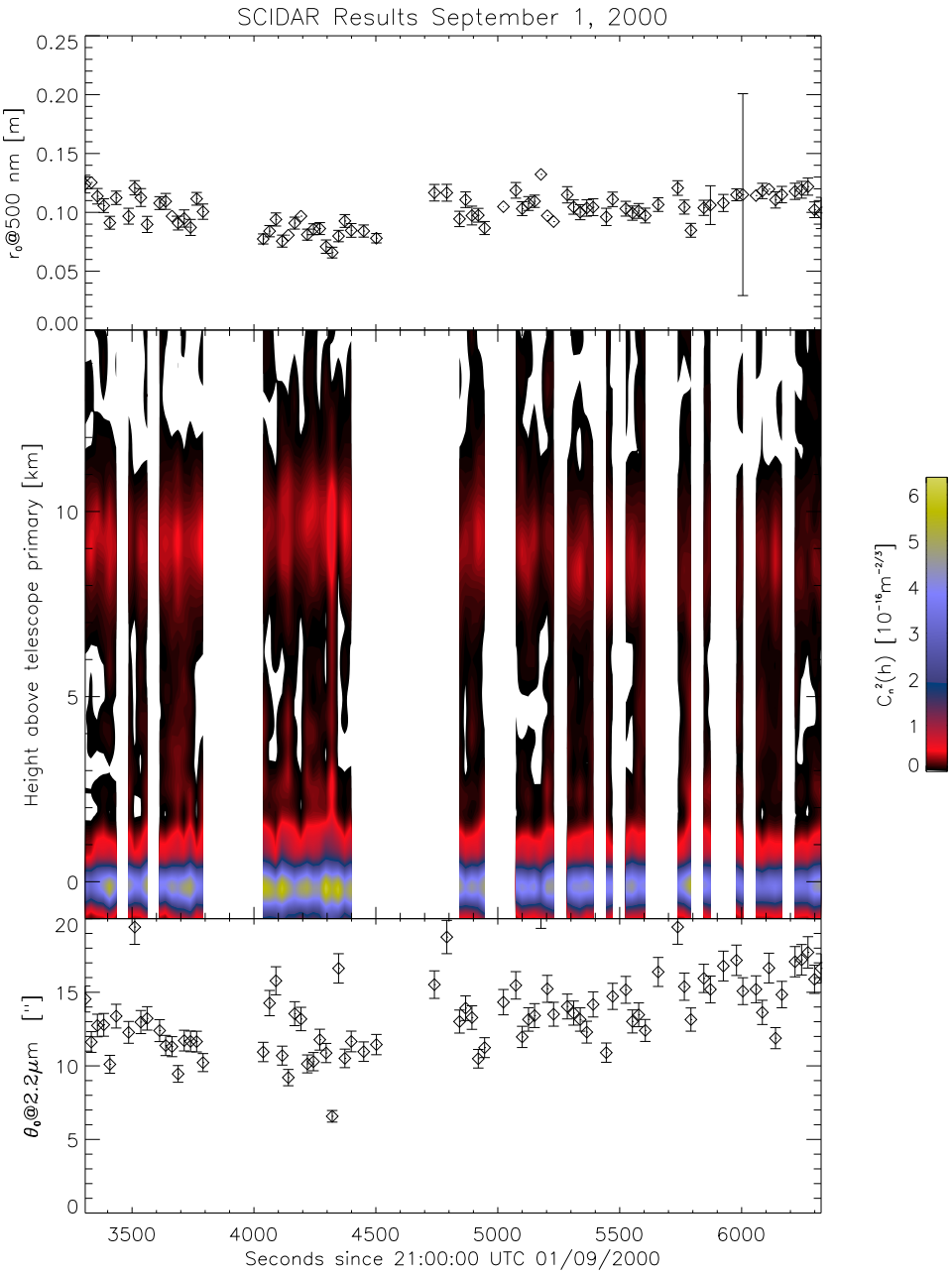

Figure 3.17: *Overview of SCIDAR results for September 1, 2000.*

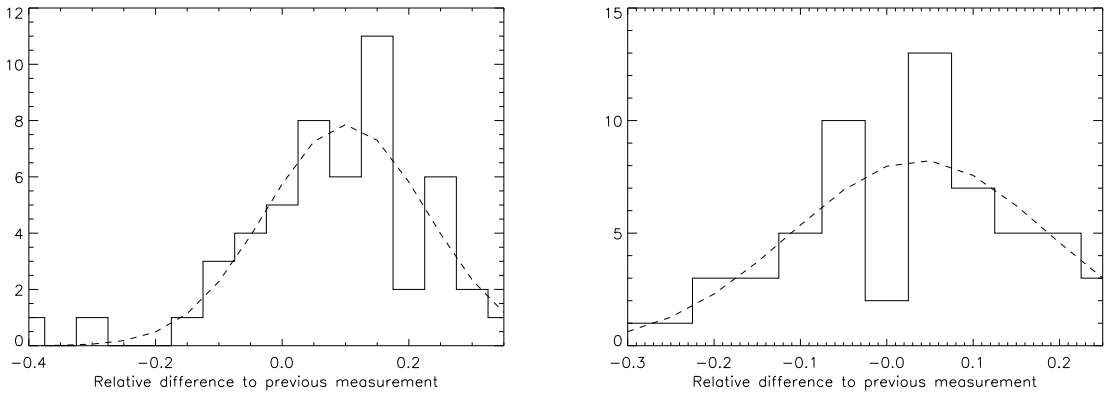

Figure 3.18: *Histograms of the difference in subsequent measurements of r_0 30 seconds apart; data obtained on August 31, 2000 (left) and September 1, 2000 (right). A Gaussian fitted to both histograms is depicted by the dashed line.*

The different structures of the atmospheric turbulence do not lead to much different isoplanatic angles, with 12.3"± 1.4" on Day 1 and 13.5"± 2.6" on Day 2. The strong height dependence of θ_0 (cf. equation 2.13) thus implies that turbulent activity in the upper part of the troposphere must be higher on Day 1 than on Day 2; in fact, integrating $C_n^2(h)$ from 3 to 15 km on both days, reveals that the turbulence content in this region is on average a factor of 1.4 higher on the first compared to the second day.
Usually it is expected that the ground layer dominates the value r_0 while the highest layers are responsible for much of θ_0. The atmospheric structure on Day 2 shows exactly this behavior; a calculation of the Fried parameter with integration reaching only to 5 km already accounts for 74% of the total, while a similar calculation for the isoplanatic angle starting at 5 km is nearly sufficient, since the value thus obtained is 98% of the total. If the same calculation is carried out for the atmosphere on Day 1, the first 5 km give only 34% to 42% of the whole atmosphere r_0. Additionally the influence of the 3 km turbulence is non-negligible for θ_0, reducing the contribution of the upper part of the atmosphere from 98% to 90%.

Temporal Statistics of the Fried Parameter

Another interesting feature of the SCIDAR measurements is that they allow to examine the temporal behavior of the derived atmospheric parameters. Since r_0 enters the PSF reconstruction algorithm at various points the knowledge of temporal development is crucial in order to determine just how long it can be regarded as stable.
Since single profile measurements are roughly 30 seconds apart during a SCIDAR observation, this time period has been used for the examination. Figure 3.18 shows histograms of the relative difference between r_0 estimates 30 seconds apart. Also shown are Gaussians fitted to the histograms. The fact that this Gaussians are not centered on zero reflects suggests there is a predominantly increasing trend present on r_0 on both days. More interesting, however, is the fitted standard deviation, which amounts to 12.8% on Day 1 and 14.9% on Day 2. Assuming that measurement error on r_0 is independent of the variations, these values reduce to 11.0% and 13.1% on the first and second day respectively. This result precautions against using the same Fried parameter for PSF reconstruction purposes for a period much longer than some tens of seconds. Although two days are too small a sample to deduce a

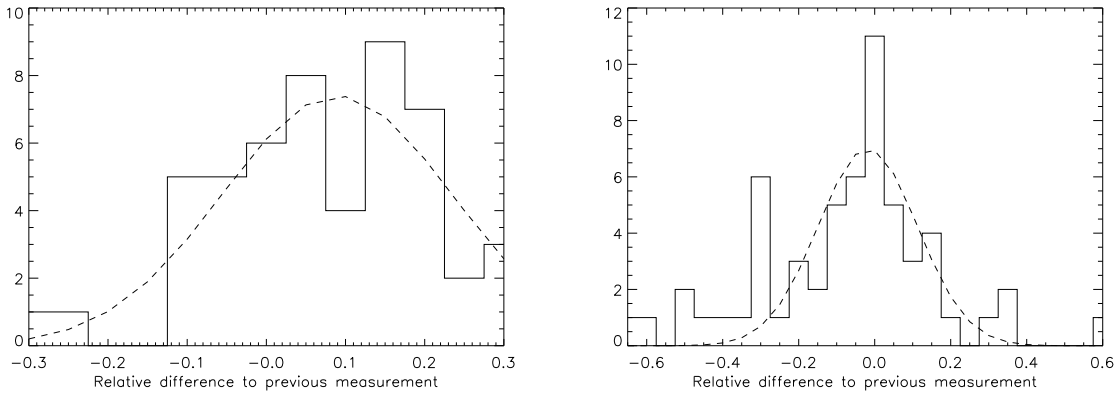

Figure 3.19: *Histograms of the difference in subsequent measurements of θ_0 30 seconds apart; data obtained on August 31, 2000 (left) and September 1, 2000 (right). A Gaussian fitted to both histograms is depicted by the dashed line.*

general statement, it seems that the temporal variation of r_0 does not strongly depend on seeing and/or structure of the turbulence, at least for good and median observing conditions.

Temporal Statistics of the Isoplanatic Angle

The same consideration as on r_0 has been carried out on the estimates of the isoplanatic angle. Figure 3.19 shows the results. Again, the decentering of the Gaussian reflects an increasing trend on Day 1 and a slightly decreasing one on Day 2[7]. The standard deviations found are not much different from that of the Fried parameter with (measurement noise reduced) values of 13.1% on the first and 11.8% on the second day; these results are even more important than that for the Fried parameter, since r_0 can be estimated from sources other than SCIDAR as well, while θ_0 is only reliably accessible from the C_n^2 profiles. For example, the use of balloon probe measurements of the turbulence profile for off-axis PSF reconstruction is completely ruled due to this short timescale variations. Additionally, it casts doubt on the argumentation (Fusco et al., 2000) that average atmospheric turbulence profiles are sufficient for off-axis PSF reconstruction.

3.3.3 Simultaneous Fried Parameter Measurements

Figure 3.20 shows the results of all Fried parameter measurements from the different instruments for the two selected days. As can immediately be seen, the r_0 estimates taken from Omega Cass images (triangles) agree very well with the SCIDAR measurements (diamonds) on both days[8]. Even when SCIDAR estimates are missing the values gained from the images seem to fill the gaps sensibly and nicely, which gives confidence in the reliability of parallel SCIDAR measurements for assisting AO. More important, however, are the estimates obtained from the ALFA control system. While the

[7]The estimates of the second day are influenced by outliers, which stem from spurious spikes in the C_n^2 profiles caused by light scattered into the SCIDAR instrument by clouds.

[8]This is an important result, since it establishes that dome seeing on the 3.5 m and the 1.23 m telescopes cannot be much different. Since these measurements where done, a ventilation system was installed at the 3.5 m telescope; it would be interesting to repeat the measurements in order to assess the impact of the ventilation.

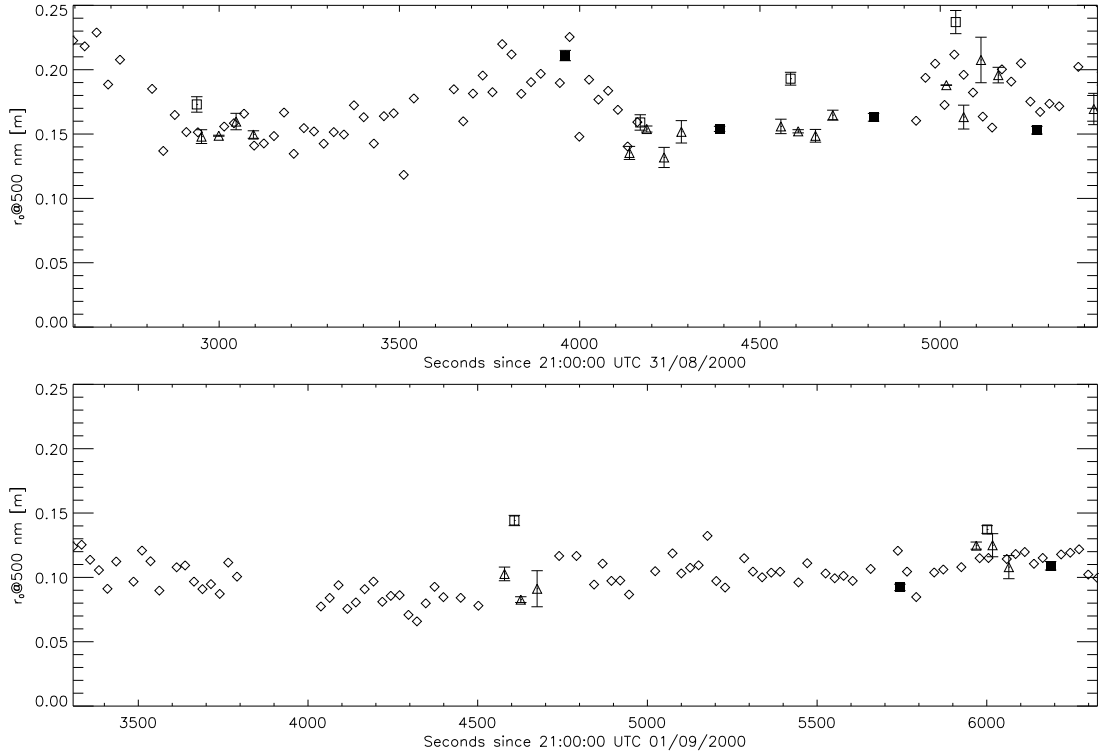

Figure 3.20: *Comparison of r_0 estimates from August 31, 2000 (top) and September 1, 2000 (bottom) as derived from SCIDAR (diamonds), Omega Cass images (triangles), open-loop (squares), and closed-loop (filled squares) ALFA gradients.*

Omega Cass values just served as a gauge for the coincidence of measurements on the two telescopes, the comparison of SCIDAR and ALFA estimates aims at a reliability check for the latter.

Estimates of r_0 from open-loop gradient data (open squares) show a slight overestimation on Day 1 that is even more pronounced on Day 2. This is in stark contrast to the excellent agreement of closed-loop gradient Fried parameter estimates (filled squares) with the SCIDAR data, exhibiting only a hint of underestimation on Day 2. The explanation for this fact lies in the way centroiding is done on the SHS CCD: during calibration a square region with a size of 3" by 3" around each reference position is determined, with only pixels lying within this region taken into account. An examination of the open-loop gradients revealed that they are biased, i.e. they show a constant offset from the reference position varying from measurement to measurement from 1" to 2". Since the star image size on the SHS is seeing limited, this offset, together with seeing disk size, leads to a PSF that lies partially outside the centroiding area; gradient lengths are therefore underestimated in turn leading to an overestimation of r_0. This also explains why overestimation is worse on Day 2, since seeing on this day was nearly double that of Day 1.

Of course, closed-loop centroiding is not affected by this problem, since the correction places the SHS PSFs near the reference positions.

It is not clear what is the reason for the slight underestimation of r_0 from closed-loop gradients on Day 2: it might either hint to a systematic error or be a consequence of the different viewing directions on Day 2.

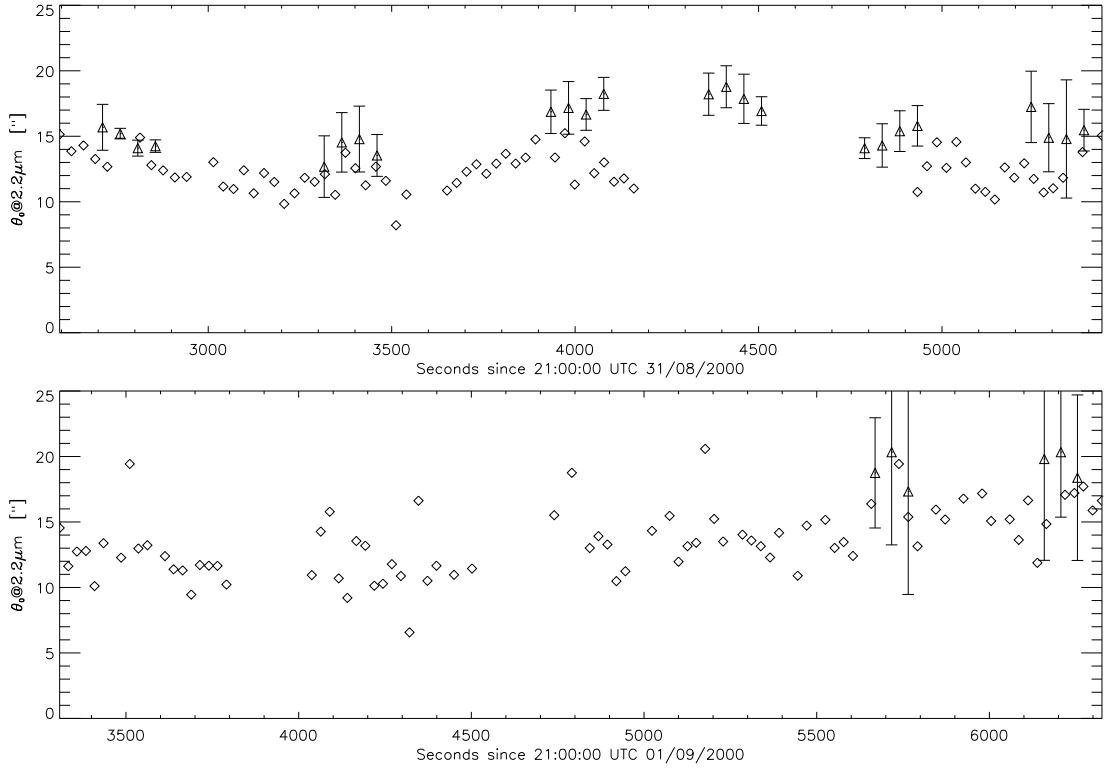

Figure 3.21: *Comparison of θ_0 estimates from August 31, 2000 (top) and September 1, 2000 (bottom) as derived from SCIDAR (diamonds), and Omega Cass images (triangles).*

3.3.4 Simultaneous Isoplanatic Angle Measurements

A comparison of the isoplanatic angles calculated from the SCIDAR measurements (diamonds) and deduced from closed-loop Omega Cass images (triangles) is shown in figure 3.21. At an image sampling of 0.08” the estimation of the Strehl ratios proved to be difficult, as is reflected by the large error bars accompanying the θ_0 estimates especially on Day 2. For this reason, the isoplanacy results are of reduced value. Leaving that restriction aside, the Omega Cass θ_0 estimates are almost always higher than those of the SCIDAR measurements. Remembering section 2.4, this is no surprise. In fact, the estimates are remarkably close to the minimum value defined by the SCIDAR profiles. Moreover, the temporal variations of the isoplanatic angle are moving largely in parallel between the instruments, again emphasizing the influence of turbulence fluctuations on image quality.

3.3.5 An Intermediate Summary

The results presented in this section served the purpose to show that the derivation of the Fried parameter from closed loop ALFA data is consistent with independently obtained results. Additionally it delivered information on the temporal behavior of the atmosphere, which turned out to be rather more variant than expected; changes in the spatial distribution of layers pose a potential problem for off-axis PSF reconstruction, thus $C_n^2(h)$ profiles used for this purpose should not be offset from an observation by more than a few minutes, contrary to the assumptions of earlier works on this subject. Also, the changes of r_0 and θ_0 on timescales of some tens of seconds place limits on time for which a PSF will sensibly be reconstructable.

Finally, the generally good agreement of Fried parameter and isoplanatic angle measurements between the SCIDAR instrument and ALFA/Omega Cass justifies the use of SCIDAR measurements for reconstruction purposes.

3.4 PSF estimation

In the preceding sections, the groundwork for the application of PSF reconstruction on the ALFA AO system was laid. With the availability of a reliable noise-estimation method and the knowledge of $C_n^2(h)$, all quantities need for the reconstruction are given. First, the quality of on-axis PSF reconstruction for bright and faint guide stars will be examined in K-Band; then attention is turned to an assessment of bright and faint guide star off-axis PSF reconstruction. These examinations will show the feasibility of the algorithms for the ALFA system. Finally, a photometry will be carried out in order to show improvents possible when using locally reconstructed PSFs for the examination.

3.4.1 Data Reduction

The goal of this section is to compare the shape of PSFs reconstructed from WFS measurements with those extracted from NIR, more specifically K-Band, images, taken simultaneously to closed-loop data. This comparison is complicated by the undersampling of the diffraction limited PSF, due to the long-lasting malfunction of the Omega Cass optics wheel (cf. section 3.1).
All images were subjected to a reduction procedure, consisting of the following steps:

1. A series of dome flatfield images with increasing exposure time were used to construct flat, bad and noise frames of the Omega Cass camera; these frames were assumed to be constant during the night.

2. Bad pixel correction was performed by adding a median filtered version of the image, multiplied by the bad pixel mask, to the original image, which in turn was before multiplied with the inverted bad pixel mask.

3. Where available, a sky background frame, treated for bad pixels the same way as described above, was subtracted.

4. Finally, pixel sensitivity variations were accounted for by dividing by the flatfield.

Keeping the results of section 3.3 in mind, the number of frames to be co-added was chosen such that the integration timespan (start of the integration of the first coadded image to the end of the last) did not exceed 30 seconds. Table 3.3 lists the observed objects together with some important imaging parameters[9].

Object	Type	airmass	Filter	Sky	Total Exposure Time [s]	Total Obs. Time [s]
95Her	binary	1.06	K+Brγ		540	1920
γ Del	binary	1.07	K+Brγ	X	833	3320
M92	globular cluster	1.64	K	X	460	1200

Table 3.3: *Objects observed for PSF reconstruction purposes.*

Table 3.4 lists the guide stars and loop parameter settings maintained during the observations. A total of 24000 gradient sets was recorded alongside each closed-loop exposure, corresponding to 80 seconds for 300 Hz and 320 seconds for 75 Hz loop operation frequency[10]. Of course, the number

[9] One of the reasons for the large difference between exposure and observation time is the need to stop the control loop in order to download recorded gradients.

[10] Available space was not fully exhausted in the 75 Hz case, since the closed loop-exposures lasted only about 90 seconds

Object	Guide Star	Brightness [m_V]	Loop Frequency [Hz]	Loop Gain
95Her	HD 164668	5.08 (7.08)	300	0.4
γDel	HD197963	5.14 (7.14)	300	0.5
M92	CSI+43-171569	13.	75	0.2

Table 3.4: *Guide stars and loop settings for the objects given in table 3.3. The numbers in brackets are the actual brightness on the SHS, which is lower since the ND2.0 filter was employed.*

of gradients was abridged before reduction to a length fitted to the integrated observing time of the images. From these gradients all quantities needed for on-axis PSF were obtained by the following steps:

1. Noise estimation was done using equation 3.9, giving the diagonal elements of the gradient noise covariance matrix $< \vec{n}\vec{n}^T >$. Off-diagonal elements of this matrix are negligible, as they could only be caused by strong variations of the sky background or transparency, which can safely be assumed to be small in the visual band. Transforming the noise according to $\mathbf{R} < \vec{n}\vec{n}^T > \mathbf{R}^T$ gave the noise covariance on the residual controlled modes $\hat{\vec{\epsilon}}$.

2. The next step was the recovery of the variance of the mirror modes $< \vec{m}\vec{m}^T >$. Since ALFA's control system is digital, these can be determined by feeding the recorded gradients $\vec{g}$ into a software version of the control algorithm (see also appendix C). The modal coefficients thus recovered have then to be doubled (mirror reflection) in order to recover $\vec{m}$. With these given, r_0 was estimated following the iterative algorithm described in section 2.3 using equation 2.74.

3. Finally, with the Fried parameter and noise known, the crucial matrices $< \vec{\epsilon}\vec{\epsilon}^T >$ and $< \vec{a}_\perp \vec{a}_\perp^T >$ were determined according to equation 2.73, scaling the theoretical KL modal variance matrix with r_0 as obtained in the previous step.

In principle, the results so obtained could be used directly to estimate the system OTF (and thus its PSF) following equation 2.68. But just the supposedly easiest part in this equation poses the biggest problem, namely the unaberrated system OTF $T(\vec{\rho})$. Due to the undersampling, the fiber image cannot be reliably used to estimate the contribution of residual aberrations; this owes largely to the fact that the exact positioning of the PSF on the 0.08"/pixel grid is not known and that the OTF obtained from the PSF carries no information beyond a frequency of approximately $0.7D/\lambda$. The only way to overcome this limitation was to measure the fiber image PSF's Strehl ratio and constructing an according modal covariance matrix. This was done by taking a 9×9 matrix, with its (0,0), (1,1) and (2,2) entries, corresponding to tip,tilt and focus variance, set to zero, as these aberrations can safely assumed to be absent in fiber imaging. The remaining diagonal entries were then set to equal values such that $S \approx \exp(\mathrm{trace} < \vec{a}\vec{a}^T >)$ was equal to the measured Strehl ratio. The corresponding OTF was finally taken to represent $T(\vec{\rho})$. While this approach serves to correct for possible overestimation of the Strehl ratio by the reconstruction process by limiting its maximum to that found on the fiber, it is not suitable to account for asymmetries present in the reference PSF.
A similar problem occurs when comparing the reconstructed to the extracted PSFs; if the reconstruction was carried out such that it directly delivered a PSF resolution of 0.08"/pixel, the shape would be by definition symmetric in the sense that the peak PSF intensity would be located exactly on the vertex of four neighboring pixels. To avoid this, the reconstruction and comparison process was done the following way:

1. The PSF delivered by the reconstruction algorithm was resolved at 0.04”/pixel.
2. From this PSF, slices in x- and y-direction were taken, and each pixel in these slices parted into 20 pixels with constant intensity.
3. The overresolved slices were then shifted and at each step regridded to a 0.08”/pixel resolution by summing the intensities in 40 sequential bins.
4. The resulting undersampled PSFs were then compared to PSF slices taken from the image PSFs selecting the reconstructed PSF such that the summed quadratic difference between the measurement and the reconstruction was minimal.

As shown in chapter 2.3, off-axis PSF reconstruction requires an additional term in the OTF. This term was calculated by selecting a nearby or synchronous $C_n^2(h)$ measurement obtained with SCIDAR and calculating $D_{ani}(\vec{\rho}, \vec{\alpha})$ as given by equations 2.77 and 2.78.
The next two sections show comparisons of selected samples of image PSFs to their corresponding reconstructed PSF.

3.4.2 On-axis PSF Reconstruction Results

The comparisons are done for x- and y-cuts of both PSFs along with a a radially averaged PSF. Contrary to other works on this topic, both PSFs are normalized to one in order to expose errors in its flanks. The quality of peak fitting is assessed by comparing the Strehl ratios of the reconstructed and the extracted PSF, given in a table accompanying each plot.

Bright Guide Star - Good Seeing

The first comparison is done on a 25 second exposure of 95Her recorded during a period with V-Band seeing of 0.6”. Loop gain at this time was 0.4. The results are shown in figure 3.22 and table 3.5. As can clearly be seen, the reconstruction quality is quite good, with the absolute difference between the PSFs nowhere exceeding 0.1. This becomes even clearer when looking at the OTFs: at lower frequencies, the error is well below 1% growing to 10-15% at higher frequencies. There are several possible sources for the high-frequency deviations, the most obvious being the insecure knowledge of the unaberrated system PSF. Looking at the residuals, it seems that errors mostly show up at the location of the first diffraction ring in the x-and y-cuts, and are much less severe in the radially averaged profile. This might hint to an asymmetry of the fiber PSF which is not accounted for by the modeling as described above.
The Strehl measured and the reconstructed Strehl ratios also agree remarkably well, with the slightly higher Strehl given in the reconstruction corresponding to the deviations of the OTF to the upside. The FWHM agreement is also quite good, especially taking into account the inherent inaccuracy of measuring its value on a 0.08”/pixel array.

	Measurement	Reconstruction
Strehl Ratio [%]	40.8±1.6	42.4
FWHM [“]	0.15±0.01	0.14

Table 3.5: *Strehl and FWHM values given by the image and the reconstruction of the guide star PSF for 95Her.*

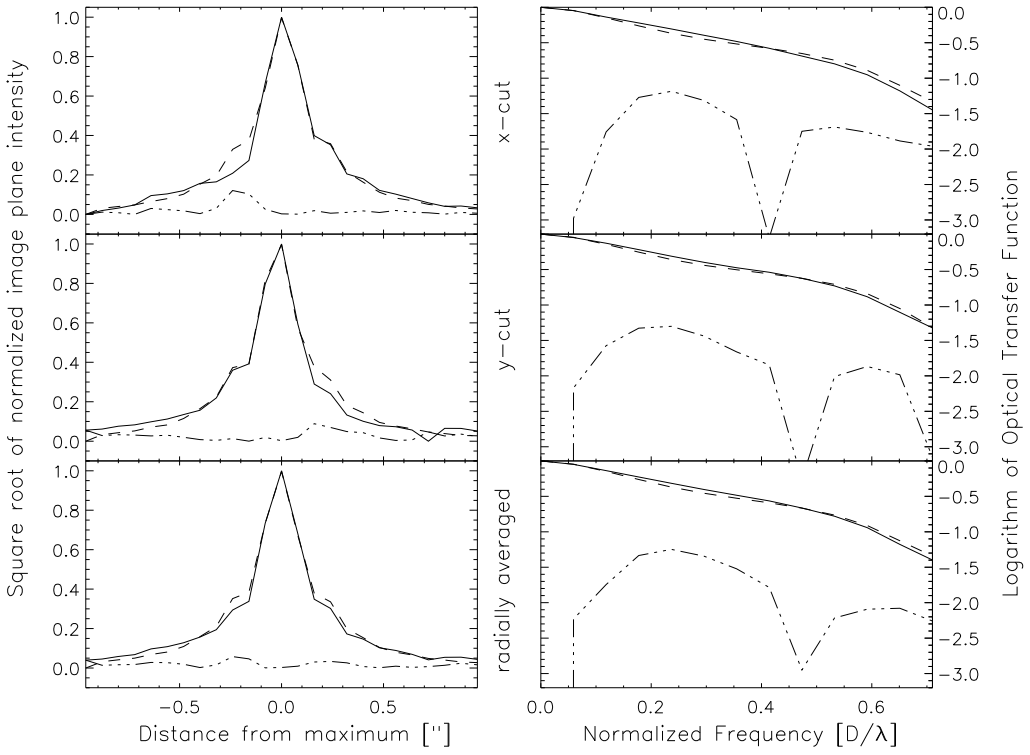

Figure 3.22: *Comparison of measured (solid) and reconstructed (dashed) PSF and OTF cuts for 95Her at a V-Band seeing of 0.6". The difference of each pair of curves is also shown (dash-dotted).*

Bright Guide Star - Median Seeing

The second example was taken on γDel on the same day approximately one hour later. Seeing had at this time degraded to 0.9" in V-Band, but still a higher correction quality was obtained due to the higher loop gain setting of 0.5, as can be seen from the slightly higher Strehl ratio of around 45%. Figure 3.23 and table 3.6 show the results for this case. On first inspection, the reconstruction quality is very good, even better than for the first example. Still, the difference between the PSFs is nowhere higher than 0.1, and strongest close to the first diffraction ring, further hinting to an unaccounted asymmetry of the fiber PSF. Additionally, the deviations are very similar between this star and the first example. This is an encouraging result, as it rules out a non-stationary error contribution unaccounted for by the reconstruction process. Looking at the OTF comparison, the agreement between the y-cut and radially averaged profiles is very good and generally close or even below 10%.

Finally, the measured and reconstructed Strehl ratios and FWHMs are very close, with both reconstructed values lying within one σ of the measured ones.

Faint Guide Star - Median Seeing

The last on-axis PSF example is taken from an observation of M92 on September 1, 2000. The conditions for this observation were very different from the previous examples in brightness as well as airmass (cf. table 3.3). Due to these conditions, the KS7 array was used with a loop frequency of 75 Hz and a loop gain of only 0.2. As this loop setup clearly represents a case with a loop delay of less

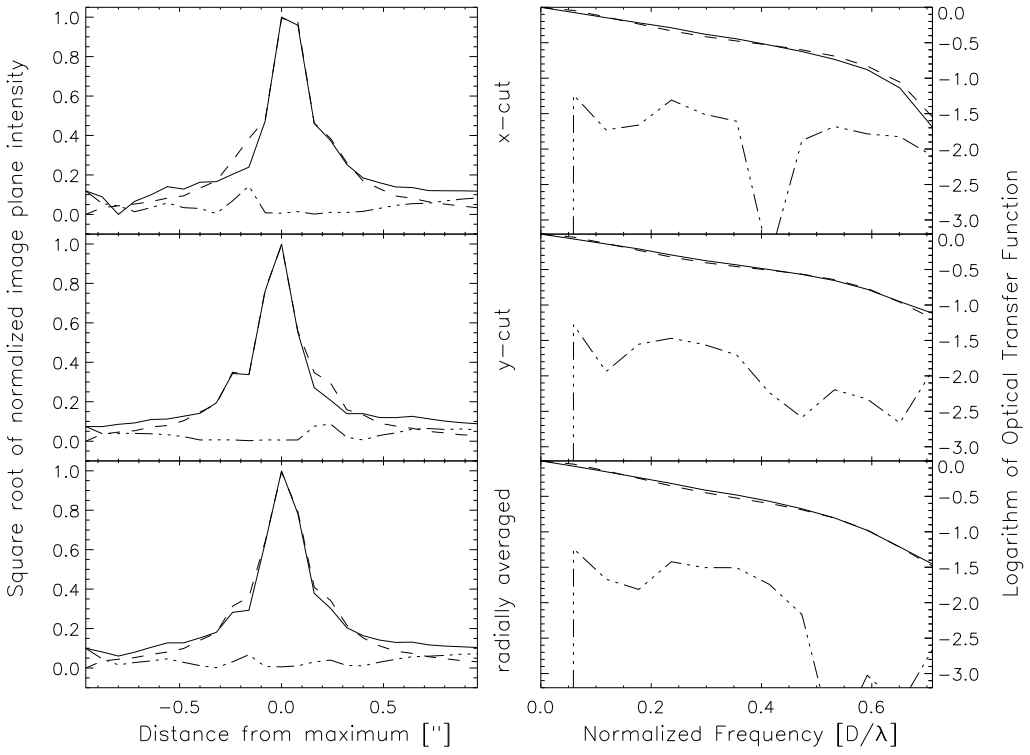

Figure 3.23: *PSF and OTF comparison for γ Del at a V-Band seeing of 0.9". Same legend as figure 3.22.*

	Measurement	Reconstruction
Strehl Ratio [%]	45.7±2.00	47.6
FWHM ["]	0.14±0.01	0.13

Table 3.6: *Strehl and FWHM values given by the image and the reconstruction of the guide star PSF for γDel.*

than one cycle, ita also served as a testbed for the noise estimation method developed in section 3.2. In fact, it turned out that no PSF reconstruction was possible unless the weighted difference estimation was used. The reason for this was that the measurements on M92 were associated with a fairly high noise level; the overestimation of noise by both the direct difference method and the parabola method in conjunction with the noise amplification by the control loop leads to *negative* variances in equation 2.74. This physically senseless result makes an estimation of r_0 by the iterative process described in section 2.3 impossible.

The PSF reconstruction results, using the weighted difference noise estimation method, are shown in figure 3.24 and table 3.7. The agreement of the PSF x-cuts is clearly very bad, while that for the y-cut and the radially averaged cut are surprisingly good. This discrepancy, however, can be easily explained by a non-common path aberration. Figure 3.25 shows a contour plot of the guide star and a nearby star, which both clearly exhibit a coma aberration. As will be seen later, this coma also appears on off-axis stars further away and seems to be of constant strength. As the only non-common path aberrations in the ALFA system can occur after the dichroid, the most probable explanations is a decentering and/or tilting of the Omega Cass camera, well possible at an airmass of 1.64 corresponding to a zenith angle

of 52 degrees. The other possibility, a static coma introduced by the ALFA SHS due to flexure of one of its components is ruled out by both the field-independent character of the coma and the absence of significant static coma terms on the mirror modes.

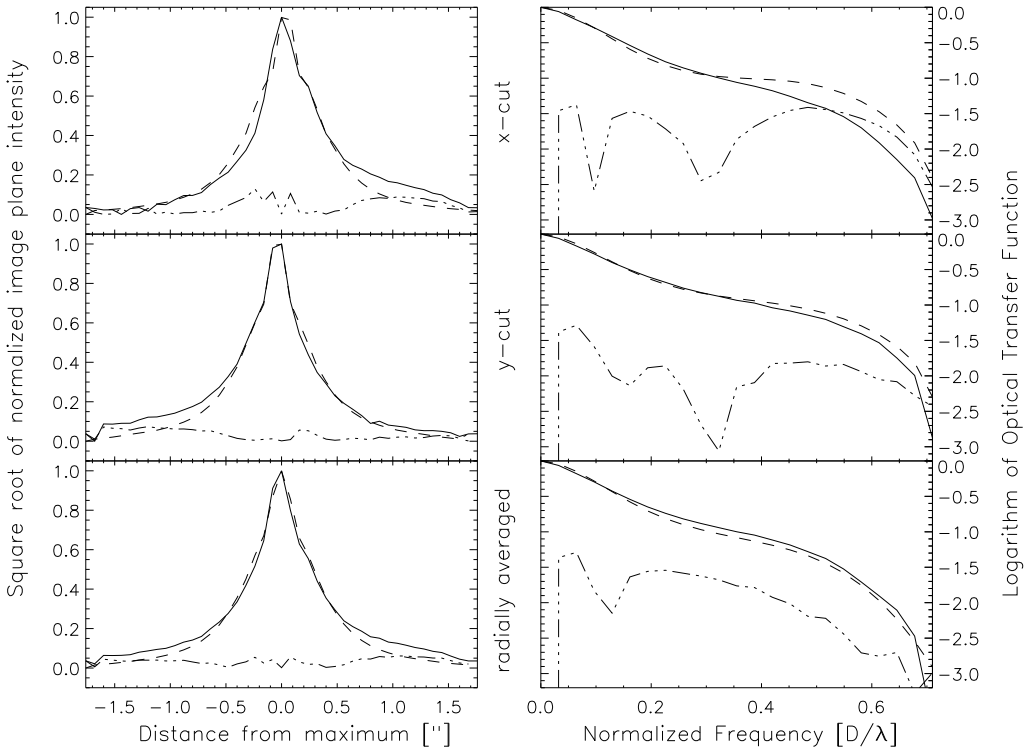

Figure 3.24: *PSF and OTF comparison for M92 at a V-Band seeing of 0.8" (1.1" when scaled by the airmass). Same legend as figure 3.22.*

	Measurement	Reconstruction
Strehl Ratio [%]	13.2±1.9	13.3
FWHM ["]	0.24±0.02	0.22

Table 3.7: *Strehl and FWHM values given by the image and the reconstruction of the guide star for M92.*

Ignoring the x-cut deviations, the y-cut of the PSF, that should be largely unaffected by the coma, shows remarkable agreement with the reconstructed PSF cut; this is even more true of the OTF, with relative error staying close to 10% up to frequencies of $0.4D/\lambda$.

While the relative error in the Strehl ratio estimation is much higher than in the bright star cases, the FWHM agreement is better than before, especially taking into account that a higher FWHM is expected on the measured PSFs due to coma. This partly reflects that the faint guide star PSFs are better sampled, with about 2.5 samples per FWHM instead of 1.6 for the bright star and good correction case.

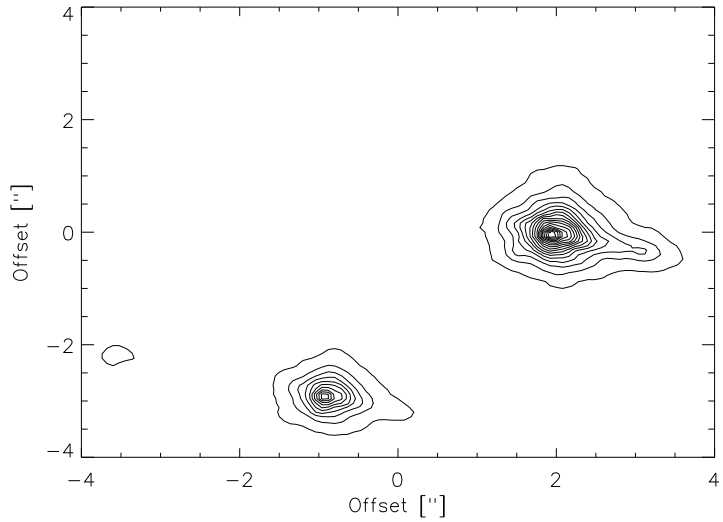

Figure 3.25: *Contour plots of the guide star and a nearby star for M92; offsets are from the center of the Omega Cass detector. Coma is clearly visible on both stars.*

3.4.3 Off-axis PSF Reconstruction Results

PSF reconstruction for stars far away from the guide star in principle requires the knowledge of the on-axis PSF. Earlier works (Fusco et al., 2000) have argued that this step could be skipped and perfect correction on the guide star assumed. While this argument leads to satisfactory results for very bright guide stars (and associated good correction), it is prone to fail for faint guide stars. As can be seen from equation 2.76 the $D_{ani}(\vec{\rho}, \alpha)$ can basically be regarded as a modification of the residual modal variance $< \vec{\epsilon}\vec{\epsilon}^T >$, save high order contributions which are comparatively small. The relative strength of the U_{ij} and the ϵ_{ij} thus determines the quality of the off-axis PSF. Especially for poor correction and low Strehl ratios achieved using a faint guide star, residual aberrations on the correction axis are comparatively high and are thus dominant far away from the guide star, leading to an effective isoplanatic angle much higher than its theoretical value (see below).
Another caveat in off-axis PSF reconstruction is the selection of the appropriate $C_n^2(h)$ profile. During the preparation of this work it has been noticed that the quality of the reconstructed PSF can be very sensitive to even weak variations of the upper troposphere; care has therefore been taken to only use atmospheric profiles either recorded in parallel or - if not available - within a time window of 10 minutes from the observation.

Bright Guide Star - Good Seeing

The first example is taken from the same exposure of 95Her as examined before, this time using the second component at a distance of 6.6” from the guide star. The results are shown in figure 3.26 and table 3.8. Note that the FWHM is not reported for off-axis stars, since it is generally different in x- and y-direction due to the elongation in the direction of the guide star.
On first inspection, the reconstruction quality is quite similar to the the on-axis case; with the short distance and a prevalent isoplanatic angle of 11.7”, this is not unexpected. Well inside the isoplanatic patch, the differences should be small as can also be seen from the Strehl ratio of approximately 38%

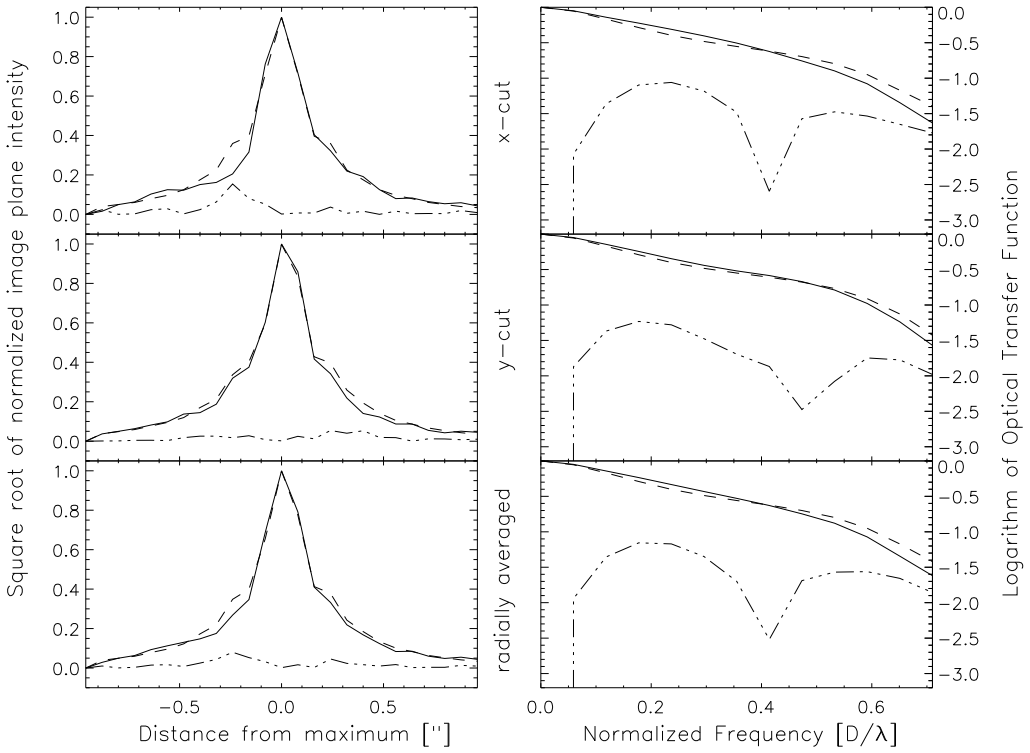

Figure 3.26: *PSF and OTF comparison for the second component of 95Her at a distance of 6.6" from the guide star and a seeing in V-Band of 0.6". Same legend as figure 3.22.*

	Measurement	Reconstruction
Strehl Ratio [%]	38.1±1.8	39.0

Table 3.8: *Strehl ratios given by the image and the reconstruction for the off-axis component of 95Her*

that lost only about 3% as compared to the guide star.
Looking at the PSF, the relatively strong deviation on the left diffraction ring region of the x-cut is still present, which establishes the presence of an unresolved asymmetry present on the calibration PSF. The y-cut and radial average PSFs, however, are estimated remarkably well. This is also reflected in the OTF comparisons, with absolute errors about the same order as for the on-axis case; the relative errors are higher, reaching about 15%, which is mostly a consequence of the generally lower OTF values for an off-axis star.

Bright Guide Star - Median Seeing

The next example is also located within the isoplanatic patch, but at a larger distance of 9.6". It is taken from the same exposure of γDel as for the on-axis case. The stronger influence of off-axis terms on the PSF can be immediately seen from the higher drop in the Strehl ratio of nearly 10%. The results of the reconstruction process are shown in figure 3.27 and 3.9.
The x-cut of the PSF shows the expected error at a position of -0.3" from the PSF center. This

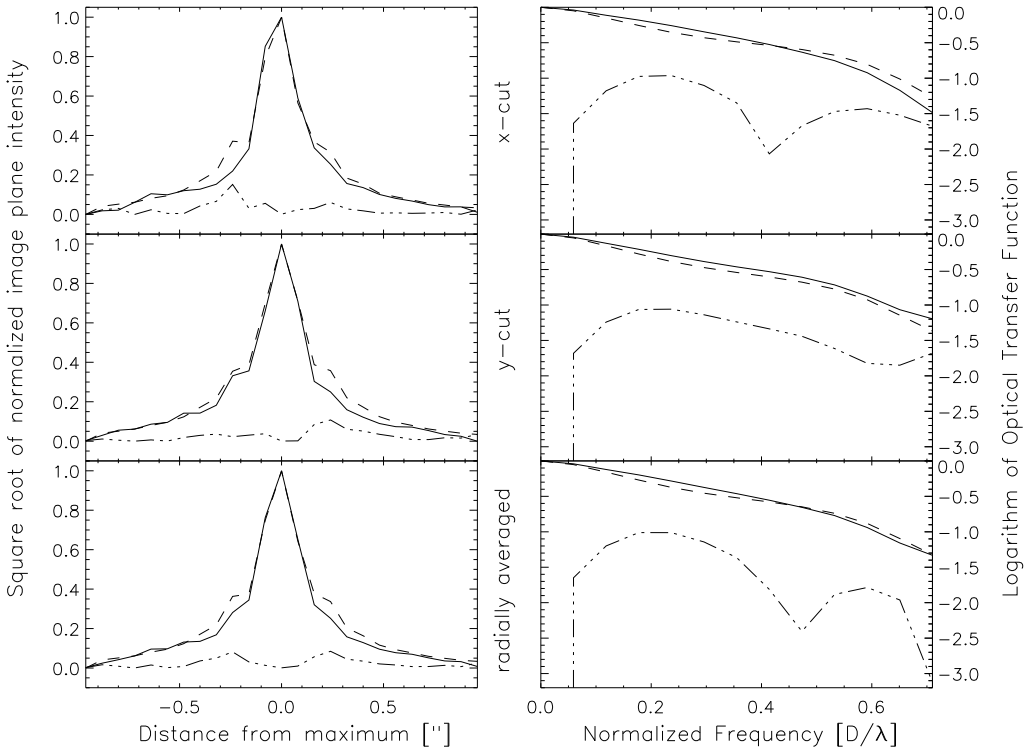

Figure 3.27: *PSF and OTF comparison for the second component of γDel at a distance of 9.6" from the guide star and a seeing in V-Band of 0.9". Same legend as figure 3.22.*

	Measurement	Reconstruction
Strehl Ratio [%]	34.2±2.2	36.5

Table 3.9: *Strehl ratios given by the image and the reconstruction for the off-axis component of γDel.*

time, however, there are also stronger deviations present on the y-cut and the radial average of the PSF. Although the overall reconstruction quality is still satisfactory, these deviations could hint on a systematic error originating in the unknown outer scale of turbulence during the observations. This assumption is further strengthened by the fact that the relative OTF reconstruction error is significantly higher than in the previous examples over nearly the whole spatial frequency range: an error in the estimation of the contribution of low spatial frequency modes, like tip, tilt, and focus, which are most affected by the outer scale, would show exactly this behavior. Interestingly, Fusco et al. (Fusco et al., 2000) found a similar discrepancy in their studies of the anisoplanatic PSF.

Faint Guide Star - Median Seeing

The last example is an off-axis star on the M92 image. This star lies far outside the isoplanatic angle of 11.7" prevalent at the time, especially when scaled to the corresponding airmass which results in a θ_0 of only 5.5". The results of the reconstruction are shown in figure 3.28 and table 3.10.
The x-cut of the measured PSF is still contaminated by a a coma contribution to the right side of

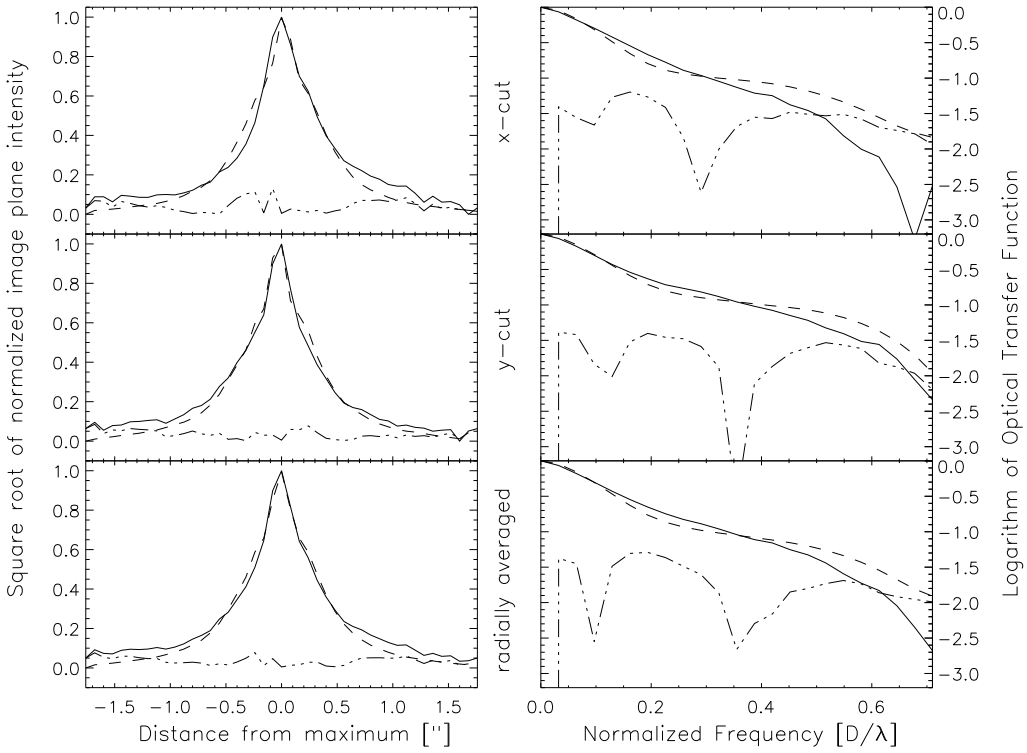

Figure 3.28: *PSF and OTF comparison for the second component of M92 at a distance of 15.3" from the guide star and a airmass-scaled seeing in V-Band of 1.1". Same legend as figure 3.22.*

	Measurement	Reconstruction
Strehl Ratio [%]	7.6±1.41	9.3

Table 3.10: *Strehl ratios given by the image and the reconstruction for the off-axis example from M92.*

the peak intensity, emphasizing the field independent character of this imaging aberration during the observation. The y-cuts and radial averages of reconstructed and measured PSF, however, again agree remarkably well considering the difficult conditions; the strongest deviations originate from high frequency bumps, which are a consequence of the comparatively low SNR for the fainter star as compared to the bright star examples. These high spatial frequency deviations are also clearly visible in the OTF comparisons, where starting from around $0.5D/\lambda$, the error is close to or even higher than the actual value of the OTF. In the lower frequency range, the reconstructed OTF shows the same tendency of underestimation as in the previous cases, caused by the calibration PSF uncertainties, and being more pronounced in this case due to the lower underlying magnitude of the OTF.
While the difference of the measured and reconstructed Strehl ratios is relatively high for this example, it still lies safely within 2σ of the measurement error.

Altogether, the PSF reconstruction results presented here are very satisfactory, especially given the difficulties associated with the undersampling of the measurements. It should be noted that the selection of the examples is representative in the sense that they are not taken from particularly good or bad cases, but were chosen such as to show the typical quality of reconstruction under the given set of circumstances.
We are confident that if a properly sampled calibration PSF was available, the small low-frequency estimation errors of the OTF would be largely accounted for. This assumption is founded on the fact that the strongest deviations of the PSF shapes do always appear at the same location, namely to the left of the x-cut and to the right of the y-cut peaks. This clearly points to a static nature of the deviations, in contrast to the results found by Harder and Chelli (2000) in their work on PSF reconstruction for SHS systems, who found non-stationary differences that strongly impaired the quality of their fits. As of writing (March 2003), measurements at Calar Alto are underway to provide very high-resolution (0.04”/pixel) images alongside WFS data.
While the overall quality of the reconstruction does not fully reach that found on CWS based systems, we suspect that much of this difference would disappear for adequately sampled data.

3.4.4 Photometric Reduction

As a last step, the PSFs reconstructed over the whole field of view will now be used to perform photometry on two binaries and the outer fringes of the M92 globular cluster. Again due to the undersampling of the images, this proved to be quite difficult; since the exact placement of the PSF on the image grid is a priori unknown, the CLEAN deconvolution, delivering very accurate results on simulated images (cf. section 2.4), could not be successfully applied.
Instead, it was necessary to use a generalization of the method of the preceding section to achieve satisfactory results that consisted of the following steps:

1. First, a grid of reconstructed PSFs was calculated, using the gradient and atmospheric turbulence data, that spans from the guide star PSF to the most distant point in the field of view. This calculation was done at a resolution of 0.04”/pixel and at PSF distance steps of 1” starting with at the guide star.

2. Then, measured PSFs were extracted from the images at the locations of the stars on which photometry was to be applied.

3. Then, by interpolation and rotation, the appropriate estimated PSF for each of the photometry locations was generated.

4. The reconstructed PSF was fitted to the measured PSF by first subdividing each pixel of the estimation into a 20×20 grid of identical intensity of 1/400th of the original pixel intensity; subsequently, this new gird was shifted stepwise over the whole range of 20 pixels in both directions, at each step projecting to a resolution of 0.08"/pixel by summing intensity within 40×40 subarrays of the grid. For each resulting undersampled PSF the following quantity was minimized

$$\chi^2 = \sum_{i,j} \left[\frac{I_{ij} - \xi R_{ij} - b}{\sigma_{ij}} \right]^2 , \tag{3.20}$$

where I_{ij} is the intensity of the measured PSF at pixel (i, j), σ_{ij} its associated noise (with $\sigma_{ij} = \sqrt{I_{ij}}$ assumed to follow Poisson statistics), R_{ij} the intensity of the reconstructed PSF at location (i, j), which is linearly fitted to the measured PSF via ξ ("peak intensity") and b ("background").

5. Finally, the projection for which χ^2 as defined in the previous step was minimal was considered as the best fit.

Multiplication of ξ with the total brightness of the normalized reconstructed PSF then gave an estimate of the flux on the selected star. It should be noted that for most of the examples given here, this method is overly complicated since the separation between stars is large enough to safely assume that their PSFs are not overlapping, making aperture photometry possible. The purpose of this section, however, is to reveal and check improvements in photometric accuracy when using a locally reconstructed PSF as opposed to a global one. The advantages of this approach will come to pass in observations of dense clusters and nearby galaxies, where the mutual distances of the interesting objects are far too small to apply aperture photometry.

Bright Guide Star: γDel and 95 Her

The first photometry example are the bright binaries γDel and 95Her; open- and closed loop images of the systems are shown in figure 3.4.4. As seen in the previous sections, both the on- and off-axis reconstruction quality was very good on both stars, thus a conclusive improvement of the photometric estimation is expected in both cases. Table 3.11 shows the results of the photometry, where *OL Aperture* are the results obtained from a two minute open-loop exposure with aperture photometry (which is used as a reference), *CL on-axis* the values obtained with using the reconstructed on-axis PSF on both stars, and *CL local* the results given by fitting the locally reconstructed PSFs. As can be seen, the local results are clearly superior, reducing the photometric error from more than 10% to 3.5% for 95Her and from more than 25% to 3.9% for γDel; while the errors of the local method are comparable for both stars, the much higher error using the global PSF on γDel in part reflects the higher distance between the guide star and the second component of the binary.

	OL Aperture	CL on-axis	CL local	θ_0 from $C_n^2(h)$	θ_0 from Grid
95Her	1.73	1.93	1.79	11.7	18.8
γDel	-2.39	-1.75	-2.30	15.2	21.5

Table 3.11: *Photometry Results for 95Her and γDel.*

In this context it is also interesting to compare the isoplanatic angles as calculated from the $C_n^2(h)$-profile present during the observations and that inferred from the reconstruction grid via equation

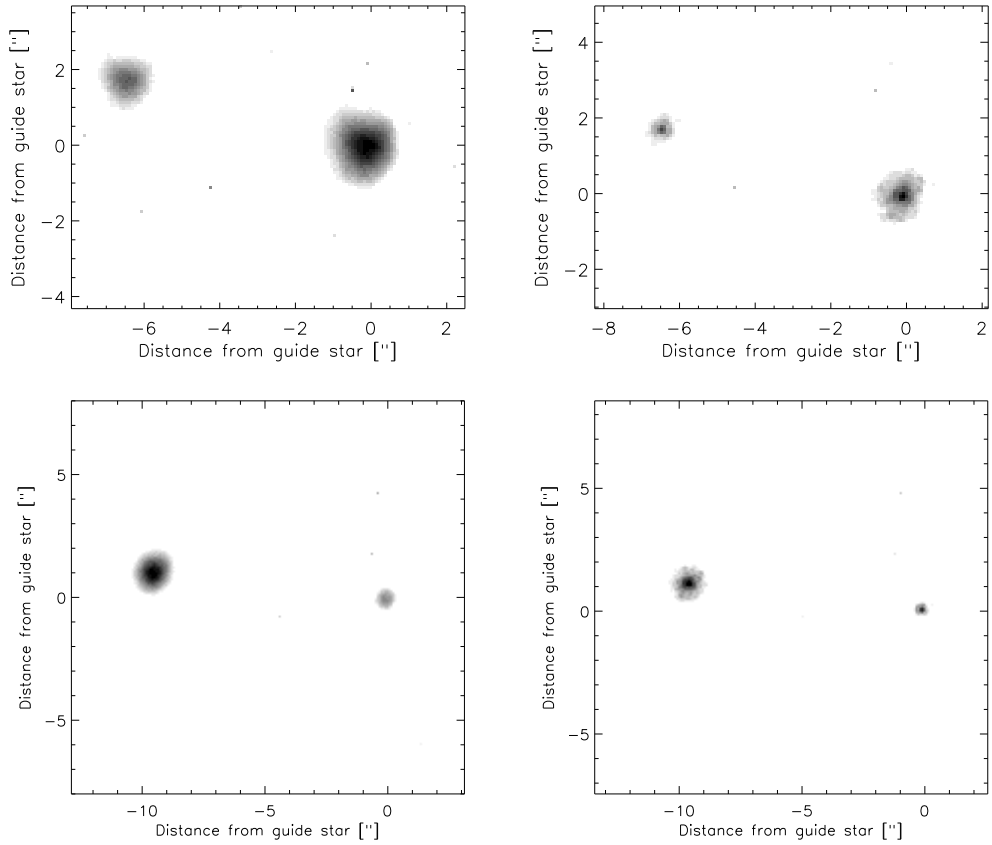

Figure 3.29: *Open- (left) and closed-loop (right) images of 95Her (top) and γDel (bottom).Intensity is displayed in inverted logarithmic scale for better visibility.*

Figure 3.30: *PSF grid used for photometry on M92 spanning from on-axis (left) to a distance of 40"; step size is 1", resolution 0.04"/pixel.*

3.19. The results of this comparison are also shown in table 3.11. Again, the practical value of the isoplanatic angle is much higher than the theoretical one, by a factor of 1.6 for 95Her and 1.4 for γDel.
The higher factor in the case of 95Her is easily explained by the performance differences of the correction: while the Strehl ratio of the guide star was 42% for 95Her, it reached 48% for γDel. The closer the performance of the loop lies to perfect on-axis correction, however, the more the effective isoplanatic angle approaches is theoretical minimum given from the atmospheric profile and equation 2.13. A practical consequence of this behavior is that, if an interesting object is located far from the corrective beacon, the on-axis correction performance can be deliberately degraded to enlarge the isoplanatic patch size. Some work to find an optimum between on-axis correction quality and isoplanatic patch size has been done by Chassat (1992).

Faint Guide Star: M92

The next example was done on a corrected image of the outer regions of M92; with its high airmass and low loop frequency, this example represents an extreme case in the sense that its operating at the very limits of ALFA's possibilities. The open- and closed-loop images used for the photometry are shown in figure 3.4.4. Note that the coma is clearly visible on several stars of the closed-loop image. As seen before, the on-axis Strehl ratio achieved was only about 13% in this case. This has

Distance from GS ["]	OL Aperture	CL on-axis	CL local
4.13	1.18	1.25	1.21
8.75	1.26	1.38	1.31
8.93	1.15	1.25	1.20
12.98	1.48	1.53	1.50
16.19	N/A	0.87	0.78
18.36	N/A	1.07	0.88
22.41	0.55	0.59	0.58
22.71	0.04	0.19	0.10
30.87	0.66	0.75	0.58

Table 3.12: *Photometry Results for M92*

a strong effect on the difference between the effective isoplanatic angle and its theoretical minimum; as noted when assessing the off-axis reconstruction accuracy of M92 before, the isoplanatic angle as calculated from the $C_n^2(h)$ profile scaled to the airmass of 1.6 was only 5.5"; using the Strehl ratios of the deconvolution grid shown in figure 3.4.4 and equation 3.19, however, gives an effective θ_0 of 26.6", nearly five times higher.
The results of the photometry, estimating the magnitude difference of several stars at various distances with respect to the guide star, are shown in table 3.12. Again, the estimates obtained by the local method are consistently smaller than those taken from the on-axis PSF. Additionally, with the

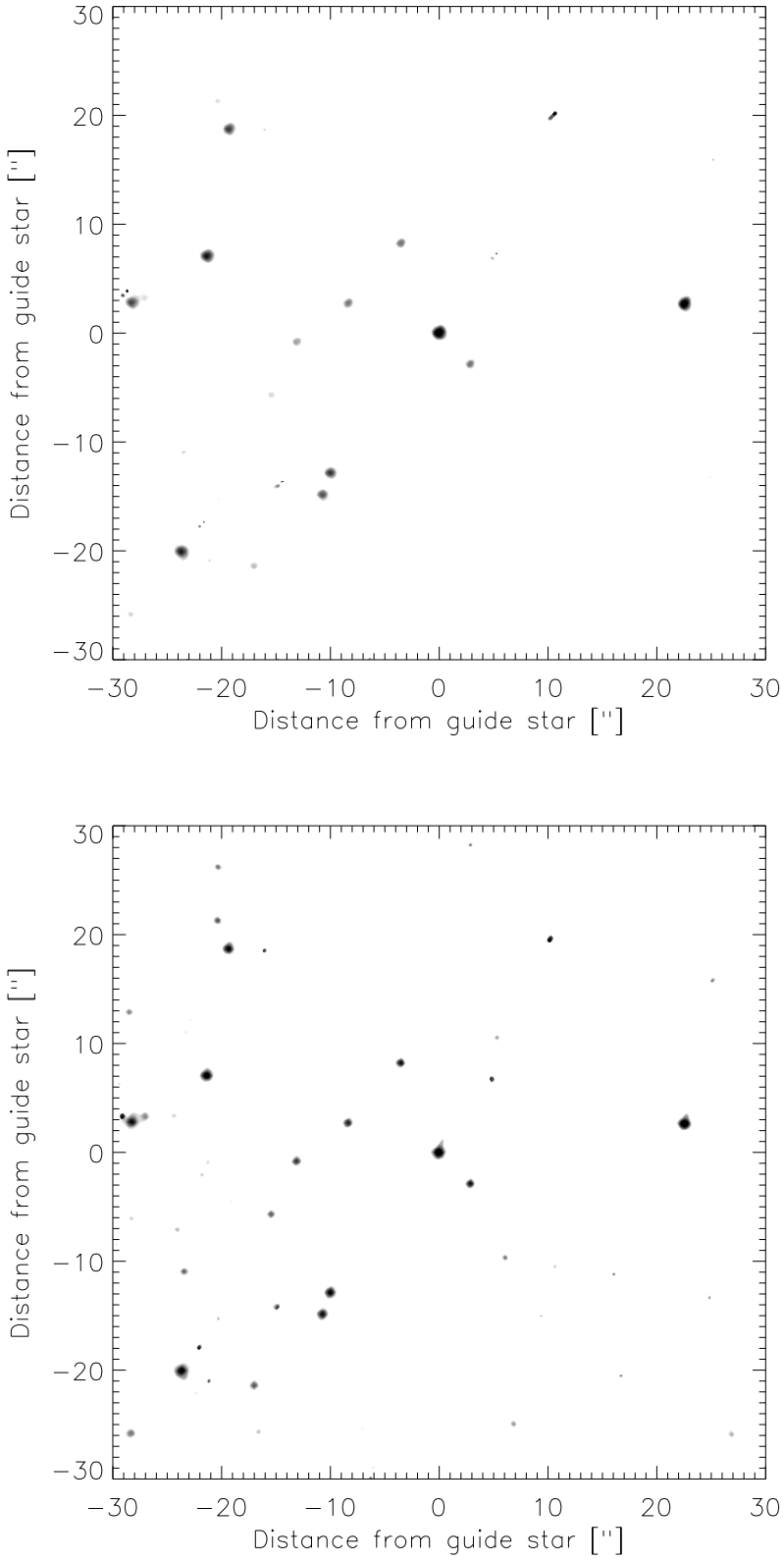

Figure 3.31: *Open- (left) and closed-loop (right) images of M92 centered on the guide star. Intensity is displayed in inverted logarithmic scale and the guide star masked out for better visibility.*

exception of the two most distant stars, the difference between the open-loop aperture photometry results and the local estimates are around a value of 3-5%, while that of the global method vary between 4 and 10%. The variation of the on-axis estimates, however, does not follow the expected behavior, which would imply a growing error with growing distance. Thus the results obtained for the faint guide star cannot be regarded as conclusive; nevertheless, the fact that the magnitude difference estimation by the local reconstruction is always smaller than for the global case indicates that less intensity is lost by applying off-axis PSFs.

Chapter 4

Conclusion

The goal of this work was the adaption and implementation of a PSF estimation algorithm for ALFA, allowing to reconstruct the optical properties of the system from wave-front sensor signals. This ability is highly desirable, since the scientific evaluation of data obtained with AO assistance is severely complicated by anisoplanacy and the varying nature of the PSF.

With the original algorithm developed for use with curvature systems, several modifications and adaptions had to be carried out; e.g. the aliasing behavior of Shack-Hartmann systems is quite different from that of curvature systems. Another task was the calculation of the correlation functions needed during the application of the algorithm both for the analytical shape of the Karhunen-Loeve functions and the measured shape of the deformable mirror.

The next step consisted of carrying out simulations that were used to test the routines developed for the PSF reconstruction task on ALFA as well as to assess the quality reachable by this estimation method. It was shown that photometric results on a simulated starfield can be dramatically improved using locally reconstructed PSFs.

One of the unsolved problems in the application of PSF estimation method to SHS systems was the low quality of gradient noise estimates obtainable during close-loop operations. Section 3.2 introduced a new method that operates directly on the gradient measurement time series and delivers superior results especially for the case of low-delay loop configurations. As reliable noise estimation is crucial for the applicability of the reconstruction algorithm, the importance of this result cannot be overestimated.

The reconstruction of off-axis PSFs in closed loop requires the knowledge of the current vertical configuration of the atmospheric turbulence. Hence, parallel measurements were carried out during an observation campaign in August/September 2000, using the ALFA system and the Imperial College's SCIDAR instrument. A complete software package had to be developed in order to reduce the tremendous amount of raw data provided by SCIDAR measurements. Apart from making available $C_n^2(h)$ profiles of the atmosphere, these observations also served the purpose to cross-check the reliability of the estimation of atmospheric parameters from both systems used; a very good agreement was found for these measurements. Additionally, an examination of the temporal variation of the essential quantities r_0 and θ_0 placed a limit on the time that atmospheric parameters can be regarded as constant.

The tasks described above led on to the actual comparison of measured closed-loop PSFs and OTFs with their reconstructed counterparts. This examination, however, was much complicated by the long-lasting malfunction of the Omega Cass camera, limiting the resolution of the images to an undersampled rate. In spite of this limitation, the quality of the reconstruction was still good on bright

and satisfactory on faint guide stars. The OTF estimation error generally was below 10% for the on-axis and below 25% for the off-axis case; additionally the most prominent deviations where of a static nature could be explained by the incomplete knowledge of the calibration PSF as well as a low SNR at the flanks of the measured PSF for the faint stars. Additionally, the faint star case revealed that a successful reconstruction of the PSF was not possible unless the new noise estimation method was used.
Finally, the reconstructed PSFs were used in a simple fitting scheme to asses possible improvements of photometric accuracy when using locally reconstructed PSFs; while the results were very encouraging for the bright guide star case, where the magnitude estimation error could be reduced to below 5%, the faint star case was not as conclusive, if pointing in the right direction.

Outlook: The PSF reconstruction software developed throughout this work is now capable to provide an estimation of a PSF anywhere on the field of view given only the gradient measurements, its associated interaction matrix and, if available, a $C_n^2(h)$ profile. It was designed to operate on data recorded with a resolution of 0.04" per pixel. Its routine use, however, is hampered by the need to stop ALFA's control system in order to download gradient measurements after a relatively short amount of time; additionally, the parallel recording of SCIDAR measurements is still far from being routine.
The impossibility of direct access to gradient measurements in the ALFA system should be addressed in any upgrade or redesign of the control system, as well as taken into account for future AO systems planned on Calar Alto (e.g. PYRAMIR). This modification would ensure the ability to reconstruct the on-axis PSF at all times during an AO observation run.
Obtaining constant coverage of atmospheric turbulence profiles, the requirement for off-axis PSF estimation, is much harder to address. In the opinion of the author, SCIDAR in its current state is not up to this task due to the impossibility of real-time or near real-time measurements and the overhead of calibration and staff required for its operation. There are, however, efforts underway to eliminate these disadvantages (McKenna et al., 2003). Alternatively, $C_n^2(h)$ measurements can also be obtained with other methods, that might be integrated with the seeing monitors already available at many sites.

Appendix A

The TURBULENZ simulation package

The TURBULENZ simulation package originated from a C program developed by Glindemann et al. (1993) and extended by Berkefeld (1998). It simulates the imaging properties of a layered turbulent atmosphere, and is configured by an input file containing the following information:

- The observation wavelength.
- An arbitrary number of turbulent layers with adjustable D/r_0, layer height, prevalent wind speed and direction, a decorrelation coefficient, and the desired outer scale.
- An arbitrary number of point sources (located at infinity).
- An arbitrary number of telescopes, characterized by their aperture diameter, position and image plane pixel scale.

During the preparation of this work, the whole C code was debugged, speed optimized and finally ported to IDL, in order to obtain a higher system independence.
The program generates phase screens according to a Kolmogorov type power law by spectral synthesis in Fourier space; since the size of a phase screen is limited, however, the spectrum is not perfectly modeled at the low frequency end, resulting in an effective outer scale on the order of the size of the phase mask. This effect is partly alleviated by the addition of so-called *subharmonics* (Lane et al., 1992), with the goal of achieving a high fidelity to the Kolmogorov law down to the frequency defined by the desired outer scale of each layer.
Deviation from the Taylor frozen flow hypothesis is also possible with TURBULENZ: the temporal evolution of the phase screen pattern is modeled by a Markov process with adjustable strength (Glindemann et al., 1993).
One of the most important capabilities of the package as compared to other simulation environments is the possibility to include the simulation of amplitude fluctuations and intensity scintillations caused by Fresnel diffraction on the phase grid of each layer (Berkefeld, 1998).
In the context of this work, it was necessary to carry out adaptive optics as well as SCIDAR simulations using TURBULENZ. While a simple approach, described in section 2.4, was used for AO, SCIDAR simulations demanded a stronger modification. If SCIDAR mode is switched on, the input file must contain the following additional information:

- The distance of the SCIDAR observation plane to the aperture plane of the telescope.
- The identification of two stars used for the SCIDAR measurements.

With this information, the phase propagation algorithm is modified such that it mimics the Rytov approximation while retaining the Fresnel diffraction code:

1. First, the observation plane distance is added to the height of each layer.
2. Then, for both stars involved, the resulting amplitude diffraction pattern is calculated for each layer
3. The total aperture plane scintillation pattern is found by first adding the log-amplitudes of the individual layer patterns and then calculating the resulting total intensity.
4. Finally, the two observation plane patterns corresponding to each star are added after shifting to the appropriate position given by the propagation distance from the aperture to the observation plane.

As was demonstrated in section 2.1, this simulation technique delivers excellent agreement of both "measured" $C_n^2(h)$-profiles and wind speeds/directions with the simulation parameters (see also Berkefeld et al. (2003)).

Appendix B

The SCAVENGER SCIDAR Package

SCIDAR measurements are delivering a tremendous amount of raw data in the form of individual observation plane exposures. Since no standard data reduction packages exist, a software package, SCAVENGER was developed in the context of this work.
The following tasks have to be performed in order to arrive at an accurate estimate of the $C_n^2(h)$-profile of the atmosphere:

- Calculation of the mean-normalized auto-covariance of a given number of observation plane exposures.
- Extraction of slices through the auto-covariance plane in direction of the line of separation of the stars as well as perpendicular to this line.
- Calculation of the T-matrix, i.e. the matrix connecting measurements in the autocorrelation plane with turbulence height and strength in the atmosphere.
- Inversion of the measurement equation.

The following paragraphs describe the tools developed to tackle those tasks.

Calculation of the auto-covariance function

The calculation of the mean-normalized auto-covariance function is straightforward but has a high computational load; it is the main reason why real-time or near real-time data reduction is as of today impossible with SCIDAR systems.
Since the actual value of the observation plane sampling is crucial in both determining the height resolution as well as potential errors in the SCIDAR measurement process, the routine doing the autocorrelation delivers an estimate of this value through the following algorithm:

- First, the average aperture image is calculated.
- Then the resulting image is binarized by assigning 0 to values below the image median value and 1 to values above it.
- Finally, an average is taken of the 10 pairs of most distant points in the illuminated part of the binarized image, delivering the pixel sampling and its standard deviation.

Note that these estimates are only accurate if the measurements are carried out in non-generalized SCIDAR mode, i.e. the observation plane coincides with the pupil of the telescope.

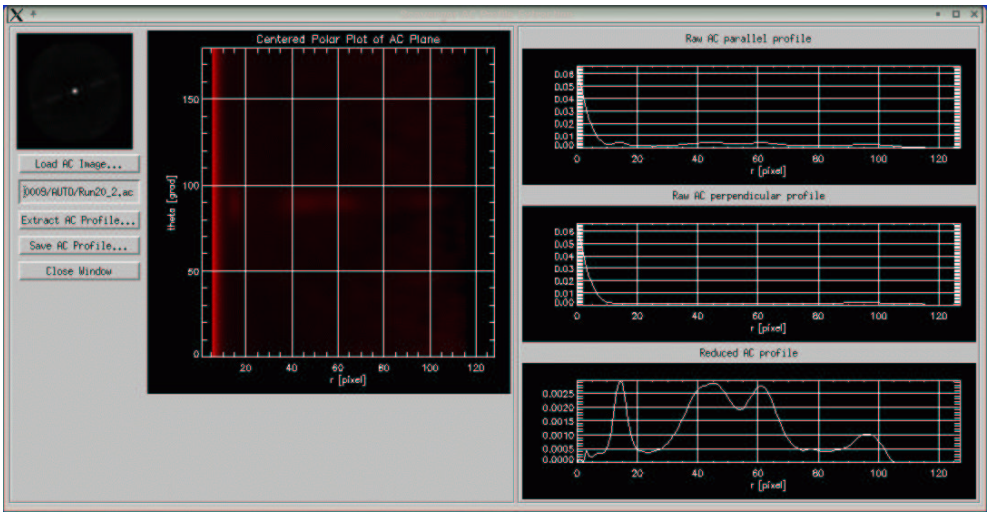

Figure B.1: *Screenshot of the interactive profile extraction routine.*

Extraction of the auto-covariance profile

With the auto-covariance function given, the next task is the extraction of the cuts through the auto-covariance plane; for this purpose, an interactive routine was created, as shown in figure B.1. On startup the user has to select a auto-covariance image, which is then displayed in Cartesian as well as polar coordinates.
In order to extract the cuts, the direction of separation of the two components has to be found; this is accomplished by asking the user first for the estimated radius of the central peak, which is then masked out exposing the fainter off-center components. Then, the user provides a radial position where the code scans for a secondary maximum. Taking a cut through the polar plot plane at the given position, the code reliably finds the location of the line of separation and finally extracts cuts parallel and perpendicular to this line, with the result of the extraction given by their difference. The cuts and the result are also plotted for control purposes, as can be seen in figure B.1.

Recovery of the $C_n^2(h)$-profile

After the auto-covariance profile $\vec{p}$ has been found, the measurement equation

$$\vec{p} = K\vec{x} + \vec{n}, \tag{B.1}$$

where $\vec{x}$ is the $C_n^2(h)$-profile and $\vec{n}$ a noise term, has to be inverted. This first requires the numerical calculation of the K matrix, given by equation 2.29. Apart from a brightness difference factor and the height shift due to generalized SCIDAR, the value of K depends on the zenith angle, the observation plane sampling and the separation of the binary's components. All of these values have to be provided by the user as can be seen in figure B.2. The code first checks if a suitable K-matrix has already been calculated; if not, a subroutine is started to accomplish this task, which is very time-consuming. A possible future update of the software package should thus involve the precomputation of a suitable grid of K-matrices, from which the needed ones could be interpolated.
Finally, both $\vec{p}$ and K are used to obtain a first estimate of the $C_n^2(h)$-profile by least squares inversion; this estimate is used as the initial guess for the conjugate gradients inversion of equation B.1. The

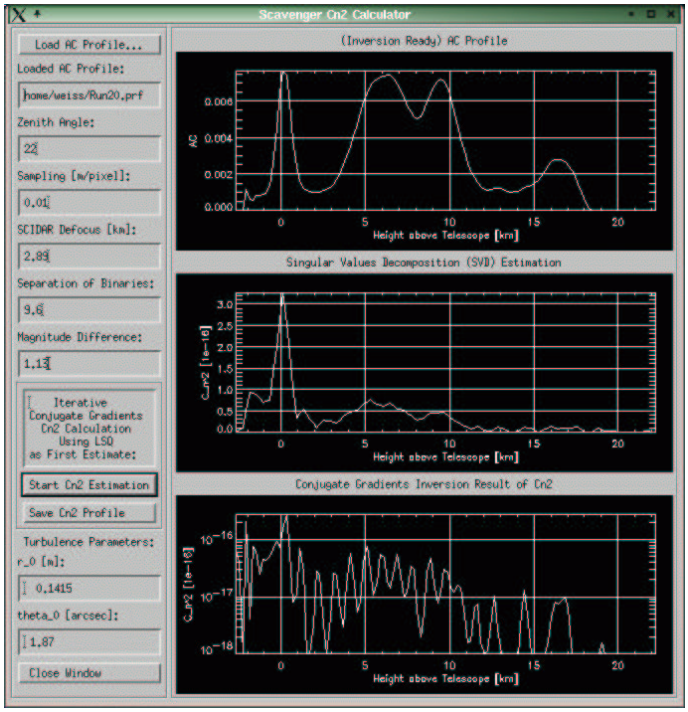

Figure B.2: *Screenshot of the interactive $C_n^2(h)$ recovery routine.*

original auto-covariance profile is shown along with the LSQ-estimate and the conjugate gradients result in the C_n^2-Calculator window (figure B.2), as well as estimates of r_0 and θ_0 at a wavelength of 500 nm calculated from the result.

During the development of SCAVENGER, care was taken to make the routines mostly independent of instrument and/or telescope specific constants like CCD size, aperture size etc. Thus, the package should be usable without major changes for any SCIDAR measurement; so far, SCAVENGER has been successfully used to reduce data taken from SCIDAR simulations with TURBULENZ, measurements at the Calar Alto 1.23m telescope with Imperial College's SCIDAR instrument (this work), and first measurements at the VATT on Mount Graham with the LBT SCIDAR instrument (McKenna et al., 2003).

Task Automation

The large amount of data produced by SCIDAR measurements makes interactive data reduction a very lengthy and tedious procedure. However, it is possible to automate data reduction using SCAVENGER's subroutines. Strictly speaking, user interaction is mostly necessary in the extraction of the auto-covariance profile $\vec{p}$, while the other parameters, like sampling, defocus etc., either stay constant during an observing run or change in a predictable way (e.g. the zenith angle). Thus, if these parameters are provided, the only task remaining is to find the line of separation between the components, which is accomplished by the following algorithm:

- Select an auto-covariance image from the current run.

- Map the image to polar coordinates.
- Mask the innermost and outermost radial regions of the polar auto-covariance image.
- Finally, identify the line of separation by searching for the angular cut for which variance is maximal.

The only additional information to be provided for full task automation is the extent of the regions to be masked; these parameters, however, are specific to the instrument and telescope used, thus sacrificing the system independent nature of the interactive routines.
All the SCIDAR results presented in section 3.3 were calculated using the non-interactive technique, which turned out to be effective for more than 90% of all auto-covariance images recorded.

Appendix C

ALFA PSF Reconstruction Software

This appendix lists the software packages developed during this work, which are necessary to carry out a successful PSF reconstruction on the ALFA system. It is divided into three sections, preparatory packages, which are usually executed only once and are only necessary to be re-run with system upgrades etc., auxiliary packages, which are used in the PSF reconstruction process, but can also be applied for other, stand-alone purposes, and finally the PSF reconstruction packages themselves. All of the routines worked are written in IDL in order to be easily portable between platforms

C.1 Preparatory Packages

C.1.1 Cross-talk matrix calculation

As noted in section 2.2, the cross-talk matrix is given by

$$\mathbf{C} = \mathbf{R}_{LS}\mathbf{D}_{\perp} \tag{C.1}$$

The interaction matrix of high-order modes is not measurable, since the DM cannot reproduce those modes. It is therefore necessary to simulate the response of the SHS to the involved high-order Karhunen-Loeve modes.
For this purpose, a complete model of the SHS measurement process was implemented, including the KS7 and KS28 arrays as well as the different available centroiding algorithms (Kasper, 2000). This simulation is used to construct the complete theoretical interaction matrix up to a given number of KL modes, from which, together with the measured interaction matrix for a given setup, the cross-talk matrix follows from $\mathbf{C} = \mathbf{R}_{LS}\mathbf{D}_{\perp}$.

C.1.2 Calculation of U_{ij}

The knowledge of the functions U_{ij} is mandatory for the reconstruction of both on- and off-axis PSFs. Although they are available in analytical form for Zernike polynomials, this is not the case for a general modal set. Additionally, it is always better to use actual measurements of the DM shape for the calculation of the functions instead of the theoretically expected values. For this purpose, a routine was implemented that carries out a numerical integration

$$U_{ij}(\rho) = \frac{\iint P(\vec{r})P(\vec{r}+\vec{\rho})\left[F_i(\vec{r}) - F_i(\vec{r}+\vec{\rho})\right]\left[F_j(\vec{r}) - F_j(\vec{r}+\vec{\rho})\right]d\vec{r}}{\iint P(\vec{r})P(\vec{r}+\vec{\rho})d\vec{r},} \tag{C.2}$$

given the shapes of the used modes.
The functions U_{ij} are calculated for all combinations of i an j for $i, j < 35$ and for $i = j$ only for $i, j \geq 35$, since high-order contributions are modeled from the theoretical Karhunen-Loeve covariance matrix, which is by definition diagonal. Low-order modes, however, often show non-zero off-diagonal elements due to deviations from perfect Kolmogorov turbulence, aliasing, noise etc.
One input parameter of the routine is a grid of the shape of modes used; thus, for modes where interferometric measurements of the actual DM shape are available, the analytically calculated modes can be replaced by measurements. In practice, this turned out to deliver better results during the PSF reconstruction process.

C.1.3 Calculation of σ_{ij}

The calculation of the σ_{ij} functions, needed for off-axis PSF estimation, follows the same lines as the calculation of the U_{ij}. Again, a numerical integration is carried out, this time according

$$\sigma_{ij}(\alpha, h) = \frac{0.023}{2^{5/3}} \iint d^2\vec{f} Q_i(\vec{f}) Q_j(-\vec{f}) |\vec{f}|^{-11/3} \exp\left[-\frac{4i\pi h}{D}\vec{f}\vec{\alpha}\right]. \tag{C.3}$$

A potential problem is posed by the divergence of the integrand with $f \to 0$; as shown by Chassat (1992), the limiting value is generally non-zero for Zernike polynomials. Thus, in principle sophisticated numerical integration techniques would have to be employed in order to yield sensible results; luckily, as can be seen from equation 2.78, $C_{ij} \sim \sigma_{ij}$ only enters the PSF estimation process in the form of differences for equal i and j. As equation C.3 effectively is just a Fourier transform, an unknown value for $f = 0$ corresponds to a constant bias in real space, which cancels in the differences. Thus, the value of the integrand at $f = 0$ can safely be set to zero before transforming.
After calculation, the σ_{ij} are transformed to polar coordinates which are more convenient for the use in equation 2.78.

C.2 Auxiliary Packages

C.2.1 Noise estimation

Noise estimation is implemented following the methods developed in section 3.2. There are two different routines, using the weighted difference and the direct difference methods respectively. The master routine is provided the measured closed-loop gradients and the loop frequency; for frequencies below 200 Hz, a loop delay of 1 is assumed, for frequencies up to 500 Hz a loop delay of 2; up to this frequency the weighted difference method is used for noise estimation, for higher frequencies, the estimation switches to the direct difference method.

C.2.2 Loop simulation

The simulation of the loop feedback in closed-loop operation is fundamental in the retrieval of the applied mirror modes during a measurement. For this purpose a complete implementation of the control algorithm in IDL was done. Apart from a freely adjustable gain, there are three additional parameter sets, α, A, and B, which are used to select specific controller modes depending on the loop frequency and control algorithm (Wirth et al., 1998). Table C.1 lists the values of the parameters used, where *PI* denotes the standard PI controller and *OPT* stands for the optimal controller (Looze et al., 1999).

Type	PI	PI	PI	OPT
Range [Hz]	0-300	301-600	>600	0-300
α	0.0	0.0	0.2	0.893
A	(0,0,-0.3)	(0,0,0)	(0,0,0.5)	(-0.077, -0.512, -0.350)
B	(0,0,0)	(0,0,0)	(0,0,0)	(0,0,0.390)

Table C.1: *ALFA control loop parameter sets; for the OPT controller, the loop gain has to be multiplied by 59.48.*

By default, the loop simulation selects the PI controller suitable for the given frequency. If the optimal controller was used during a measurement, the parameters have to be adjusted by hand.
The other crucial input parameters of the loop simulation are the calibration matrix (the gradient matrix) and the measured gradients. Its output is the time series of modal coefficients as applied to the DM; in order to obtain the actual variance of the mirror modes it is necessary to double the values obtained from the simulation (due to reflection, the output is always half the atmospheric mode present). Additionally, the first 50-100 simulated mirror modes should not be used for variance calculations, since they represent the initial phase of correction starting from a flat mirror and thus are prone to unnatural oscillations.
As has been done in section 3.2, the loop simulation can also be used to simulate closed-loop operation starting from an open-loop gradient measurement set according to the following algorithm:

1. Set up the closed-loop simulation with the desired parameters; from the first entry of the open-loop gradient set, calculate the initial modal input using the reconstruction matrix $\mathbf{R}$ constructed from the corresponding interaction matrix $\mathbf{D}$.

2. Calculate the modal output of the loop, and construct the corresponding gradients by direct application of $\mathbf{D}$ on the doubled value of the current mirror modal coefficients.

3. Subtract the mirror induced gradients corresponding to the desired loop delay from the next set of open-loop gradients; use the result to calculate the next modal input to the loop.

4. Start over at step 2.

The output of this algorithm are time series of simulated closed-loop gradients and mirror modes, which can be used to examine the actual transfer function of the loop for a given set of parameters as well as for noise propagation studies.

C.2.3 Closed-loop r_0 estimation

Closed-loop estimation of the Fried parameter is essential for both correction of aliasing noise and the scaling of the high-order mode contribution to the PSF. The routine integrates most of the results of described above and thus has to be invoked providing the gradient matrix, the closed-loop gradients, loop gain and frequency, as well as the cross-talk matrix. It then calls the noise estimation routine and the loop simulation in order to get the mirror modes and the gradient noise estimates. Following the iterative algorithm described in section 2.3 and using equation 2.58 it produces an estimate of r_0.

C.3 PSF Reconstruction Packages

The most important packages are, of course, those used for the actual PSF reconstruction. A prerequisite for both on- and off-axis estimation is the knowledge of the calibration PSF; thus a routine has been implemented that takes a K+Brγ filtered image of the fiber source and constructs an OTF estimate with adequate sampling. Due to lack of suitable images, however, this routine has not been thoroughly tested.

C.3.1 On-axis OTF/PSF calculation

The on-axis OTF/PSF reconstruction routine needs the following input:

- the on-axis OTF $T(\vec{\rho})$,
- the observation wavelength λ
- the interaction (gradient) matrix $\mathbf{D}$,
- the time-series of closed loop gradients $\vec{g}(t)$,
- the theoretical interaction matrix $\mathbf{D}_{\perp}$ as calculated by the routine of section C.1.1,
- the loop frequency and gain,
- the theoretical covariance matrix for Karhunen-Loeve modes,
- and the U_{ij} functions for the modal set used. obtained from C.1.2.

With this information, the reconstruction algorithm calls the auxiliary routines for noise and r_0 estimation, which in turn are used to construct $<\vec{\epsilon}\vec{\epsilon}^T>$ and $<\vec{a}_{\perp}\vec{a}_{\perp}^T>$. Together with the U_{ij} functions the on-axis OTF is calculated and saved to disk, before a final Fourier transform delivering the PSF for the given wavelength at a resolution of 0.04”/pixel.

C.3.2 Off-axis OTF/PSF calculation

Apart from the on-axis OTF, the off-axis PSF reconstruction requires additional information:

- the angular displacement $\vec{\alpha}$ of the reconstruction position from the guide star given in polar coordinates,
- the $C_n^2(h)$-profile of the atmosphere together with the values of h corresponding to each point in the profile,
- and the σ_{ij} functions as calculated in section C.1.3.

With this information, the anisoplanatic transfer function (ATF) is calculated and multiplied with the on-axis OTF to obtain the total OTF; again, the resulting OTF is saved to disk before the off-axis PSF is found by a Fourier transformation.

All of the routines described above are more or less adapted to the ALFA system; care has been taken, however, to put specific parameters like mirror diameter, obstruction ratio, etc. into constants, such that the routines can easily be modified for other telescopes and/or system, with the obvious exception of the closed-loop simulation.

Bibliography

Abramovici, A. and Chapsky, J.: 2000, *Feedback Control Systems: A Fast-Track Guide for Scientists and Engineers*, Kluwer Academic Publishers

Ageorges, N. and Dainty, C. (eds.): 2000, *Adaptive Optics with Laser Guide Stars*, Kluwer Academic Publishers

Avila, R.: 1998, *Ph.D. thesis*, Universite de Nice

Babcock, H.: 1953, *PASP* **65**, 229

Barchers, J. D. and Ellerbroek, B. L.: 1999, in *Proc. SPIE*, Vol. 3762, pp 125–139

Bergmann, P.: 1946, *Phys. Rev.* **70**, 486

Berkefeld, T.: 1998, *Ph.D. thesis*, Ruprecht-Karls-Universität Heidleberg

Berkefeld, T., Weiß, A. R., and Glindemann, A.: 2003, *submitted to Appl. Opt.*

Beuzit, J., Hubin, N., Gendron, E., Demailly, P., Gigan, F., Lancombe, F., Chazallet, F., Rabaud, D., and Rousset, G.: 1994, in *Proc. SPIE*, Vol. 2201, pp 955–961

Brandner, W., Rousset, G., Lenzen, R., Hubin, N., Lacombe, F., Hofmann, R., Moorwood, A., Lagrange, A.-M., Gendron, E., Hartung, M., Puget, P., Ageorges, N., Biereichel, P., Bouy, H., Charton, J., Dumont, G., Fusco, T., Jung, Y., Lehnert, M., Lizon, J.-L., Monnet, G., Mouillet, D., Moutou, C., Rabaud, D., Röhrle, C., Skole, S., Spyromilio, J., Storz, C., Tacconi-Garman, L., and Zins, G.: 2002, *ESO Messenger* **107**, 1

Cannon, R.: 1996, *JOSA A* **13**, 862

Chassat, F.: 1989, *J. Optics (Paris)* **20**, 13

Chassat, F.: 1992, *Ph.D. thesis*, Universite Paris XI Orsay

Chun, M. and Avila, R.: 2002, in *Astronomical Site Evaluation in the Visible and Radio Range*, Vol. 266 of *ASP Conf. Proc.*, p. 72

Conan, J.-M., Rousset, G., and Madec, P.-Y.: 1995, *JOSA A* **12**, 1559

Dai, G.-M.: 1995, *JOSA A* **12**, 2182

Dai, G.-M.: 1996, *JOSA A* **13**, 1218

Diolaiti, E., Ragazzoni, R., and Tordi, M.: 2001, *A& A* **372**, 710

Dorf, R. and Bishop, R.: 2001, *Modern Control Systems*, Prentice-Hall, 9 edition

Fante, R. L.: 1975, *Proc. IEEE* **63**, 1669

Fried, D. L.: 1965, *JOSA* **55**, 1427

Fuchs, A., Tallon, M., and Vernin, J.: 1998, *PASP* **110**, 86

Fusco, T., Conan, J.-M., Mugnier, L., Michau, V., and Rousset, G.: 2000, *A& A Suppl. Ser.* **142**, 149

Gendron, E. and Lena, P.: 1994, *A& A* **291**, 337

Gendron, E. and Lena, P.: 1995, *A& AS* **111**, 153

Gershenfeld, N.: 1999, *The Nature of Mathematical Modeling*, Chapt. 10, Cambridge University Press

Glindemann, A., Hamilton, D., Hippler, S., Rohloff, R.-R., and Wagner, K.: 1997, in N. Hubin (ed.), *ESO Workshop on Laser Technol-*

ogy for Laser Guide Star Adaptive Optics, pp 120–125

Glindemann, A., Lane, R. G., and Dainty, J. C.: 1993, *J. Mod. Opt.* **40**, 2381

Gracheva, M., Gurvich, A., and Kallistrova, M.: 1970, *Radiophys. Quantum Electron.* **13**, 40

Greenwood, D. P.: 1976, *JOSA* **66**, 193

Greenwood, D. P.: 1977, *JOSA* **67**, 174

Hamilton, J.: 1994, *Time Series Analysis*, Princeton University Press

Harder, S. and Chelli, A.: 2000, *A& A Suppl. Ser.* **142**, 199

Hardy, J. W.: 1998, *Adaptive Optics for Astronomical Telescopes*, Oxford University Press, New York

Hartmann, J.: 1900, *Zeitschr. f. Instr.* **24**, 1

Hippler, S., Glindemann, A., Kasper, M., Kalas, P., Rohloff, R., Wagner, K., Looze, D., and Hackenberg, W.: 1998, in *Proc SPIE*, Vol. 3353, pp 44–55

Högbom, J.: 1974, *ApJS* **15**, 417

Homstad, G., Strohbehn, J., Berger, R., and Heneghan, J.: 1974, *JOSA* **64**, 162

Kasper, M. and Hippler, S.: 2003, in *Proc. SPIE*, Vol. 4839, in press

Kasper, M., Looze, D., Hippler, S., Herbst, T., Glindemann, A., Ott, T., and Wirth, A.: 2000a, *Exp. Astron.* **10**, 49

Kasper, M. E.: 2000, *Ph.D. thesis*, Ruprecht-Karls-Universität Heidelberg

Kasper, M. E., Looze, D. P., Hippler, S., Feldt, M., Weiß, A. R., Glindemann, A., and Davies, R.: 2000b, in *Proc. SPIE*, Vol. 4007, pp 592–599

Klückers, V. A., Wooder, N. J., Nicholls, T. W., Adcock, M. J., Munro, I., and Dainty, J. C.: 1998, *A& A Suppl. Ser.* **130**, 141

Labeyrie, A.: 1970, *A& A* **6**, 85

Lane, R. G., Glindemann, A., and Dainty, J. C.: 1992, *Waves in Random Media* **2**, 209

Law, N. and Lane, R.: 1996, *Opt. comm.* **126**, 19

Lee, R. and Harp, J.: 1969, *Proc. IEEE* **57**, 375

Lenzen, R., Bizenberger, P., Salm, N., and Storz, C.: 1998, in *Proc. SPIE*, Vol. 3354, pp 493–499

Looze, D., Beker, O., Kasper, M., and Hippler, S.: 1999, in *Conference on Control Applications*, IEEE

Mahajan, V.: 1994, *Applied Optics Suppl.* **5**, 8125

McKenna, D. L., Avila, R., Hill, J. M., Hippler, S., Salinari, P., Stanton, P., and Weiß, A. R.: 2003, in *Proc. SPIE*, Vol. 4839, pp 825–836

Melsa, J. and Cohn, D.: 1978, *Decision and Estimation Theory*, McGraw-Hill

Nappo, C. J.: 2002, *An Introduction to Atmospheric Gravity Waves*, Academic Press

Noll, R. J.: 1976, *JOSA* **66**, 207

Obukhov, A. M.: 1949, *Izv. Akad. Nauk. S.S.S.R., Ser. Geograf. Geofiz.* **13**, 58

Pope, S. B.: 2000, *Turbulent Flows*, Cambridge University Press

Press, W. H., Flannery, B. P., Teukolsky, S. A., and Vetterling, W. T.: 1993, *Numerical Recipes in C*, Cambridge University Press, 2nd ed. edition

Prieur, J.-L., Daigne, G., and Avila, R.: 2001, *A& A* **371**, 366

Primot, J., Rousset, G., and Conan, F.: 1990, *JOSA A* **7**, 1598

Rabien, S., Ott, T., Hackenberg, W., Eckart, A., Davies, R., Kasper, M., and Quirrenbach, A.: 2000, *Exp. Astron.* **10**, 75

Ragazzoni, R., Diolaiti, E., Farinato, J., Fedrigo, E., Marchetti, E., Tordi, M., and Kirkman, D.: 2002, *A& A* **396**, 731

Ragazzoni, R. and Farinato, J.: 1999, *A& A* **350**, L23

Roddier, F.: 1981, in *Progress in Optics*, Vol. 19, pp 281–376, North-Holland Publ. Co., Amsterdam

Roddier, F.: 1988, *Applied Optics* **27**, 1223

Roddier, F.: 1999, *Adaptive Optics in Astronomy*, Cambridge University Press

Roddier, F. and Roddier, C.: 1986, in *Proc. SPIE*, Vol. 628, pp 298–304

Roggemann, M. C. and Welsh, B.: 1996, *Imaging through Turbulence*, CRC Press

Rousset, G., Fontanella, J., Kern, P., Lena, P., Gigan, P., and Rigaut, F.: 1990, *A& A* **230**, L29

Rousset, G., Fontanella, J., Kern, P., Lena, P., and Rigaut, F.: 1993, in *NATO ASI Series*, Vol. 423, pp 336–344, Kluwer

Saint-Jacques, D. and Baldwin, J. E.: 2000, in *Proc. SPIE*, Vol. 4006, pp 951–962

Shack, R. and Platt, B.: 1971, *JOSA* **61**, 656

Strehl, K.: 1902, *Zeitschr. Instrum.* **22**, 214

Tallon, M. and Foy, R.: 1990, *A& A* **235**, 549

Tatarski, V.: 1971, *The Effect of the Turbulent Atmosphere on Wave Propagation*, US Dept. of Commerce, Springfield, VA

Tyler, G.: 1992, in *Adaptive Optics for Large Telescopes*, Vol. 19, p. 8, OSA Technical Digest Series

Veran, J.-P., Rigaut, F., Maitre, H., and Rouan, D.: 1997, *JOSA A* **14**, 3057

Vernin, J., Barletti, R., Ceppatelli, G., Paterno, L., Righini, A., and Speroni, N.: 1979, *Appl. Opt.* **18**, 243

von der Lühe, O., Berkefeld, T., and Soltau, D.: 2002, in *Proc. SPIE*, Vol. 4538, pp 197–204

Wang, J. and Markey, J.: 1978, *JOSA* **68**, 78

Weiß, A. R., Hippler, S., Kasper, M. E., and Feldt, M.: 2002a, in *Proc. SPIE*, Vol. 4538, pp 135–143

Weiß, A. R., Hippler, S., Kasper, M. E., Wooder, N. J., and Quartel, J.: 2002b, in *Astronomical Site Evaluation in the Visible and Radio Range*, Vol. 266 of *ASP Conf. Proc.*, p. 86

Winker, D.: 1991, *JOSA A* **8**, 1568

Wirth, A., Navetta, J., Looze, D., Hippler, S., Glindemann, A., and Hamilton, D.: 1998, *Applied Optics* **37**, 4586

Danksagung

An dieser Stelle möchte ich mich bei all jenen bedanken, die zum Gelingen dieser Arbeit beigetragen haben. Danke an ...

Stefan Hippler, Markus Feldt, Markus Kasper und Thomas Berkefeld für die fachliche Betreuung, Einführung in das weite Feld der adaptiven Optik sowie unzählige andere Dinge, die für die Durchführung dieser Arbeit unverzichtbar waren.

Prof. Reinhard Mundt und Prof. Immo Appenzeller für die Erstellung der Gutachten.

Nick Wooder, John Quartel, Rachel Johnston, and Ian Munroe for their SCIDAR instrument and the support during and after the observations.

Roberto Ragazzoni for his patience during the last phase of my Ph.D. work which largely distracted me from other projects.

meine aktuellen und ehemaligen Büromitbesetzer Joana Costa, Elena Puga, Christian Wolf, Markus Kasper und Sadegh Khochfar für das gute Arbeitsklima, und viele Gespräche abseits der grauen Theorie.

meine Kollegen Wolfgang Gässler, Markus Hartung, Sebastian Egner, Stefan Hippler und Markus Feldt für die praktische und moralische Unterstützung zum Ende der Arbeit .

meine Schwestern Claudia und Monika, deren Männern Harm-Dirk und Thomas und meinen Freunden Martin Dürr, Jörg Assmann und Drazen Zagac für Ablenkung und Hilfe in schwierigen Situationen.

meine Frau Yvonne, meinen Sohn Levi und meine Tochter Rebekka für ihre Geduld; ohne das Organisationstalent meiner Frau und ihrer Herrschaft über das alltägliche Chaos wäre diese Arbeit nicht zustande gekommen.

meine Eltern, die mir mein Studium überhaupt erst ermöglichten und mich dabei stets nach Kräften unterstützten.